

ONLINE DAMAGE DETECTION ON SHAFTS USING TORSIONAL AND UNDERSAMPLING MEASUREMENT TECHNIQUES

By

Vishaal Bhana

Submitted in partial fulfilment of the requirements for the degree

Master of Engineering

In the Faculty of

Engineering, Built Environment and Information Technology

University of Pretoria, Pretoria

February 2013



ONLINE DAMAGE DETECTION ON SHAFTS USING TORSIONAL AND UNDERSAMPLING MEASUREMENT TECHNIQUES

Vishaal Bhana

Supervisor: Professor P.S Heyns

Department: Mechanical and Aeronautical Engineering

Degree: Master of Engineering

Abstract

The presence of cracks in rotors is one of the most dangerous defects of rotating machinery. This can lead to catastrophic failure of the shaft and long out-of-service periods. The occurrence of a crack in a rotating shaft introduces changes in flexibilities which alters the dynamics during operation. This research deals with detecting damage in rotors by means of constantly monitoring the variation in the rotor's dynamics during normal operating conditions. This project entails a computer finite element section as well as an experimental investigation.

The flexibility in the region of the crack is different from an uncracked section. A finite element model of a shaft is built and investigated. The damaged model is the same except that the nodes in the location of the crack are not equivalenced in order to represent the crack. A simple constant cross-sectional shaft with semi-circular transverse surface cracks varying in size have been modelled on the Patran finite element software and a normal modes analysis was done using the Nastran solver. The results revealed a change in the natural frequencies due to the variation in the size of the crack.

The experimental investigation involved creating sample shafts with damage positioned in them that would closely resemble what one may find in actual real-life situations and the dynamics during rotation with various torsional loadings are investigated and monitored using three methods. A fibre-optical sensor, Digital image correlation system and telemetry strain gauges were used. Undersampling techniques were used for the DIC system. Results showed that the fibre-optic sensor is by far the most favourable as it is able to detect damage under constant operation. The finite element model was updated by re-modelling the geometry, damage and material properties. The solution of the analysis matched the experimental results closely and model verification was achieved.

Acknowledgments

I would like to thank the following people who have been influential in this project and showed guidance and support throughout my academic career:

Prof. P.S. Heyns, for his guidance, understanding, knowledge and great attitude in encouraging me and pointing me in the right direction during the project.

Sasol Laboratory at the University of Pretoria, for allowing me access to equipment required during the experimental stage of the project.

Special thanks to George Breytenbach and Herman Booysen for always willing to lend a helping hand and giving guidance during the experimental testing.

Gerrit Visser and Hennie Klopper at Esteq for their assistance with the finite element modelling.

Rudi Nel at CSM Engineering for manufacturing and giving advice into practical design approaches during the manufacturing stage.

My parents and sisters for their immense support throughout my studies and positive attitude during the tough stressful times.

My colleagues at the University for their assistance with work and their companionship through the study years.

Contents

1. Chapter 1- Introduction and background	1
1.1. Introduction	1
1.2. Literature Study	3
1.2.1. Failure cases	3
1.2.2. Online monitoring	5
1.2.3. Research developments	6
1.3. Project overview and objectives	11
1.3.1. Chapter overview	11
1.3.2. Objectives	11
2. Chapter 2- Mathematical modelling and processing techniques	13
2.1. Overview	13
2.2. Basic Vibration and Finite Element Theory	13
2.3. Fibre optic Sensor	13
2.1. Telemetry	16
2.2. Digital Image Correlation system	18
2.3. Processing techniques	23
3. Chapter 3 Finite Element Analysis	24
3.1. Overview	24
3.2. Key FEM parameters	24
3.2.1. Geometry	24
3.2.2. Mesh	24
3.2.3. Boundary conditions	25
3.2.4. Loads	25
3.2.5. Material properties	25
3.3. Rotor model design and analysis	26
3.3.1. Model setup	26
3.3.2. Mesh type selection	27
3.3.3. Meshing and convergence study	29
3.3.4. Boundary condition modelling	31
3.3.5. Material selection	32
3.3.6. Analysis and results	32
3.3.7. Damage modelling	34
3.4. Equipment location analysis	37

3.5.	Conclusion.....	39
4.	Chapter 4- Experimental setup and Test procedure.....	40
4.1.	Overview	40
4.2.	Manufacturing	40
4.3.	Setup.....	42
4.4.	Fibre-optical sensor setup.....	43
4.5.	Telemetry setup.....	45
4.5.1.	Shunt calibration.....	48
4.5.2.	Torque-Load calibration.....	49
4.6.	Digital Image Correlation (DIC) system setup.....	50
4.7.	Tachometer setup.....	54
4.8.	Test procedure.....	56
5.	Chapter 5- Post-processing and Observations.....	58
5.1.	Overview	58
5.2.	Post-Processing and Observations.....	58
5.2.1.	Fibre-optic sensor	59
5.2.2.	Telemetry strain gauge system	64
5.2.3.	DIC.....	68
5.3.	Remarks	73
6.	Chapter 6- Model updating and final results.....	74
6.1.	Overview	74
6.2.	Model updating.....	74
6.2.1.	Parameter modification	74
6.3.	Undamaged comparison of experimental and FEM	76
6.4.	Strain response investigation.....	76
6.5.	Conclusion of updated FEM	80
6.6.	Final Results	81
6.6.1.	Fibre-optic sensor	81
6.6.2.	Telemetry system.....	83
6.6.3.	DIC.....	84
6.6.4.	Further undersampling investigation.....	85
6.7.	Conclusion of results.....	87
7.	Chapter 7- Conclusions and Recommendations.....	89
7.1.	Conclusion.....	89

7.2.	Recommendations and Future work	90
8.	Chapter 8- References	92
9.	Appendix A: Solidworks drawing of setup for manufacturing	7.2-96
10.	Appendix B: Detailed lumped spring-mass calculations and FEM matrices derivation.....	7.2-97
10.1.	Lumped spring-mass system	10.1-97
11.	Appendix C: Torque calculation for frequency response analysis	10.1-99
12.	Appendix D: Equipment Specification sheets	10.1-101
12.1.	Digital Image Correlation System.....	12.1-101
12.1.1.	Camera lens and measuring volumes	12.1-102
12.2.	Shunt resistor calibration.....	12.2-102
12.3.	Digital Image Correlation system	12.3-102
12.3.1.	Marker size.....	12.3-102
12.3.2.	Camera setup	12.3-103
13.	Appendix E: Matlab codes	12.3-104
13.1.	Order removal and plotting of data	13.1-104
13.2.	Creating tacho signal using Tacho function	13.2-109

List of Figures

Figure 1 Potential failure cycle in machinery.....	1
Figure 2 Online monitoring machine cycle	2
Figure 3 Speckled pattern on test object (Chu et al., 1985)	9
Figure 4 Deformed pattern as a result of strain through use of pixel correlation (Mguil-Touchal et al., 1997)	9
Figure 5 Reference and vibration signal of square wave (Resor et al., 2005)	14
Figure 6 Constant time and angle sampling (Groover et al., 2005)	15
Figure 7 Time signal of an accelerating shaft (Groover et al., 2005)	16
Figure 8 a) Frequency content of time signal showing RPM frequency and a 20Hz frequency, b) Order free frequency content showing only the 20Hz frequency (Groover et al., 2005).....	16
Figure 9 Torsional strain gauge on a shaft (How strain gauges work).....	17
Figure 10 a) Mounting of gauge on shaft, b) Wheatstone representation of gauge resistors (National Instruments, 1998).....	17
Figure 11 Illustration of aliasing (Heyns, 2008).....	19
Figure 12 Time signal sampled at two rates	20
Figure 13 Detailed view of undersampling	20
Figure 14 Original spectrum showing undersampled folds (Hosking, n.d).....	21
Figure 15 Folded fan to undersampled frequency F_s and showing aliasing (Hosking, n.d).....	21
Figure 16 Band-limited frequency spectrum (Hosking, n.d).....	21
Figure 17 Fan-fold of band-limited frequency spectrum showing desired frequencies (Hosking, n.d).....	21
Figure 18 Fan-paper frequencies applied to example	22
Figure 19 Frequency plot of over and undersampled signals.....	23
Figure 20 Schematic diagram of test model	26
Figure 21 a) 4 noded Quad4 element, b) 8 noded Quad8 element (Patran Library).....	28
Figure 22 Bending defects present in quad4 element a) Deformation mode in pure bending b) Quad4 element under pure bending (Cook R.D et al, 2002)	28
Figure 23 Hex20 or "brick" element (Patran Library)	29
Figure 24 Surface mesh created using mesh seeds and then extruding the elements	30
Figure 25 Frequency convergence	30
Figure 26 Percentage error convergence	31
Figure 27 Bearing boundary condition 1 and 2 representing x and y coordinates encircled	32
Figure 28 Final FEM model for analysis	33
Figure 29 1st Torsional mode shape	33
Figure 30 2nd Torsional mode shape.....	33
Figure 31 Schematic diagram of lumped spring mass system	34
Figure 32 Cross section of the transverse crack inserted into the shaft of depth a	34
Figure 33 a) Selected nodes that are not equivalenced in order to represent a crack, b) Pink circles shows the nodes that were equivalenced	35
Figure 34 Change in torsional frequency with crack depth a) 1st mode b) 2nd mode	36
Figure 35 Comparison of Frequency ratio between FEM data and Lebold et al. (2003) experimental study.....	36
Figure 36 1st torsional mode shape for magnitude response analysis	37
Figure 37 Comparison of strain response at motor and free-end	38

Figure 38 Rotor setup in bearings coupled to the motor on the right	40
Figure 39 Manufactured rotor used for testing	41
Figure 40 Rigid flange coupling used	41
Figure 41 a) 3kW DC motor with controller box, b) Controller box controls.....	42
Figure 42 Brake setup on rotor	43
Figure 43 Bearing and spacer setup.....	43
Figure 44 Pump for hydraulic brake.....	43
Figure 45 Complete brake setup with control switch on left and control valve in middle	43
Figure 46 Optic sensor with coded "zebra" tape	45
Figure 47 (a) Square wave with too much gain, (b) gain adjusted using screw driver	45
Figure 48 Gain set to produce a better square wave	45
Figure 49 Components of telemetry system (Binsfeld Engineering Inc.)	46
Figure 50 Torsional strain gauge.....	47
Figure 51 Telemetry system mounted on the shaft	47
Figure 52 Loss of strain signal resulting in over-ranging.....	48
Figure 53 Shunt resistor applied to bridge (Technology, 2000).....	49
Figure 54 Torque load applied to FEM model for strain result.....	50
Figure 55 Resulting strain from torque load calibration.....	50
Figure 56 Camera setup and dimension descriptions (GOM, 2010).....	51
Figure 57 Calibration setup, calibration cross and strobe light positions	52
Figure 58 Camera adjusted such that laser appear on cross-hairs, Left camera not set, right camera correctly set	53
Figure 59 Focus set such that blurry images like left camera adjusted to focus as in right camera	53
Figure 60 Object markers showing a span of 10 pixels.....	54
Figure 61 Overall rotor and test equipment setup	54
Figure 62 Tachometer setup with reflective tape.....	54
Figure 63 a) Periodic tacho signal for constant speed run, b) Tacho signal showing 46 optic sensor pulses per revolution	55
Figure 64 Inconsistent tacho signal due to strobe lights	55
Figure 65 Spectrogram of runup test.....	60
Figure 66 Averaged 2D plot of runup test	60
Figure 67 Spectrogram plot of Constant speed test run.....	61
Figure 68 Averaged 2D plot of the constant speed test run.....	62
Figure 69 Constant time and angle sampling.....	62
Figure 70 Order content FFT	63
Figure 71 Comparison of order plot before and after orders removed	63
Figure 72 Frequency domain with harmonics removed	64
Figure 73 Order removed FFT of higher speed run	64
Figure 74 Spectrogram of Runup test for strain	65
Figure 75 Average 2D plot of Runup test.....	65
Figure 76 Constant run test of strain	66
Figure 77 Harmonics removed Strain Frequency plot	66
Figure 78 Order removed Frequency plot of higher speed test run.....	67
Figure 79 Time domain strain signal	67
Figure 80 DIC image where some markers are picked up while others are not.....	68

Figure 81 Distinction between left and right components.....	68
Figure 82 DIC 3D image of the reference state.....	69
Figure 83 DIC 3D image of an image during running.....	69
Figure 84 DIC time domain signal.....	70
Figure 85 FFT of the undersampled DIC signal.....	70
Figure 86 Fan-paper representation of location of undersampled frequencies.....	70
Figure 87 Zoomed in plot on area of interest for natural frequency.....	71
Figure 88 High speed DIC test run.....	71
Figure 89 Undersampled frequency plot of optic signal.....	72
Figure 90 Undersampled frequency plot of optic signal.....	72
Figure 91 a) Experimental rotor setup, b) Updated FEM model setup.....	75
Figure 92 Damage modelling, a) FEM, b) Experimental.....	75
Figure 93 1st torsional mode shape of updated model.....	76
Figure 94 Selected elements to be measured.....	77
Figure 95 Detail of MPC, motor-element and torque load at motor-end.....	78
Figure 96 Strain response as a result of motor torque.....	78
Figure 97 Strain response from a higher torque load.....	79
Figure 98 Excitation torque load applied at free-end.....	79
Figure 99 Strain response from external excitation.....	80
Figure 100 Frequency variation as a function of damage.....	81
Figure 101 Frequency ratio comparison.....	82
Figure 102 Percentage error between Experimental and FEM results.....	82
Figure 103 FFT comparison of undamaged and damaged cases for optic sensor.....	83
Figure 104 FFT comparison of undamaged and damages cases for strain gauges.....	84
Figure 105 Frequency section of reversed frequency base-band.....	85
Figure 106 Subplots of each damage case in the base-band range showing peaks representing torsional frequencies.....	86
Figure 107 Strain due to weight.....	10.1-99
Figure 108 Strain and motor torque due to motor load.....	10.1-99
Figure 109 Torque (N.m) strain relation.....	10.1-100
Figure 110 Torque (V) strain relation.....	10.1-100
Figure 111 Calibrated Torque values.....	10.1-100

List of Tables

Table 1 Dimensions of setup.....	27
Table 2 Convergence study.....	30
Table 3 Material properties (Callister W.D., 2003).....	32
Table 4 Comparison of FEM and Analytical results.....	34
Table 5 Results of damaged rotor.....	35
Table 6 Calibration table parameters.....	53
Table 7 Result comparison between experimental and updated FEM model.....	76
Table 8 Conversion of damaged frequencies to base-band frequency of undersampled methods.....	84
Table 9 Representation of undersampled frequencies obtained.....	87

Nomenclature

Symbol	Description	Units
English Letters		
A	Cross sectional area	m ²
c	Damping	N.s/m
C	Damping matrix	N.s/m
E	Elastic modulus	Pa
F	Force	N
f	frequency	Hz
I	Flexibility factor	
I	Cross sectional properties	m ⁴
J	Mass moment of inertia	kg.m ²
J	Torsional mass matrix	kg/m ²
k	Stiffness	N/m
K	Stiffness matrix	N/m
L	Length	m
l	Length	m
m	Mass	kg
M	Mass matrix	kg
N	FFT lines	
O	Orders	
R	Radius	m
r	radius	m
t	Time	sec
T	Torque	N.m
u	Displacement	m
\dot{u}	Velocity	m/s
\ddot{u}	Acceleration	m/s ²
X	Frequency domain content	Hz

Greek Letters

θ	Angular displacement	rad or °
$\dot{\theta}$	Angular velocity	rad/s
$\ddot{\theta}$	Angular acceleration	rad/s ²
ρ	Density	kg/m ³
α	Angular acceleration	rad/s ²
α	Crack depth	m
π	Pi	
ε	Strain	mm/mm
ω	Vibration frequency	rad/s
$\bar{\theta}$	Nodal amplitude	
ω^2	Eigen-value	

Subscripts

k	Counter increment
max	Maximum frequency range of interest
p	Polar moment
s	Sampling frequency
x	Sectional properties about x-axis
y	Sectional properties about y-axis
z	Sectional properties about z-axis

1. Chapter 1- Introduction and background

1.1. Introduction

Rotating machinery form the backbone of almost every industrial plant. Shafts are key components in machinery since they transmit mechanical energy. Common uses are in turbines, pumps, compressors and generators. These components operate on daily basis at high rotational speeds and develop extreme forces and loads. Since the shaft operates through variable loads and conditions, the stresses induced on it also change which results in cyclic loading and stresses occurring. When coupling these high variable loadings with stress raisers present from shoulder and keyways, it results in cracks forming on the shaft which is known as crack initiation.

With continuous loading and operation of the machine, the crack will start to grow and propagate through the shaft. Crack propagation can occur over a time period and once it reaches a certain critical length, the shaft can suddenly fracture in a brittle manner. In machines that operate at such high speeds, this can be catastrophic and dangerous to machines and people working in the vicinity. It is also extremely costly in terms of repair work as well as downtime the company faces.

Turbomachinery used for power generation must invariably run for many months and even years without stopping. During this lifetime, the shaft will experience various complex loadings occurring and if crack initiation and propagation does occur, it can result in failure and thus downtime which will be extremely costly for the company and lead to unwanted and unpleasant blackouts for residents and businesses alike. A summary of this effect may be viewed in the schematic diagram shown in Figure 1 below. It is clear that this cycle is extremely unwanted.

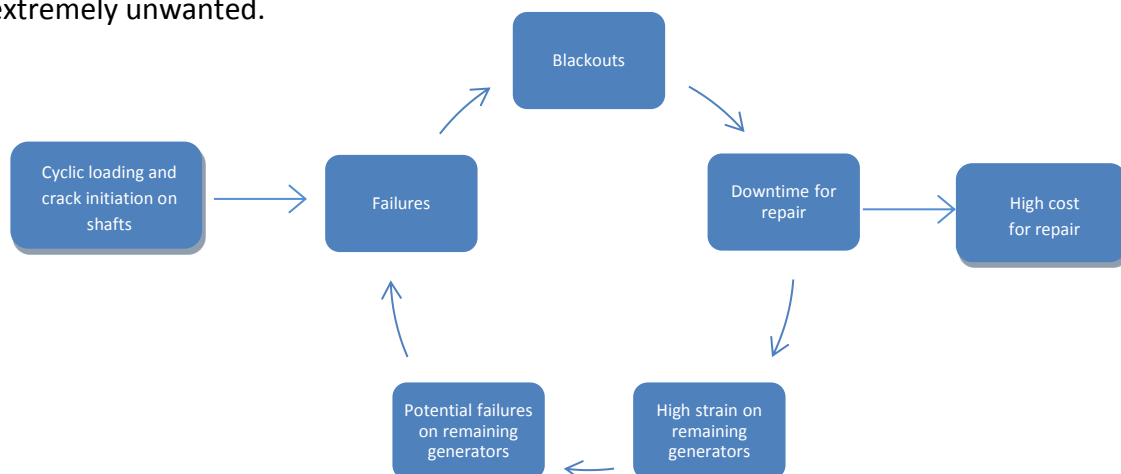


Figure 1 Potential failure cycle in machinery

In order to prevent this sort of catastrophic and costly failure, the shaft's "health" should constantly be monitored. There are various types of maintenance plans that are available and in use. Breakdown maintenance is the type whereby the machine is run until it breaks

down and once this occurs, it is then repaired or a new installation is done. Time-based preventative maintenance is a technique whereby the machine is stopped after a certain pre-defined time period and the components are inspected for wear. This is done regardless of whether the machine is in good operating condition. The last is condition based maintenance. In this approach the machine is constantly monitored and changes in its behaviour is a sign of abnormal behaviour and results in the machine being stopped and faults are investigated. This ensures that the machine is only stopped when faults occur and therefore require no unnecessary maintenance checks.

Such an online monitoring technique which relies on detecting the minute changes in the dynamic behaviour of the system due to cracks changing the stiffness properties of the shaft must be developed and forms the basis of this project. The introduction of such a technique to a system modifies the above diagram shown in Figure 1 to something like that shown in Figure 2 below.

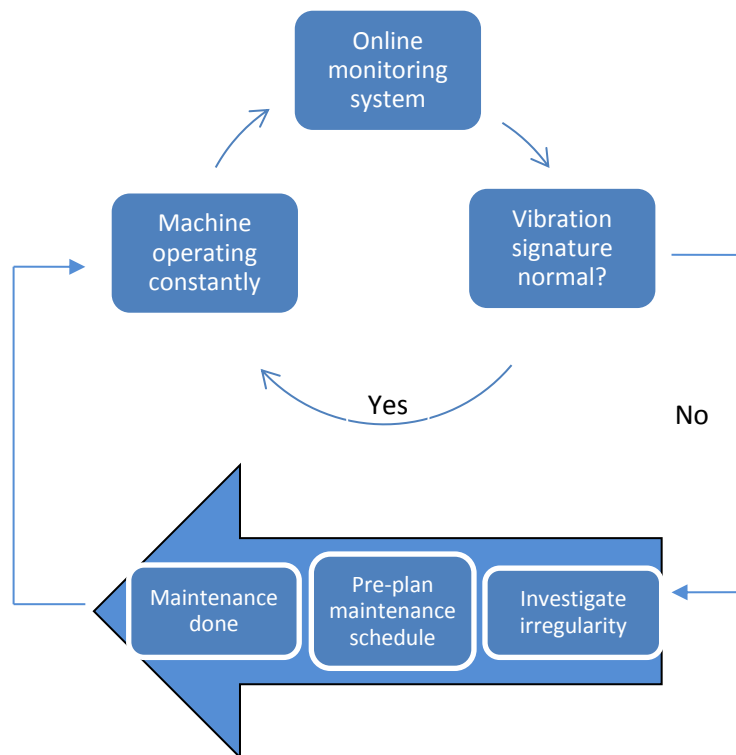


Figure 2 Online monitoring machine cycle

In order to detect these changes, one needs sound equipment capable of measuring the data accurately. In the past, the shop foreman would typically measure the vibration signal by pressing the end of a screwdriver against a bearing housing and the handle against his ear. In this way the pure vibration signal from the bearing would be analysed in his brain. This was a very reliable method but was dependent on the operator's skill. Thus instruments that could provide the same function and that were not dependent on the user, were developed.

With the development of the FFT algorithm, analysers became very powerful in capturing useful frequency data in order to monitor a machine. The frequency range monitored is however limited as stated in the Nyquist theorem. This theorem states that the frequency range that can be investigated is half the sampling frequency. Thus, for cases of high range frequency content, very high sampling is required.

In some cases even though the analyser is capable of sampling at a high rate, it may be limited by the capabilities of the equipment. For instance, when measuring data using photogrammetry systems, the sampling may be limited by the capture rate of the camera. In these cases undersampling methods are used to investigate the system. The undersampling approach has been successfully used for image resolution enhancement, construction of high-speed periodic signals from incoherent sub-sampling algorithms and multi-channel laser vibrometry systems amongst others. However there are plenty of measuring equipment like accelerometers, fibre optic sensors and telemetry systems that are capable of measuring at the correct sampling rate. Some may yield better responses and results than others due to the fact that they each measure different parameters and it all depends on how sensitive these parameters are based on the setup.

In the past it has often been found that lateral vibration measurements have been done with quite successful results. However recently there has been increased interest and studies done on torsional techniques. These have shown good potential of obtaining desired results. This forms the main focus of the present study. Investigations of three different torsional techniques are used for measuring the torsional response of a system. Based on the different results obtained, one can conclude which equipment is best suited for certain operating conditions.

This dissertation contains a literature study on vibration techniques and monitoring methods. A brief discussion of how the finite element method (FEM) will be utilised is given. Some examples of existing methods obtained from literature are touched upon. From this a detailed problem description is stated. The experimental setup, testing, comparison with finite element results, discussion of results and conclusions and recommendations follow in the subsequent chapters.

1.2. Literature Study

1.2.1. Failure cases

There have been cases of turbogenerator failures due to cracks propagating in them since the 1950s. In the period between that time up to the 1970s, generator capacities increased from 60MW to around 500MW (Ishida, 2008). This meant higher loads and stresses which resulted in a higher risk of failures. In some cases it had been hard to find the cause of failure due to the rotor being completely destroyed.

The major energy crisis in the 1970s also led to the slowdown in the construction of newer plants. The majority of equipment back then was commissioned in the 1960s and with a

design life of 30 years. These equipment have long reached their design lives and it is expected that failure from crack initiation will become a growing problem in the future (Ishida, 2008).

Steam turbines operate at high speeds and if a crack is initiated, it is quite possible for it to burst and allow broken pieces to be sent violently and dangerously into the air. This has occurred in various instances. In 1950 an LP-turbine from the Nijmijen unit in Holland failed from brittle fracture. Similar cases of LP-turbine failure were also found in 1951 in Germany on their Siemens unit and in 1954 in the USA on the Ridgeland No.4 unit. In 1972 in the Kainan No. 3 unit in Japan, an LP-turbine failed due to improper installation as well as high vibration through resonance. In 1974 in the USA Gallitin No. 2 unit, an IP-LP-turbine failure occurred as a result of creep, fatigue and embrittlement after 106,000 hours of service (Kobayashi, 1974).

Another serious failure occurred in 1970 when an LP turbine in Japan burst during a running test, which led to the deaths and serious injuries of over 60 people. After further investigation, it was found that cracks initiated due to high stress concentration from ground holes (Kobayashi, 1974; Ishida, 2008).

Rankin et al. (1956) reported that in 1953 a steam turbine at the Tanners Creek power station in the USA went into sudden vibration and failed after a 160° section of the shaft broke out. In a different case in 1954, Schabtach et al. (1956) reported a generator that burst while being balanced in Arizona in USA. Before failure of this generator several cracks were found.

There have been situations where cracks were detected before failure. In 1956, Coyle reported that there had been a development of fatigue cracks due to low nominal gravitational bending stresses. It was found that two of these cracks propagated to over 75% of the shaft section. In the third case a crack developed all around the circumference and had propagated to 1/16 of an inch. Yoshida reported four cases in the 1970s whereby cracks were found in steam turbine rotors and concluded that it was caused due to cyclic thermal stresses which were present during the frequent start up and shut down of the system. Paterson also reported that three cracks were discovered at the Ferrybridge power station during 1972-1974 (Ishida, 2008).

In other cases, Laws (1971) reported four cracked rotor incidents. A 40% transverse crack was found to have propagated on a 500MW turbine generator. A 30 inch long circumferential crack on a 60MW turbine generator, the main rotor of a 660MW turbine generator contained a 45% transverse crack and on one of the 350MW turbines, a complete circumferential crack was also found (Ishida, 2008).

Dimarogonas et al. (1987) also reported a crack found in a 300MW turbine generator in one of the power plants in Greece. They also reported that in many cases, the occurrence of a

crack resulted in an abnormal increase in the vibration of the system, and that detailed symptoms of the cracks were obtained through vibration diagnosis techniques (Ishida, 2008).

After the 1970s, there had also been several cases where cracks were found in nuclear power plants. This was an even more serious issue because of radiation exposure. Ziebarth et al. (1981) investigated the vibration history of two 1300MW nuclear plants in the USA and Germany. In the USA they found that the vibration had started to increase and that an excitation at two frequencies was present during rundown. In Germany there had been considerable vibration in the vertical and horizontal directions and had started to increase six days prior to shut down. There had also been a case where a pump shaft had failed due to a fatigue crack that had propagated from a groove (Ishida, 2008).

At the nuclear power plant in Darlington, a crack growing to over 25% of the shaft's cross section was found on a 935MW turbine generator. The vibration data revealed that the amplitudes of the resonance and its harmonics had increased as a result of the crack (Sanderson, 1992).

In 1986 a pump shaft in Crystal River nuclear power plant broke due to a fatigue crack in a groove. Another crack developed in a separate part of the same machine in 1989. In 1990, a crack that had propagated to 25% of the cross section was found in a generator rotor of the 935MW turbine generator of Darlington nuclear power plant (Ishida, 2008).

In 2002 the Russian Kashira power station had a destruction of a 300MW turboset when a cracked shaft had burst during operation (Machorro-Lopez, 2009). Similar cases were also found at the Tennessee Valley Authority Gallatin No. 2 power plant in the United States of America in 1974 and the accident in 1988 in Germany due to a 330MW steam turboset explosion.

There have indeed been many cases of failures in power plants as a result of crack initiation and propagation. There is a possibility of other cases which have not necessarily been reported to the public. There are also various cases where fatigue crack failure is not only limited to turbine generators in power plants. One such case is a crack reportedly found on a wind tunnel fan shaft. The crack had grown over 120° of the cross section (Ishida Y, 2008).

1.2.2. Online monitoring

As can be seen from the cases above, damage in rotors is critical if present and can lead to catastrophic failure if undetected. An online monitoring system is crucial for these large machines. Heng et al. (2009) did a study on rotating machinery prognosis which deals remaining operational life, future condition, or probability of reliable operation of an equipment based on the acquired condition monitoring data. This sort of method ensures to reduce downtime, spares inventory, maintenance costs, and safety hazards.

There are various maintenance strategies currently in use. These range from breakdown maintenance, preventive maintenance and condition-based maintenance (CBM). Amongst

these, CBM is the most attractive. This method monitors machinery health by continuously measuring the condition of the system without interruptions during normal operation (Heng et al., 2009). This method essentially becomes a fault detection system (FDS) as any changes seen in the data collected often relates to some damage or irregularities of the system.

As mentioned earlier, FDS offers similar benefits as CBM (Hameed et al., 2009):

- Avoidance of premature breakdown- Detecting faults early and allowing necessary processes to be implemented before failure.
- Reduction of maintenance costs- unnecessary maintenance is avoided.
- Supervision at remote sites, remote diagnosis- Through wireless technologies, systems can be monitored from long distances.
- Improvement of the capacity factor- Correct maintenance plans and strategies can be planned before damage evolves to a critical state.

As seen, CMB and FDS are quite advantageous to be implemented on machinery. There are various methods and parameters that one may use for monitoring. In rotating equipment, the vibration method is more commonly used and also forms the root method for this study. This technique involves monitoring the frequency content of the system, such as operating speeds, natural frequencies and the changes to these parameters that may result as a consequence of some fault being present in the system. There are different sensors that may be used for vibration measurement. Accelerometers, velocity sensors and proximity transducers are among a few of them. Strain methods may also be used by analysing the strain results in the frequency domain.

1.2.3. Research developments

From the failure cases mentioned before and the increasing advantage that online monitoring brings, it has prompted many researchers to conduct detail studies in this field. The study of cracked rotors and monitoring of such rotors became popular over the last four decades (Kumar, 2009). Many researchers used different methods of modelling a rotor shaft system, from using lumped spring-mass systems, Timoshenko beam elements to commercial finite element software. Experimental work was also often done and trends were developed from these results. In recent years more research is done on optimizing existing post-processing methods in order to obtain clearer results. The various works done by many researchers are discussed below.

There had been various studies using lateral and torsional techniques. Each showed good online monitoring capabilities for damage detecting. Recently there has been more interest in torsional analysis with equipment like the fibre-optical sensor using coded tape and torsional laser vibrometry becoming more popular. Maynard et al. (2001) also showed that through torsional vibration, one could obtain the torsional frequency as well as blade bending frequencies. Torsional vibration has thus shown good potential for damage detection in rotating machines.

a) Analytical and numerical models

Various investigations were conducted to simulate a rotor setup and to analyse the torsional dynamics with and without damage. One of the basic methods is to use a lumped spring-mass system which considers the shaft to be light and neglects its mass, treating it as torsional springs. The disks on the model are treated as the masses with their moments of inertia. Raskovic (1949) investigated this for several boundary condition states using the Lagrange differential equation for a torsional case (Raskovic, 1949). Aspragathos (1981) investigated fatigue damage of turbine-generator shafts. He separated the model into electrical and mechanical systems. For the mechanical system, he used a 2nd order linear differential equation to represent the dynamic model to obtain the torsional response.

Bumby et al. (1982) used mathematical models in the form of a lumped spring mass system and a finite element model to compare the undamped natural frequencies and mode shape of the torsional modes to an existing superconducting turbo-generator containing a double rotor structure. This was done by finding an equivalent stiffness for the inner and outer rotors using different cylinder models representing the rotor shells and eventually developing a simpler lumped mass model for determining the torsional frequencies. This simplified method proved to be advantageous for system studies and the results showed good comparison of the frequencies between the exact solution and the lumped model and the finite element model.

Research then started investigating models using finite element methods using simple Timoshenko beams. This meant discretizing the model into small elements. Each element would therefore have its own mass and stiffness which are represented by matrices (Craig, n.d.). When modelling damage, many of them used experimental techniques to see how the flexibility of the shaft changed. This was done by Dimarogonas and eventually the flexibility could directly be related to the depth of a crack through an equation (Dimarogonas, 1981). Papadopoulos investigated the dynamic behaviour of a shaft with a transverse crack in it. He applied the FEM approach by modelling a rotor using beam elements with rotational DOFs. He then modelled damage into an element by modifying the stiffness using the flexibility factor equation. The free vibration problem was solved for the first three torsional natural frequencies and it showed a decrease as was expected (Papadopoulos, 1992).

This technique was used successfully by more researchers. Gounaris et al. (1988) looked at modelling a crack in a finite element model of a square cross section beam and investigated lateral vibration. Sekhar et al. (1991) did a similar study on a round cross section shaft and looked at crack detection and vibration characteristics of cracked shafts. In 1997, the dynamic analysis of a rotor system containing a slant crack was investigated using the FEM approach (Sekhar et al., 1997). Sekhar again studied a rotor in 1999, but this time a shaft containing two transverse open cracks. Finite element analysis was done for the rotor setup for flexural vibration (Sekhar, 1999).

There have also been various investigations into the types of damage introduced into the system. The majority of the above research was only numerical and did not involve experimental analysis. When experimental investigations were done, it was either a notch, cut or sawed into the shaft, or a proper fatigue crack grown into the shaft using three-point-bending cyclic loading. Recently Kenneth Maynard and Martin Trethewey together with numerous colleagues did considerable amount of investigations on fatigue grown cracks. Wendtland reported work on damaged shafts by machining slots into them resulting in an open crack, although he clearly stated that his results were not applicable to real cracks - only to saw-cuts (Dimarogonas, 1996).

As commercial software became available, modelling slowly started to move in that direction. This ensured that each model was represented by a vast number of elements and nodes which would increase the accuracy of the model. Lissenden et al. (2006) investigated the response of a fatigue crack grown in a stainless steel shaft. Before the experimental setup was done, a 3D FEM model was built using ANSYS FEM software. When modelling damage, the nodes at the crack location were simply not connected. This obviously meant an open crack case which is not exactly what happens in a fatigue crack but results showed good comparison to the experimental results. Machorro-Lopez et al. (2009) did similar simulation and experimental work on identifying damage in shafts using active sensing. A detailed 3D FEM model was also built in ANSYS.

b) Experimental techniques

Fibre-optic sensors have gained significant interest in industry. This is mainly because of their ability to perform its function in hostile environments and high electromagnetic-interference prone areas, while at the same time providing advantages in terms of ease of application (Batchellor et al., 1990).

In recent years Kenneth Maynard and Martin Trethewey have done a considerable amount of work on torsional vibration measurement. In 1999, a feasibility study using non-contact methods was done for detecting blade damage on shaft using torsional vibration techniques. These non-contact methods were through the use of coded tape and a fibre-optic sensor. Results showed a clear change in blade natural frequency as a result of blade damage. Their results were further verified through a finite element model whereby the crack was modelled into the system as torsional spring of different stiffness than the rest of the shaft (Maynard et al., 1999).

Further studies also revealed that in some cases, the harmonics of the setup is very dominant and results in the system not being excited enough in order to adequately detect some low level torsional frequencies. Using order resampling followed by the removal of these orders and then frequency resampling, increased the effective dynamic range and improved the ability to identify the frequencies (Maynard et al., 2001). This laboratory experiment was then extended to industrial applications on fans in a wind tunnel of the

National Full-Scale Aerodynamic Complex (NFAC) and an aircraft jet engine. The results demonstrated that this method of testing is feasible (Maynard et al., 2002).

Using their research developed above and together with other colleagues, they then investigated the torsional vibration signature of a shaft on which they grew a fatigue crack using the three-point-bending technique. These tests were done on various crack depths up to a maximum of 60% of the shaft diameter. Results revealed a nonlinear relation between crack depth and frequency (Bieryla et al., 2005).

Other fibre-optical methods using Digital Image Correlation (DIC) techniques were done in 1985 by Chu et al. Their basic application was to measure macroscopic parameters such as strain and displacement from which stress could be obtained. This was done by taking an image of an object in one state and comparing it to an image after a time increment of Δt . Each object had a speckled pattern on it that served as the comparison variable as seen in Figure 3. The results showed accurate rigid-body translations and rotations as well as deformation gradients which were related to strain which may be viewed in Figure 4 (Chu et al., 1985). Similar tests were also performed by Mguil-Touchal by investigating the strain field for XES steel in its plastic domain under plane strain condition. A feasibility study on the strain field measurement was done by conducting bending tests on a specimen with impact loading. In a separate case, mechanical characterization of human spongy bone amongst other tests, were also done for full field strain measurements. Their investigations proved that the DIC had become another successful tool for displacement/strain field measurements (Mguil-Touchal et al., 1997).

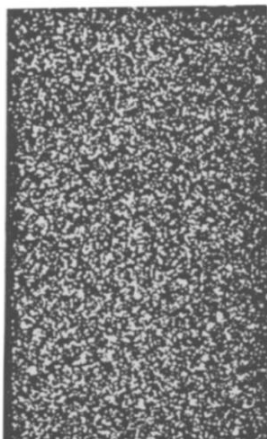


Figure 3 Speckled pattern on test object (Chu et al., 1985)

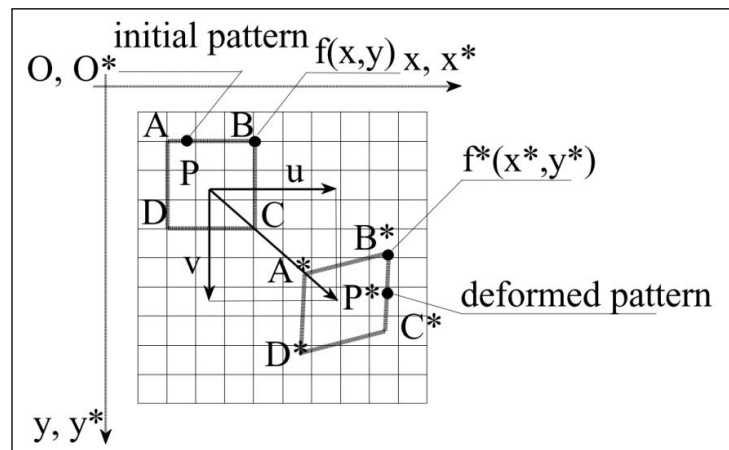


Figure 4 Deformed pattern as a result of strain through use of pixel correlation (Mguil-Touchal et al., 1997)

The use of the DIC system gradually progressed from statically loaded strain cases to more dynamic cases. Lall et al. (2007) investigated the transient dynamics of impact loading on electronic equipment. For this the use of the DIC with ultra-high-speed imaging was successfully used for full-field measurement of transient strain. Recent investigations involved using the DIC system for proper vibration testing. From the increased development in this technology, it has allowed DIC methods to measure the mode shape and deformation of a vibrating structure. Helfrick et al. (2008) presented this after doing tests, analysis and

correlation of traditional modal data along with the DIC approach for comparison to a finite element model. His results from the DIC method for measuring operating shapes were promising and there was a strong correlation with the finite element model results as well as the traditional modal impact test results.

The above study was investigated further by doing a comparison study of non-contact measurement techniques. This involved comparing tests between the DIC system and a 3D laser vibrometer. These were then also compared to a traditional accelerometer. Tests were again done on the dryer base. The results showed that each technique applied in this comparison has its own advantages and drawbacks, but in the end all methods yielded good consistent measurements. The biggest difference between traditional methods and optical techniques is the approach taken to measure multiple modes. Accelerometers and laser vibrometers measure multiple modes over a broad frequency range, point by point. Conversely, the optical approach measures all points simultaneously, one mode at a time. The main advantage of DIC is the immense number of effective measurement points and the fact that strain throughout these patches can be measured directly, whereas the laser and accelerometer can practically only be measured at discrete points. This investigation showed that the DIC method successfully measured mode shapes and correlated well with the laser vibrometer and accelerometer (Avitabile et al., 2010).

Helfrick also implemented the DIC method to rotating equipment by measuring the out-of-plane vibration of fan blades. The technique used a pair of digital cameras along with a stroboscope to make full-field measurements of displacement without contact and while the blades were rotating. Capturing the fast motion of the fan with a digital camera requires a shutter time which is short enough to prevent motion blur. However, a short shutter time does not allow enough light to be recorded by the camera's pixel array under normal lighting conditions. Therefore a stroboscope was used and solves both the problems of needing a sufficient amount of light in a short shutter time. A quick flash will both illuminate the object and prevent motion blur. Disturbances were introduced by adding weights to two of the blades. By consistently taking images during operation, a time domain out-of-plane displacement of the blade could be obtained. The results showed that 3D DIC measurement methods using a stroboscope can be used to successfully obtain shape information of rotating body (Helfrick, 2009).

Before advances in the DIC method, the majority of strain measurements were done using strain gauges. Strain gauges are often associated with tensile testing to develop stress-strain curves of a material. They are commonly applied for local deformation studies. Carboni had done compliance measurements near a crack tip for crack closure evaluation. By doing this, mechanisms which control the effects of fatigue crack growth was studied (Carboni, 2006).

Until the 1980s dynamics were often measured using conventional transducers that measure displacement and differentiating these signals to get velocity and acceleration. Soon after, interest had developed into using strain for modal analysis in order to capture

dynamics of systems (Vari, 1997). In 1996, Yam and Leung investigated the relationship between strain and displacement modes for an elastic vibrating structure. This was carried out theoretically and experimentally. The relation showed that both were able to obtain good mode shapes with the strain being more sensitive to local changes as was expected (Yam et al., 1996). According to Vari, it was found that using the strain modal testing (SMT) techniques were less favourable than the displacement method. They critically assessed its potentials and downfalls (Vari, 1997). Kim et al. (2000) used modal testing to identify damage on steel members. They investigated the modal frequencies, displacements and strain mode shapes. Changes in the frequencies and mode shapes were detected.

1.3. Project overview and objectives

1.3.1. Chapter overview

This chapter reviewed the literature relating to online monitoring, damage detection using various methods and results obtained by other researchers utilizing and investigating these methods. It is essential to understand what has been done, what works and what potentially new innovative methods could be investigated further.

To briefly summarise this chapter, it has been clearly stated and noted how important online monitoring is in industry and that if not done and proper maintenance schedules are not followed, this can lead to disastrous failures. Many authors have modelled rotors using various numerical techniques and have done so successfully. Experimental techniques have also yielded successful results. The fibre-optic sensor with coded tape has been implemented in industry with great confidence in its ability. The DIC method has shown promising results for static cases and recently in dynamic cases as was seen for the rotating fan blade whereby modal shapes through strain methods were developed. Although various methods have been tested and some show good potential, they have not been compared so as to know which forms the best method in certain conditions. Based on these facts the objectives of this project may be stated.

1.3.2. Objectives

- Investigate and compare results from various measurement techniques for online monitoring of the torsional dynamics of damaged and undamaged rotors under normal constant speed operating conditions.
- At the same time, achieve a better understanding and demonstrate the practical use of undersampling methods for frequency based measurements and online monitoring.

In order to reach the two main objectives above, a number of smaller objectives need to be achieved. These are listed below.

- Carry out a numerical investigation of a rotor system by modelling a shaft using finite element methods.
- A modal analysis is to be conducted to understand the dynamics of the rotor.

- Damage is to be modelled into the rotor and its effect on the system must be investigated.
- An actual rotor is to be manufactured for experimental testing. It is to be ensured that this closely resembles what was modelled the FEM in order better verify the results.
- Testing is to be done using three different torsional methods. These would be the fibre-optic sensor, strain gauge telemetry system and the DIC system.
- Detailed analysis of the frequency content obtained from each method must be analysed.
- Damage is to be inserted in to the system in increments of increasing severity. With each insertion of damage, the frequency data is to be studied and any changes noted.
- Based on these results the advantages and disadvantages of each method must be stated in order to identify the most favourable method.

2. Chapter 2- Mathematical modelling and processing techniques

2.1. Overview

This chapter focuses on the theoretical aspects of the study. One needs to understand the mathematical formulations and theorems involved for carrying out an analysis. This chapter discusses some basic vibration theory associated with dynamics of a system and a brief discussion of how this is applied to the FEM analysis. The discussion then moves to the post-processing of the experimental testing related to time and frequency domain content used for the fibre-optic sensor, strain gauge telemetry and the DIC system. Undersampling methods used for the DIC system are then discussed.

2.2. Basic Vibration and Finite Element Theory

Depending on the excitation, structures and machines vibrate at different frequencies. The responses to these loads are very interesting to engineers and designers. Many failures are caused due to excessive vibrations. It is therefore vital to understand the dynamics involved in a system.

If the excitation coincides with natural frequencies, an object will inherently vibrate with larger magnitudes in so-called natural mode shapes which are associated with the natural frequencies. As the frequencies increase the mode shapes become increasingly complex and may include out-of-plane bending as well as torsional behaviour. This study focuses on damage detection by consideration of the torsional natural frequencies of a shaft. If damage is present, it will result in the stiffness decreasing which results in a reduction of the natural frequency which is monitored.

To study this in FEM, a model is built up with multi-degree-of-freedom (MDOF) models comprising thousands of nodes and elements. Each element has mass and stiffness associated with it and is represented in a matrix format. By substituting these matrices into the equation of motion and solving, the free vibration eigenproblem is encountered. From this eigenvalues and eigenvectors which contain information about natural frequencies and modes shapes are obtained. Detailed derivations of this may be found in Cook et al. (2002).

2.3. Fibre optic Sensor

The fibre optic sensor uses digital time interval techniques for the measurement of torsional vibrations in rotating shafts. Through high-speed timers this technique is capable of detecting passage times or “zero crossing” in a carrier signal from a multiple pulse per revolution encoder tape mounted on the shaft (Resor et al., 2005). The result of this is a square wave in the time domain ranging from 0 V to 5 V or depending on the sensor’s output voltage.

When looking at an ideal case of constant speed running and assuming zero vibration present, the time signal should be a perfect square wave with each pulse having the same constant time increment. This can be seen in Figure 5 a). Due to vibrations that occur during

operation, the pulse size will not be perfect each time in a real situation or run. An exaggerated example of this behaviour is seen in Figure 5 b). If the measured signal in b) is compared to this ideal or reference signal in a), the variations which arise are a result of torsional vibration and occur at frequencies associated with the dynamics of the system. These are often hidden within the shaft's rotational frequency and its order content.

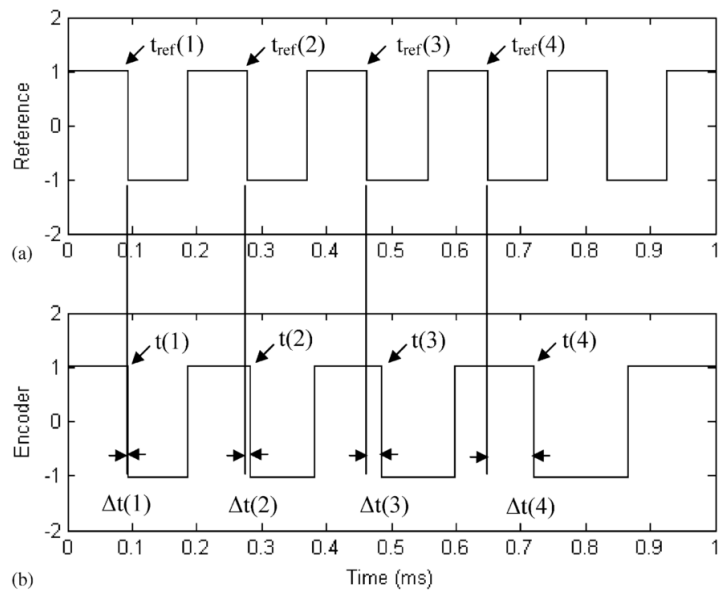


Figure 5 Reference and vibration signal of square wave (Resor et al., 2005)

In order to make proper sense of the signal, one needs to view it in the frequency domain where the frequency content in terms of operational speeds and natural frequencies may be studied. This is done through the use of the Fast-Fourier-Transform (FFT).

This method will be used when carrying out the post-processing of the fibre-optic sensor square wave. From this it is expected that the shaft's operating speed as well as the torsional frequencies will be visible. It was mentioned earlier that the natural frequency may be hidden amongst the operating frequency and its orders. This is a similar scenario that was found in an experiment conducted by Maynard et al. (2001), where they investigated blade natural frequencies through torsional methods, and which was mentioned in the previous chapter.

Order removal is a process whereby the orders are removed from the signal in order to look at frequencies present in the signal other than those associated with the rotational frequency. In order to completely apply this method; the following steps need to be followed (Groover et al., 2005):

- Vibration data is sampled using a constant time basis.

$$x(t_r) = x(r\Delta t) \quad (\text{Eq-1})$$

where r is an index integer and Δt is the time-based sampling frequency.

- Dividing a once per revolution tachometer signal by some integer O means dividing the signal into constant angular sections and therefore the times associated with the constant angles are obtained.

$$\Delta\theta = \frac{360^\circ}{O} \quad (\text{Eq-2})$$

- Figure 6 shows an example of constant time and constant angle sampling. This voltage signal at the constant angle time must be obtained through interpolation and may be done using a linear interpolation function in Matlab assuming the intervals are small.

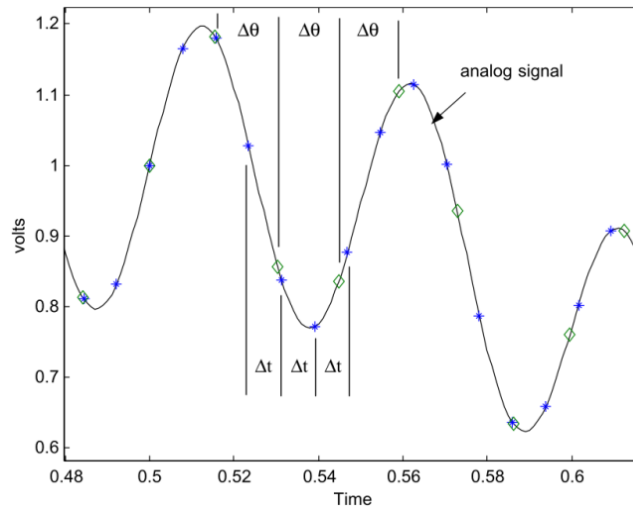


Figure 6 Constant time and angle sampling (Groover et al., 2005)

$$y_i = \text{interp1}(x, Y, x_i) \quad (\text{Eq-3})$$

Where y_i is the interpolated constant angle volt value, x and Y are the constant time sampled data and x_i is the constant angle time vector. Once this is known an equation like Equation 1 for constant time may be written for constant angle.

$$x(\theta_r) = x(r\Delta\theta) \quad (\text{Eq-4})$$

- The constant angle sampled data is transformed via the FFT to the order domain. This is done using the FFT approach mentioned earlier in terms of angle instead of time.

$$X(o_n) = \sum_{r=0}^{N-1} x(\theta_r) e^{-j(2\pi nr/N)} \quad (\text{Eq-5})$$

This results in an order spectrum instead of frequency spectrum.

- The high amplitude orders may be removed by simply taking the smallest value of the neighbouring data.

$$X(o_k) = \min[X(o_{k-1}), X(o_{k+1})] \quad (\text{Eq-6})$$

- An inverse FFT is applied to return to a constant angular increment sampled array, from order content to time content.

$$x(\theta_r) = \sum_{r=0}^{N-1} X(o_n) e^{-1(2\pi nr/N)} \quad (\text{Eq-7})$$

- The constant angular increment sampled array is interpolated to an array sampled with constant time basis using the *interp1* function mentioned earlier.
- An FFT is applied and then standard spectral estimation procedures used to compute the vibration spectra with the high-level orders removed of the new time signal.

Figures 7 and 8 below show a simple example of a time signal of an accelerating shaft, its frequency content showing the high dominance rotational frequency content with some other frequency content and finally the order removed frequency content. The order removed signal clearly shows only the frequency that is investigated.

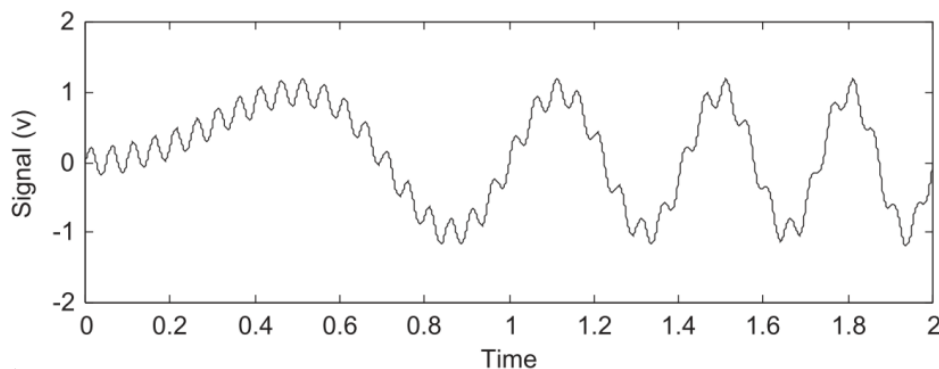


Figure 7 Time signal of an accelerating shaft (Groover et al., 2005)

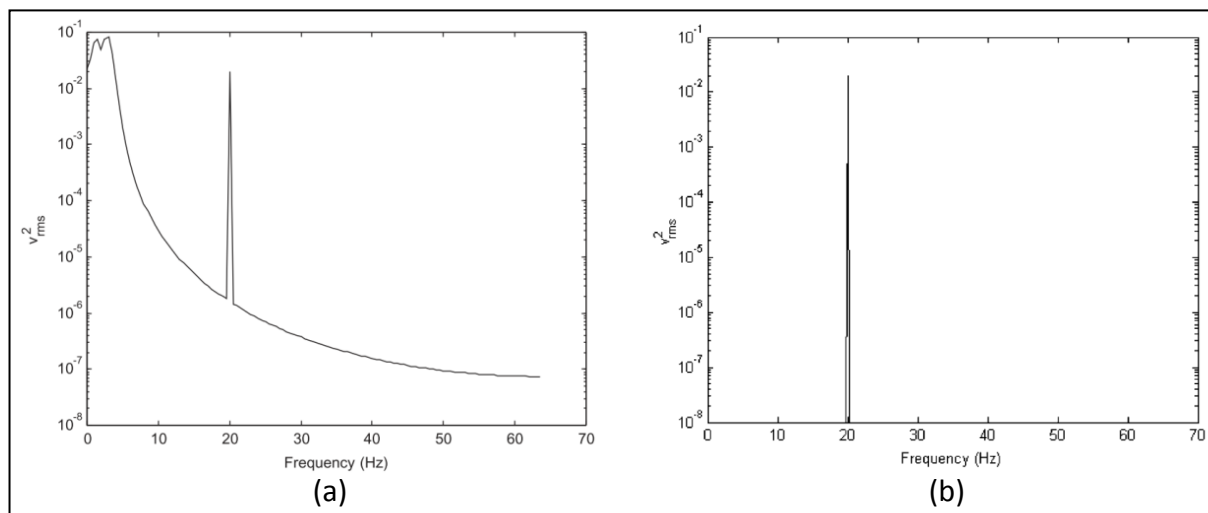


Figure 8 a) Frequency content of time signal showing RPM frequency and a 20Hz frequency, b) Order free frequency content showing only the 20Hz frequency (Groover et al., 2005)

2.4. Telemetry

The objective of using the telemetry system is to measure the torsional strain response of the shaft during operation. When the shaft is twisted, it results in a shear strain and shear stress. The interest in this study would be the strain since it can directly be obtained from the strain gauge. The diagram of a twisting shaft is shown in Figure 9. When the shaft is in operation, it is likely that it may excite some of the modes; therefore it may tend to oscillate

from A to B at the mode frequency with certain amplitude. This will cause the strain to have a natural frequency signal within its strain signal provided the amplitude is high enough.

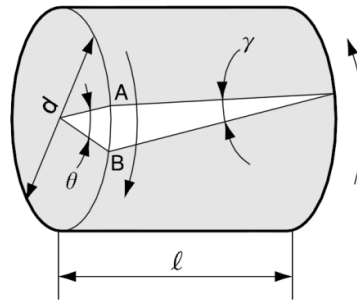


Figure 9 Torsional strain gauge on a shaft (How strain gauges work)

The change in resistance due to strain is extremely small. Thus, for strain measurements a Wheatstone bridge is used in order to convert the resistance change into voltage change which is more sensitive. The diagram below is a Wheatstone bridge setup for using torsional strain gauges. The gauges are shown on the shaft with the dotted gauge mounted 180° on the other side. These gauges are connected as shown in Figure 10.

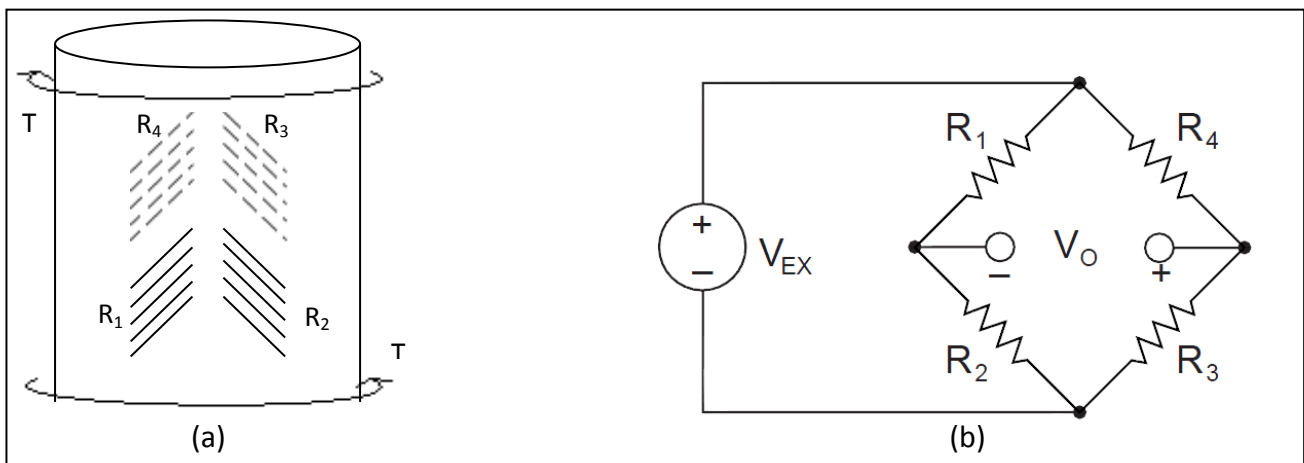


Figure 10 a) Mounting of gauge on shaft, b) Wheatstone representation of gauge resistors (National Instruments, 1998)

If a torque T is applied as shown, it results in R_2 and R_4 extending which alters their resistance in the diagram of Figure 10 b) and therefore a change in the output voltage V_o is resulted. The voltage V_o is obtained from Equation 8 shown below.

$$V_o = \left[\frac{R_3}{R_3 + R_4} - \frac{R_2}{R_1 + R_2} \right] \cdot V_{EX} \quad (\text{Eq-8})$$

Once the bridge is set up, voltage V_o is measured. During elastic strain vibration and deformation, the voltage is directly proportional to strain. Therefore through calibration the relation between voltage and strain is obtained. The calibration method carried out is explained in Chapter 4.5.1. The signal is now a strain measurement in the time domain

containing strain information of operating frequencies as well as possibly any torsional frequency content provided it occurred at a decent amplitude level. The FFT analysis explained under the fibre-optical sensor section is the same method that will be applied for the strain signal.

2.5. Digital Image Correlation system

The DIC system provides a method of collecting data through images. Each image contains pictures of the object and is defined in a pixel format and each image represents a data point in time. Much like how the fibre-optic sensor sampled the square wave voltage at constant time increments, the DIC does the same except that it records images.

The challenge that this system poses is that sampling is governed by the speed of the camera or in a dynamic case, the speed of the camera and strobe lights. The fibre-optic sensor and telemetry system uses the same analyser to record the data which is capable of sampling at 51200 Hz. The DIC camera is capable of capturing images at a maximum of 480 Hz. However the available strobe light is limited to 15 Hz. Therefore with this system the sampling frequency may at maximum only be 15 Hz.

The process of sampling arises from the need to describe analogue time histories in a digital fashion. There are two important principles that need to be applied to the process of digitising analogue signals and recovering valid frequency information. This is stated by Shannon's sampling theorem which in a simple form states:

$$f_s \geq 2f_{\max} \quad (\text{Eq-9})$$

where f_{\max} is the highest frequency desired to be investigated. This equation institutes the limit that can be used to digitise a signal and still identify a certain maximum frequency component. If,

$$f_s = 2f_{\max} \quad (\text{Eq-10})$$

Then, f_{\max} is known as the Nyquist frequency. Therefore if a signal contains frequency content in which 100 Hz is of interest then the sampling frequency f_s must be greater or equal to 200 Hz. If it results that f_s does not conform to the sampling theorem then amplitude and frequency errors will be present. This leads to aliasing which may be seen in Figure 11 below.

The analog signal shows a 1 Hz sine wave. Converting it to a digital format and sampling at 1Hz results in the red line digitized signal which contains no information about the actual signal and is incorrect. As f_s is increased the digitized signal never gives correct information. If only the digitized red signal in the second figure is analysed, it looks like its frequency is 0.769 Hz which is not a representation of the 1 Hz actual signal. However once it is sampled at $f_s=2$ Hz which obeys the theorem, it is seen that the digitized signal reveals a 1 Hz signal.

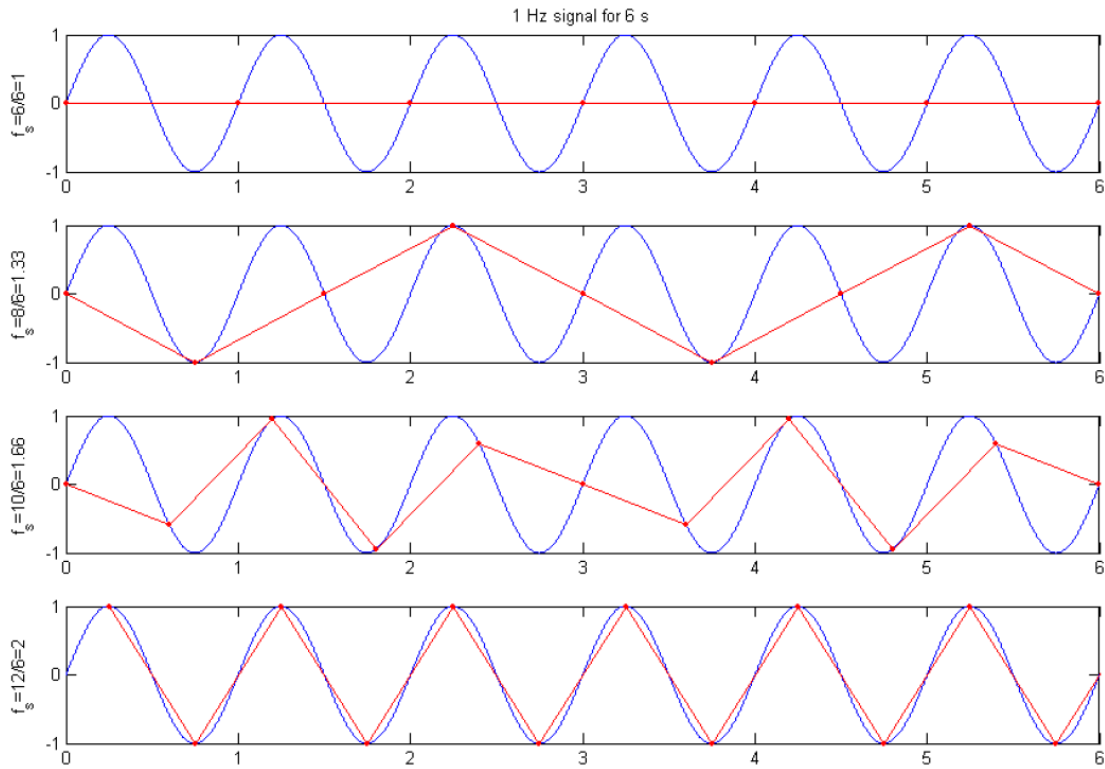


Figure 11 Illustration of aliasing (Heyns, 2008)

In order to be able to use the DIC system, it is essential that an undersampling technique be used. In order to apply this, the time data needs to be sampled correctly in order to at least resemble the actual signal. Assume a shaft rotating constantly at 10 Hz with an additional frequency, in this case a torsional frequency, embedded within it at 80 Hz given by,

$$y = \sin(2\pi 10t) + \sin(2\pi 80t) \quad (\text{Eq-11})$$

In order to sufficiently read these frequencies, it needs to be sampled according to the Nyquist theorem. In this case at least 160 Hz. The above signal was sampled at 1000 Hz over a 30 second period shown in Figure 12. Figure 13 shows this over a 10 second period. It also shows an undersampled signal sampled at a frequency just below the shaft frequency of 10 Hz. In this case 9.9009 Hz was used. Ideally this means that the signal is sample after every revolution plus a Δt period. Thus instead of collecting 1000 data points per rotation, we allow it to rotate once and a bit to get the next data point. Essentially this would collect the same signal but would need a longer time period to collect it over. A zoomed in figure of this is shown in Figure 13.

As seen in Figure 13, the shaft operates at 10 Hz meaning that each revolution takes 0.1 seconds shown by time A. Undersampling would sample at a Δt time later after each rotation shown by time B. The sum of this would yield the actual signal shape but over 10 seconds as shown in Figure 12 above.

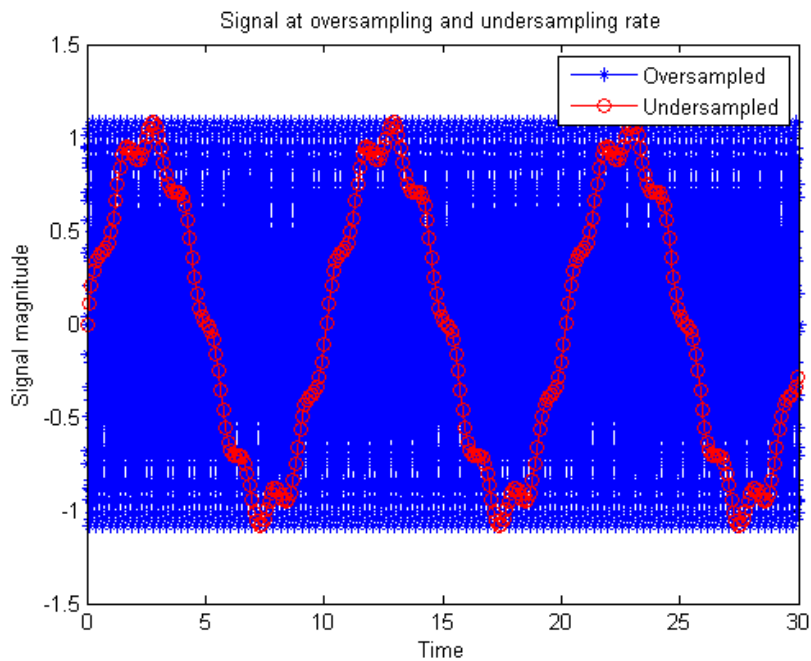


Figure 12 Time signal sampled at two rates

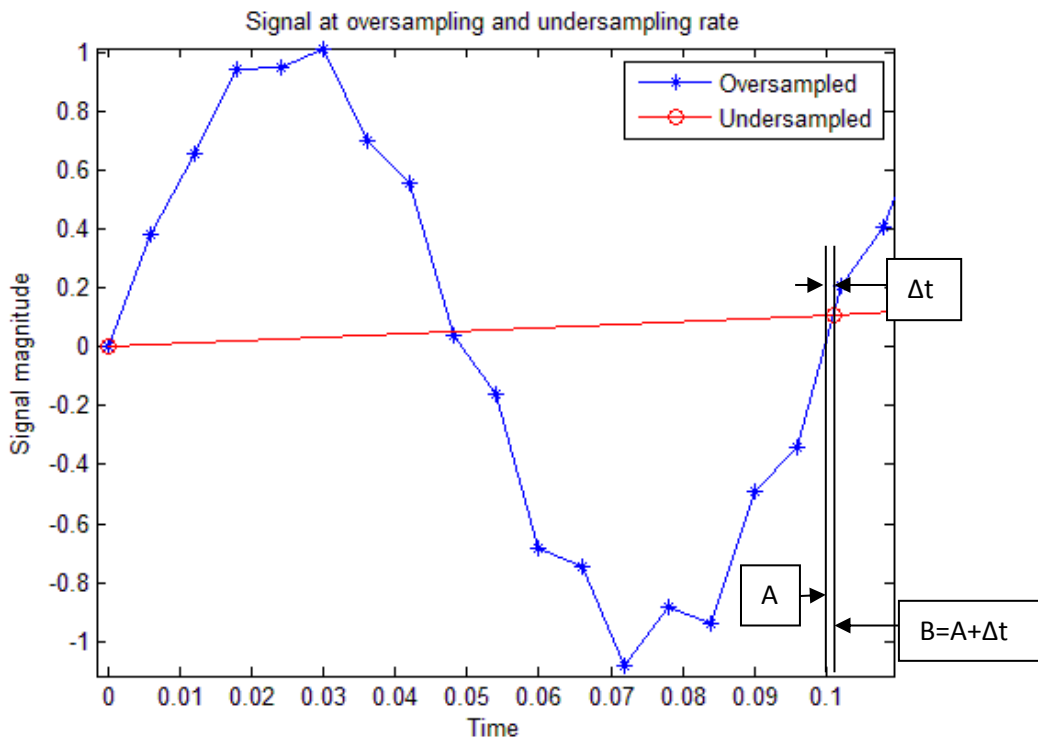


Figure 13 Detailed view of undersampling

For undersampling to be applied successfully, a careful frequency plan must be developed. A method that has been implemented before is the ‘fan-fold’ paper method. Figure 14 shows an example of a frequency spectrum assumed to have been sampled at a correct sampling frequency. If it is decided to undersample the signal at a rate of f_s Hz, which forms a certain fraction of the original signal, the spectrum may be divided into regions every $f_s/2$ Hz. If the signal is then folded in a fan pan paper orientation, all these frequencies will fall in the region of $0-f_s/2$ Hz seen in Figure 15. Note that F_s shown in the figure is the same as f_s mentioned earlier. As the even folds fold back, the resulting spectrum is then reversed. This

concept is the aliasing that was mentioned earlier but now an understanding is developed as to where this noisy spectrum comes from.

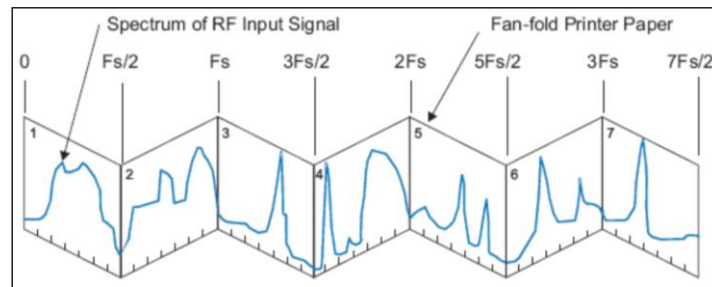


Figure 14 Original spectrum showing undersampled folds (Hosking, n.d)

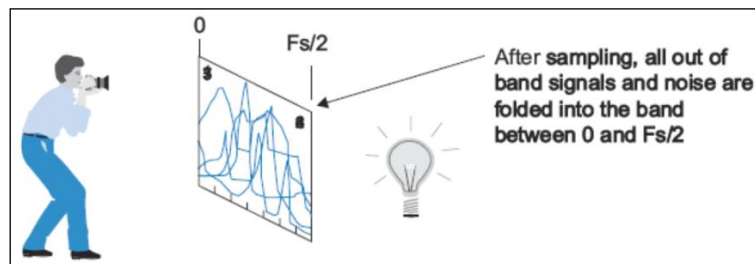


Figure 15 Folded fan to undersampled frequency F_s and showing aliasing (Hosking, n.d)

As seen it is quite hard to pick up the frequencies one is interested in. However, if the frequency of interest lies in a certain region without too much other frequency content present, the signal may be sampled at a lower rate. Figure 16 shows an isolated or band-limited frequency spectrum. When undersampled at f_s and after applying the fan-fold method, the original spectrum may be clearly seen in the base-band.

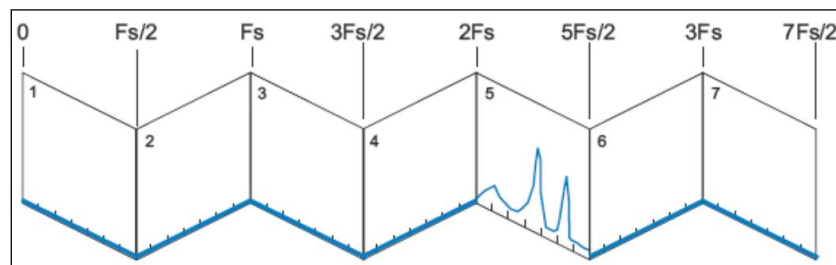


Figure 16 Band-limited frequency spectrum (Hosking, n.d)

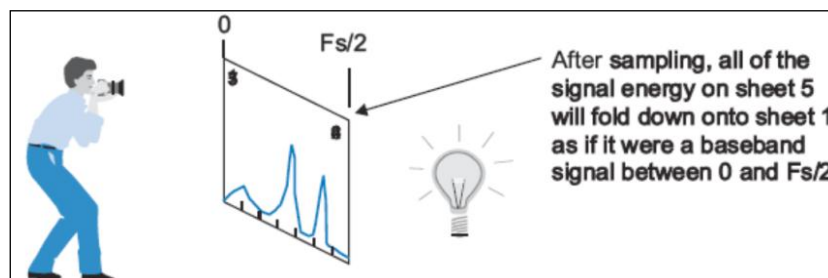


Figure 17 Fan-fold of band-limited frequency spectrum showing desired frequencies (Hosking, n.d)

By implementing this undersampling method, there are a few points to take note of:

- The frequency is indeed band-limited; otherwise a noisy spectrum like that found in Figure 15 is obtained.
- The undersampled frequency does not intersect the original spectrum band-limited signal.
- If the band-limited signal falls on an even fold, its spectrum is reversed. Ideally the undersample rate must be such that this does not occur for simplicity sake.

To show how it works, this technique may be applied to the sine wave example discussed earlier. The undersampling frequency is known to be 9.9009 Hz and therefore our own fan-paper may be created. Figure 18 below shows this, where green sections result in the frequencies being folded onto the base-band and red sections are frequencies that fold into the base-band with a reverse orientation. The frequencies start from the left at zero and the number in the block represents the right side frequency within its block. This may be extended to the highest frequency desired which in this case is 80 Hz.

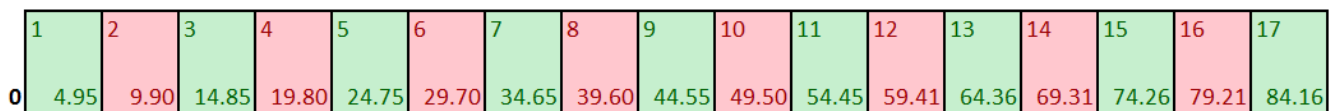


Figure 18 Fan-paper frequencies applied to example

It is required to look for the 10 Hz and 80 Hz frequencies. Fortunately both of these lie in the green section and fall in the base-band in its correct orientation. 10 Hz lies in the 3rd fold and to find its frequency in the base-band, simple arithmetic is applied where the 9.909 Hz is subtracted from the 10 Hz. Therefore the 10 Hz should appear at 0.0991 Hz in the base-band frequency plot. Similarly this done for the 80 Hz where 79.207 is subtracted from it resulting in a base-band representation at 0.793 Hz.

Figure 19 shows the frequency plot of the oversampled signal showing the 10Hz and 80Hz peaks. Below this is the frequency plot of the bas-band frequency of the undersampled signal. In here we find a peak at 0.096 Hz and 0.792 Hz which closely correlate to our calculations of 10 Hz and 80 Hz.

For the examples below, the time signal was created in a way such that it is dependent on the sampling frequency. Both signals were measured over 30 seconds which means a possible frequency resolution of 0.03 Hz can be obtained. Using the *NFFT* function in Matlab, an FFT size is calculated which is dependent on the length of the time vector. By dividing the sampling frequency by the FFT size, a frequency resolution of 0.03 Hz is obtained and this is the resolution of the oversampled frequency plot in Figure 19.

The same approach was utilized for the undersampled case whereby the time signal created is dependent on the sampling frequency. Using the same *NFFT* function and the sampling frequency of 9.909 Hz resulted in a frequency resolution of 0.02 Hz. As mentioned, the

smallest resolution usable is 0.03 Hz. This is where the slight deviations may arise between expected and acquired frequencies.

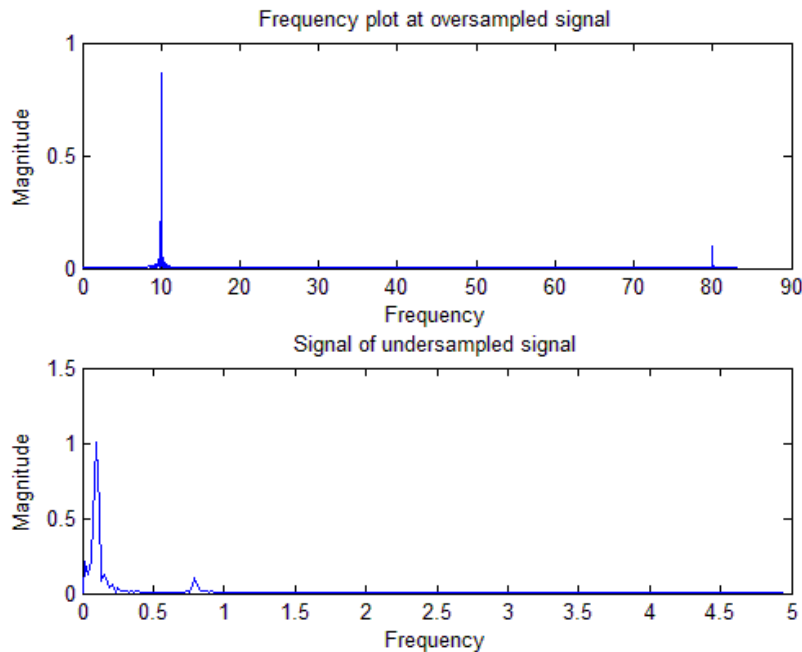


Figure 19 Frequency plot of over and undersampled signals

This example was created to illustrate how undersampling may be utilized. This is an ideal situation where the time signal and frequency signal was dependent on the sampling frequency. In actual experimental setups this is not the case as will be seen during the testing and post-processing sections, and it is important to note how the resolution will be affected.

2.6. Processing techniques

This chapter discussed the various post-processing and measuring techniques needed for this study to be carried out. Below is a summary of the techniques followed through the rest of the dissertation:

- Numerical modelling of rotor setup using FEM models and solving of stiffness and mass matrices in order to carry out modal analysis.
- Time domain data recording of all three methods and conversion into the frequency domain using the FFT algorithm in Matlab
- In the case where high harmonics and orders are present, the implementation of the order removal technique is applied.
- Use of the Wheatstone bridge in order to correctly mount the strain gauge and obtain voltage signals out to represent the correct strain.
- Application of the DIC system using undersampling and fan-paper method in order to correctly understand and read the aliased frequency plot that results.

3. Chapter 3 Finite Element Analysis

3.1. Overview

A finite element model of the shaft is constructed to carry out the numerical analysis. This is done by modelling the rotor in the Patran software and evaluated using the Nastran solver. It is important that the parameters affecting the theoretical analysis using the finite element approach are identified and that the model is built correctly.

A basic rotor model is built and a convergence study conducted during the first analysis. An analysis that looks at the dynamics in terms of natural frequencies and mode shapes is completed. Similar tests are done to a damaged rotor case whereby damage is simulated as a crack in the shaft. A sensitivity study is done on the effect that increasing crack depths will have on the rotor. For verification, these results are compared to a simple analytical model. Based on these results, an actual test setup is designed and manufactured and live experimental tests are carried out.

3.2. Key FEM parameters

The FE method has been around for a considerable time and has proven to be an accurate, time effective and cost effective means of numerical analysis as well as for verification of experimental testing. It is capable of solving large, complex problems that have general geometric, loading and boundary condition configurations and has increasingly become the primary tool for analysis (ESTEQ, 2006). However it is just as easy to put it into incorrect use and obtain strange results without realising. Therefore great care must be taken when carrying out a finite element analysis, from the modelling stage through the development of the model right up to the analysis, since a small change in one of the parameters may have a large effect on the results. The main parameters are the geometry, mesh used, boundary conditions, applied loads and material properties. These are briefly discussed below.

3.2.1. Geometry

It is important that the geometry is modelled as close as possible to the one that will be manufactured. This is to ensure that the correct dynamics are captured and that the system is understood properly. Once experimental results are obtained, the FE model's geometry may be fine-tuned in order to match the experimental results closer. This process is known as model updating.

3.2.2. Mesh

There are various types of elements that may be used for meshing an object. They all have their own advantages for different geometric configurations. The three main types are 1D beam, 2D shell and 3D solid elements. This study involves a solid rotor and therefore solid elements used. The following should be considered, when modelling with solid elements (L&K GmbH., 2011).

- Solid structures usually lead to large meshes when modelled with solid elements and therefore need large computational time and working space. In regions of large stress gradients the mesh density must be large. Therefore for these structures and objects where depth of the model is not too large, one should use shell or beam elements whenever possible.
- Mirror symmetries of the model (half or quarter model) or rotational symmetry, where axial symmetric elements reduce the spatial dimension from 3D to 2D should be utilized.
- Hexahedron elements are more reliable than tetrahedron elements, but the mesh generation may be more complicated or even impossible.
- Tetrahedron elements allow more complex meshes but the results should be inspected more closely.
- Quadratic elements produce better results, but require more computing time.
- The results of solid elements are reliable only if the following is considered:
 - the aspect ratio of elements should be near to one (not less than 1:2 to 1.3)
 - warping, should be not too large; the corner nodes should lie as near as possible on a brick

3.2.3. Boundary conditions

Of all the parameters, this is one of the most important. This refers to the manner in which the component is constrained and the number of degrees of freedom in which it is constrained. A minute error in this section may result in completely different results which is undesirable. Therefore, for the setup to be analysed, one needs to understand:

- What supports the structure
- How is it supported
- In what direction is it supported
- Know the degrees of freedom in which it is not supported

3.2.4. Loads

If an external load is applied to the structure, understanding the magnitude, direction and time dependency of the load is critical. In many instances it is this load that results in some sort of movement or internal stresses of the object that occur. And it is these results we look for and why the analysis is initially done. Therefore modelling the correct type of load is essential.

3.2.5. Material properties

The material properties consist of the density, elastic modulus, Poisson's ratio and shear modulus. In some cases temperature and electric resistivity or conductivity need to be known. For simple isotropic materials values of the material are easily available. However when moving to composites, it can get complex with a system of material properties representing a material in specific directions. Therefore it is essential to know roughly what

type of materials one is working with. This is also a parameter that is often involved in model updating.

3.3. Rotor model design and analysis

3.3.1. Model setup

Before the model is built, it must be ensured that the model is at a manageable size and practical, keeping in mind that it will eventually be manufactured for the experimental testing.

The basic design opted for this setup comprised of two masses mounted onto a shaft. Most industrial rotor shafts contain a variety of mountings on them. These range from a series of turbine blades to a coil arrangement setup as found in generators. It was decided to represent these mountings and mass inertias in a simple way and therefore two disks were utilised. In order to prevent any complex modelling, the disk and shaft were to be treated as one component.

The rotor is to be powered by a motor on the one side and coupled to the shaft through use of rigid couplings. The other end of the shaft is overhanging and free. The setup is to be tested under normal constant speed rotation and therefore no additional component was added on this free-end. This approach also allows for the option of mounting a load to brake the system if necessary and makes the setup more flexible. Details of this were not known at the time and therefore the rotor had a free end for the initial analysis. From here on, the side where the motor is coupled is referred to the motor-end and the overhanging side is referred to as the free-end.

The rotor was to be mounted on two bearings on either side of the disks. Self-aligning cylindrical roller bearings were to be used. This allowed for any misalignment problems that might occur and prevent any drastic stresses in the shaft. Details of this setup may be seen in Figure 20 below together with a coordinate system that will be used. It must be noted that this is a 2D image and the x-coordinate axis comes out of the page.

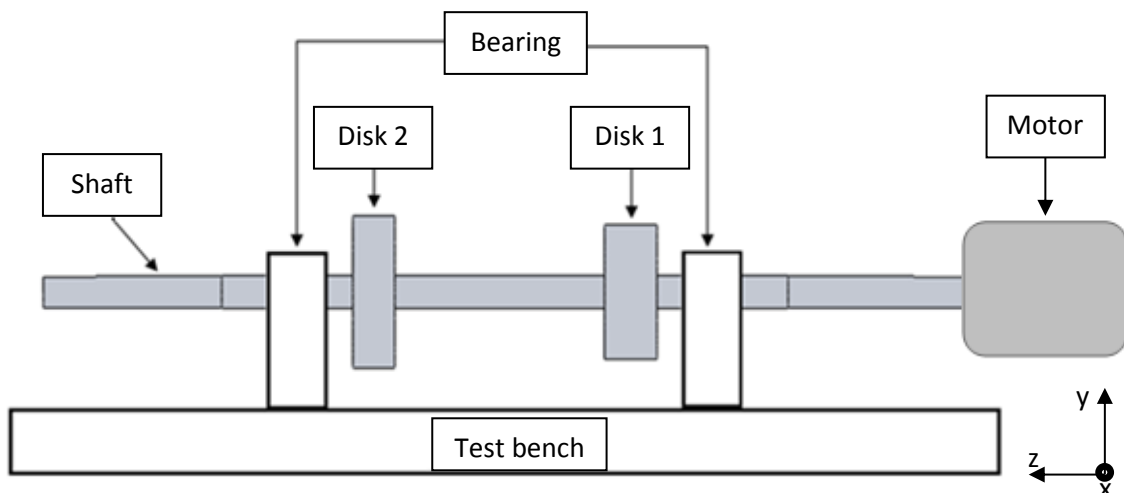


Figure 20 Schematic diagram of test model

The initial dimensions associated with the above diagram may be seen in Table 1. These were governed by some manufacturing constraints. It was initially decided that damage was to be introduced by using a spark eroding process and in order to do this the disk's locations and overall shaft length needed to be adjusted to the below dimensions for this to occur. The disk sizes were also restricted, as too big would result in them touching the test bench.

Table 1 Dimensions of setup

Description	Diameter (mm)	Width (mm)
Disk 1	144	50
Disk 2	127	40
Shaft	30	880
Centre distance Disk 1 – Disk 2	-	200
Distance bearing to Disks	-	20

3.3.2. Mesh type selection

As mentioned before there are various elements that can be used. For this setup which is a solid rotor, 3D solid elements will be used. The elements available using Patran are Tet4, tet10, Tet16, Hex8 and Hex20. These have their individual advantages, disadvantages, complexity, simplicity and accuracy when applied to geometry. This section discusses these traits and the most suitable option is chosen.

a) Tet4

The Tet4 element is a three dimensional triangular pyramid like element containing a node at each of its corners. It is derived from the 2D linear triangle element which is also known as the constant-strain triangle (CST). It is a linear triangle since the field quantities vary linearly in its Cartesian coordinates.

This element was mainly created for theoretical purposes and is not suited for actual analysis. Specifically in bending, meshes containing these types of elements are undesirably stiff. One may refine the mesh, however convergence occurs extremely slowly. In certain cases of strain conditions, the mesh tends to “lock” whereby it cannot deform at all (Cook R.D. et al, 2002).

b) Tet10 and Tet16

Unlike the 3-noded triangle element above, the Tet10 is derived from the 6-noded triangle element with an extra node between each of the three corner nodes. Due to the extra nodes, the displacement field for the element is quadratic and is also known as the quadratic triangle. It has also been shown that these elements can model bending more accurately and does not suffer from “locking”. It is also shown that convergence occurs at a much faster rate than the Tet4 which makes it a more ideal candidate.

The Tet16 is similar to the tet10 except that it contains two nodes between the corner nodes. It is a much higher order triangle and similar to the Tet10 in that it does not suffer from “locking” and has good convergence rates (Cook R.D. et al, 2002).

c) Hex8 and Hex20

These elements are 8 noded and 20 noded cubes. In order to critically evaluate these elements, they need to be looked at in the 2D quad4 and quad8 elements shown in Figure 21. The reason for this is that since the rotor geometry is not a simple geometry, it cannot be modelled directly by 3D solid cubed elements. Therefore 2D quad elements are used on the face of the shaft and then extruded into a three dimensional cube.

The quad4 is a simple 4-noded plane element. Like the CST, the quad4 cannot exhibit pure bending. Although it does not “lock” like the CST, when it is bent it displays the expected bending strain but also a parasitic shear strain which absorbs strain energy. Thus in order to comply with a prescribed bending deformation, a larger bending moment than the correct value is required. Figure 22 shows its defects under bending. Due to the similar properties as the Tet4 element, the extruded Quad4 or Hex8 element is not ideal for meshing the geometry.

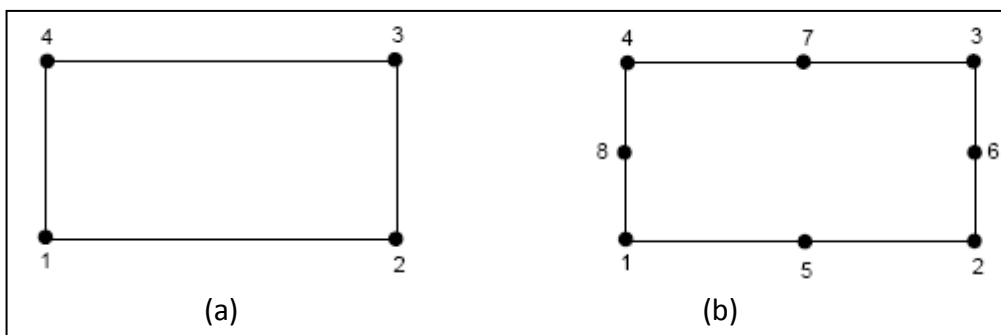


Figure 21 a) 4 noded Quad4 element, b) 8 noded Quad8 element (Patran Library)

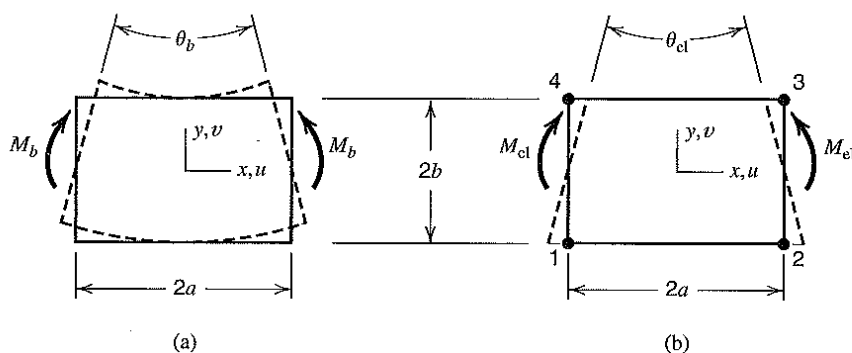


Figure 22 Bending defects present in quad4 element a) Deformation made in pure bending b) Quad4 element under pure bending (Cook R.D et al, 2002)

The quad8 element is like the quad4 with added side nodes, much like how the side nodes were added to the Tet4 to obtain Tet10 and Tet16. The Quad8 does not display any of the defects present in the quad4 like the parasitic shear. The extruded quad8 element is known

as “brick” elements. By extruding the quad8 2D element, the Hex20 “brick” element shown in Figure 23 is obtained.

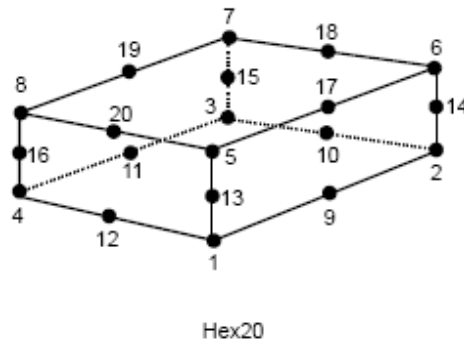


Figure 23 Hex20 or “brick” element (Patran Library)

Based on the properties of the elements studied above, the Tet10, Tet16 and Quad8 to Hex20 elements are the most favourable. Since the Tet elements may directly be modelled into a 3D geometry, it is a slight advantage but research has shown that although this is the case, much more nodes are required to obtain the same result which increases computational time. This is seen in a simple bending problem of a cantilever beam. This example displays the CST, Quad4, LST and Quad8 elements. The results showed that the LST and Quad8 are most accurate, however the LST requires more than twice the number of nodes (Cook et al., 2002).

The other advantage of using Hex20 elements is that there is more control of how the geometry is meshed. Cao et al. (1998) also recommends using this type of element for modelling cracks as damage since it allows easier meshing on crack faces which is advantageous for this study. Future tests and analysis in this study will use the Hex20 “brick” element.

3.3.3. Meshing and convergence study

In order to mesh on the 2D cross sectional surface of the rotor, it was divided into four quarters. A mesh seed was created to control the number of elements on the surface. This was then extruded to a specified number of elements along the longitudinal directions. Figure 24 below shows the mesh seed on the perimeter of each quarter with the surface elements aligning to those nodes.

A number of these tests were done with various different numbers of surface and extruded elements used. This was done as a convergence study to define how many elements would be required to accurately mesh the model. Table 2 shows a summary of the number of elements used as well as the first torsional mode obtained. Figure 25 shows the natural frequency converging to 133.02Hz and Figure 26 shows that the error decreases and approaches 0% error.

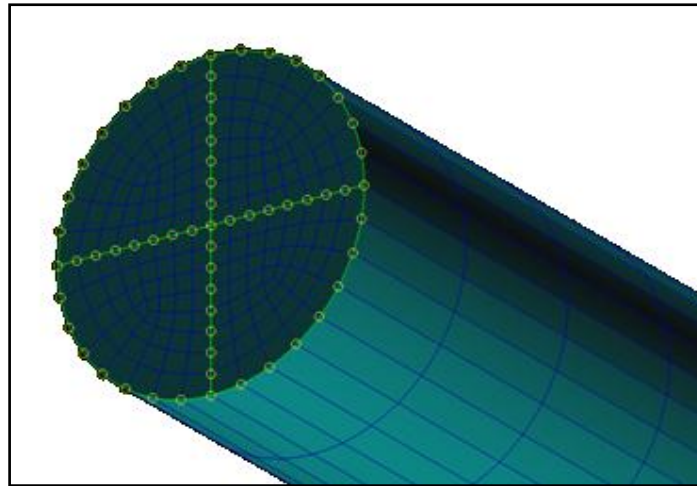


Figure 24 Surface mesh created using mesh seeds and then extruding the elements

Table 2 Convergence study

Convergence study								
Iteration	1	2	3	4	5	6	7	8
nodes	821	2095	6295	11101	16 195	31014	41769	54929
elements	67	211	820	1668	2679	5259	7631	10447
Frequency	121.52	129.8	132.67	132.56	132.82	132.89	132.97	133.02
% error	6.38	2.16	0.08	0.20	0.05	0.06	0.04	0.00

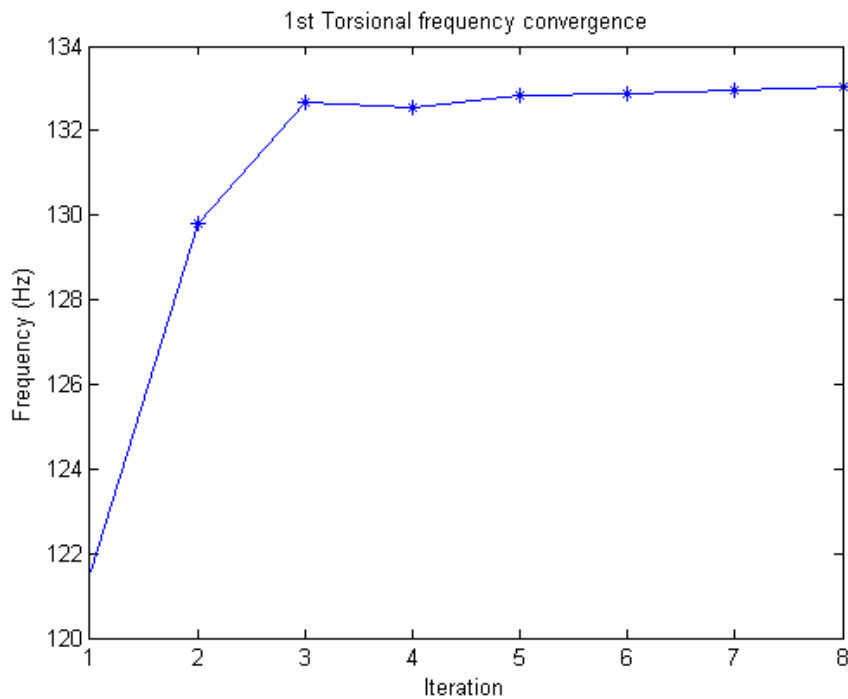


Figure 25 Frequency convergence

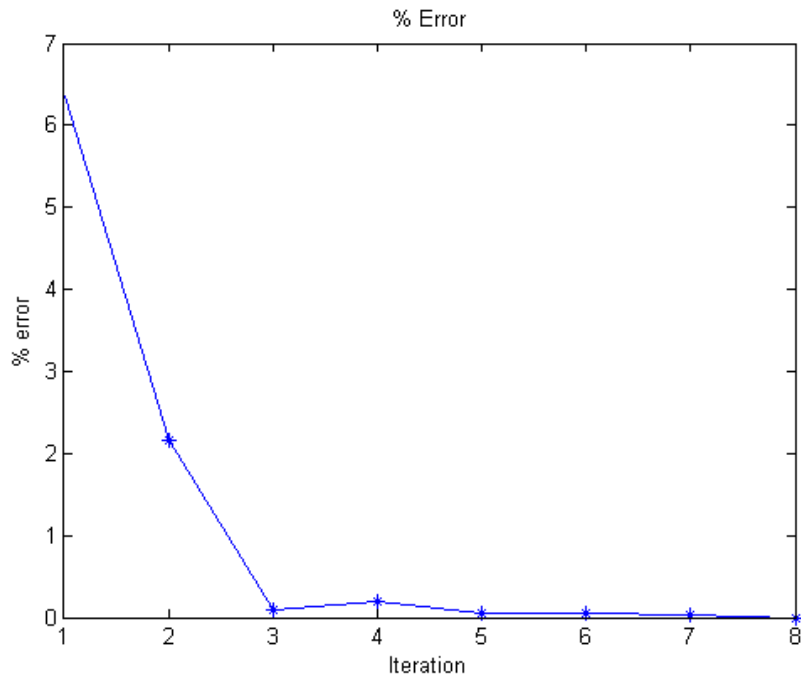


Figure 26 Percentage error convergence

3.3.4. Boundary condition modelling

The boundary conditions should be applied to closely resemble what the actual case might look like. As mentioned before, this forms a very critical part of the analysis. It is important to know exactly how and where the rotor is restricted. As mentioned, the rotor is coupled at the one end to a motor and free at the other end. It is simply supported next to the disks using self-aligning cylindrical bearings. The following points define the boundary conditions.

The motor-end shaft is coupled to another shaft that goes into the motor to an armature. This armature has quite a large mass. In some instance it is sufficient to simply treat it as a fixed joint by restricting the boundary condition in all directions at this point. This method was used for representing the BC in the convergence study. Lissendien et al. (2007) also used the same approach for the motor, as was shown in the literature study chapter. Their research showed good results using this method and therefore for further analysis this method was utilised as it is a simple approach without any complex modelling and would sufficiently allow finding where the natural frequency and other parameter sensitivities are.

Due to the rigid coupling used, self-aligning bearings were chosen to allow some correction for the shaft for any irregularities that may have developed in the shaft. Therefore at the bearing location the rotor is only fixed in the translation directions x and z , but may rotate about any of the three axis. The reason for not constraining the y direction is that the bearing is not located on any shoulder on the shaft and there is no axial restraint. The only way that the shaft is prevented from freely moving in the axial direction is its connection to the motor. Figure 27 shows how this boundary condition was applied.

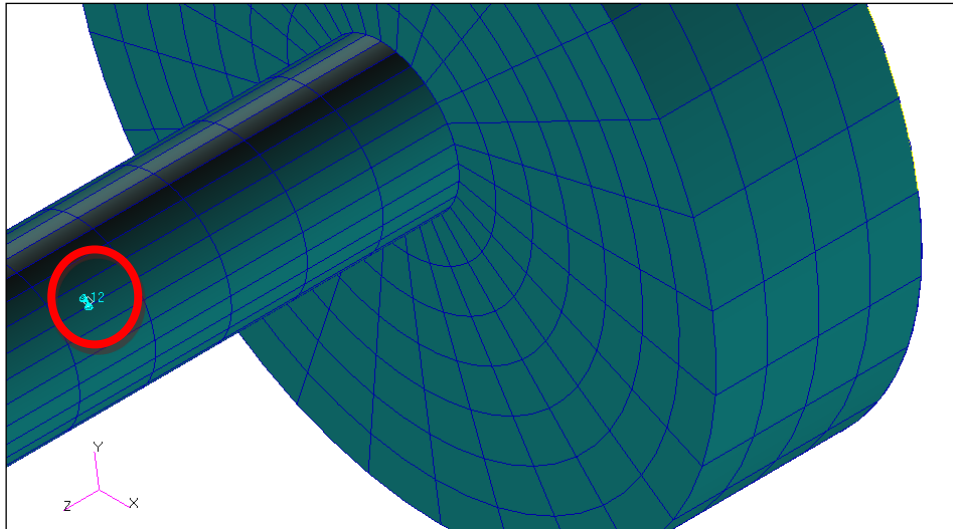


Figure 27 Bearing boundary condition 1 and 2 representing x and y coordinates encircled

3.3.5. Material selection

The rotor may be constructed with a variety of materials. Rotor shafts are commonly made from steel containing a combination of Nickel, Chromium, Molybdenum, Vanadium, Tungsten, Nitrogen and Niobium. Depending on the appropriate operating temperatures, the shafts can be fabricated out of low/high alloy heat resistance material or of low alloyed, highly toughened material for low pressure application (Janssen et al., n.d). From this it would make sense to use steel as the basic material. Obtaining something with the above elements would result in a more costly design. It was therefore decided to use normal mild steel. It is easy to manufacture and work with, has a better strength-to-weight ratio than something like Aluminium and available at low cost. Table 3 specifies the properties used for the preliminary analysis:

Table 3 Material properties (Callister W.D., 2003)

Properties	Value
Density	7800kg/m ³
Elastic modulus	207x10 ⁹ GPa
Poisson's ratio	0.3
Shear modulus	80x10 ⁹ GPa

3.3.6. Analysis and results

Once all the above settings and properties were applied to the model, a proper modal analysis could be done. This model in its final state may be seen in Figure 28. Once the analysis was done it revealed a torsional frequency of 133.02 Hz for the first torsional mode. The mode shape associated with this frequency is shown in Figure 29. The second torsional frequency obtain was 409 Hz and its mode shape may be seen in Figure 30. It is seen in the first mode shape that the response increases as it moves from the motor end to the free end. The second mode shape shows a higher response near the smaller disk and decreasing on either side of it.

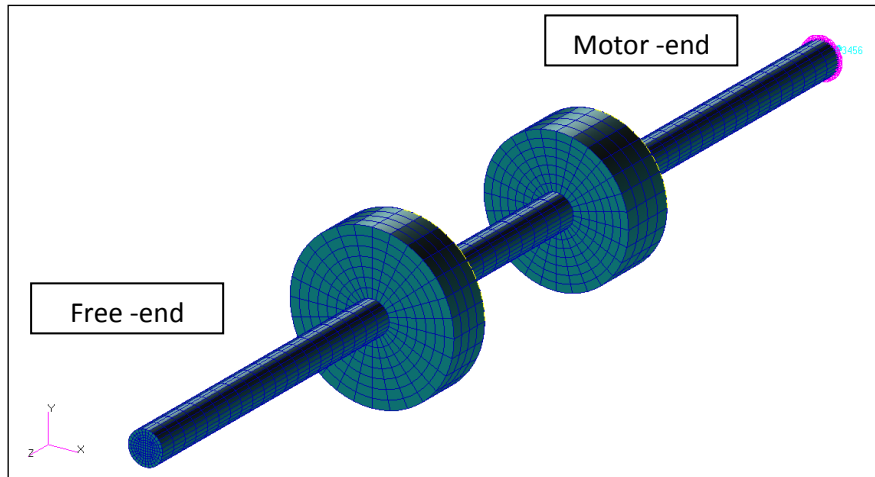


Figure 28 Final FEM model for analysis

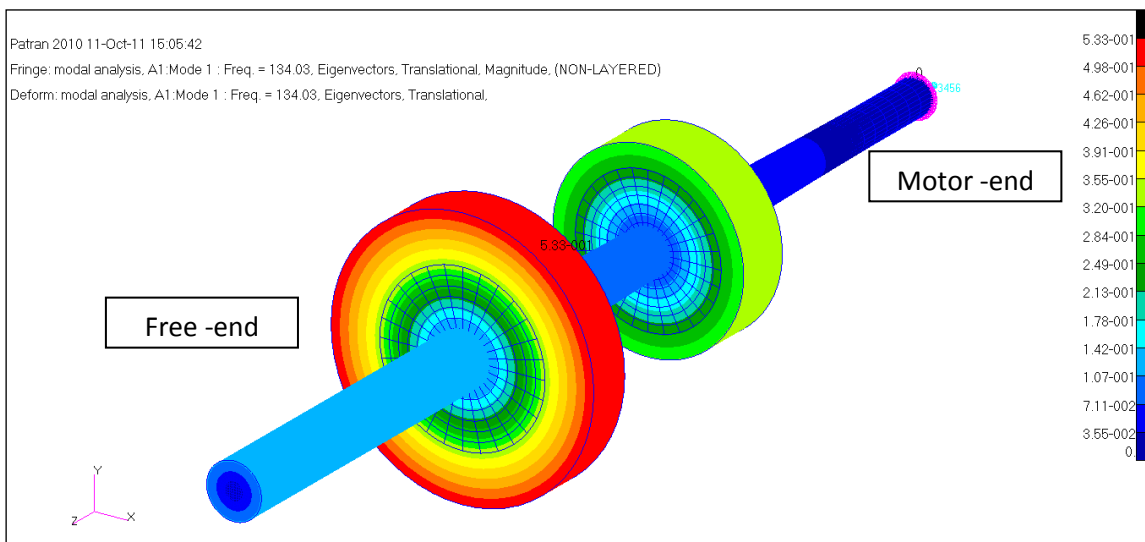


Figure 29 1st Torsional mode shape

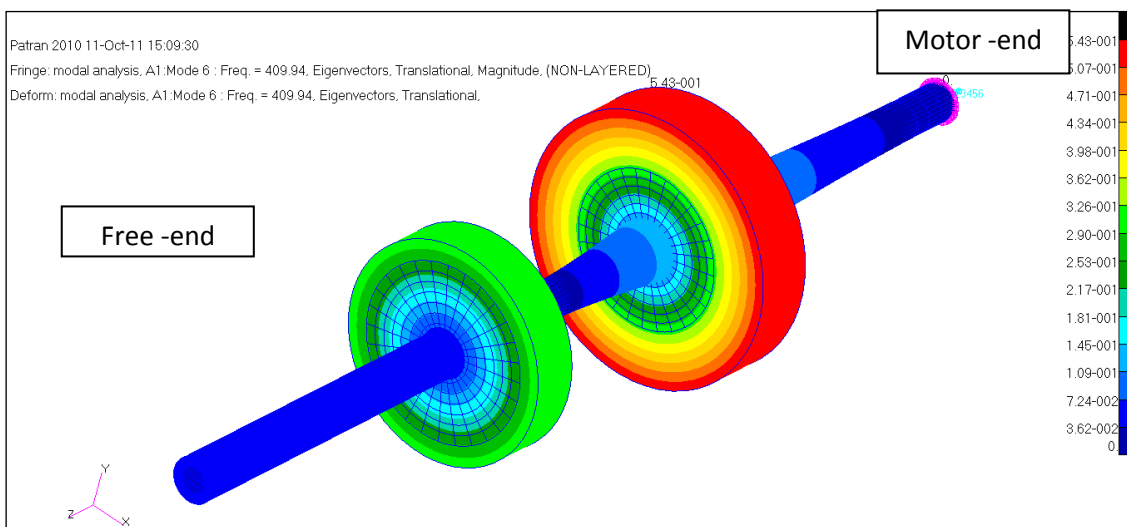


Figure 30 2nd Torsional mode shape

For interest and model verification, the results were then compared to the results obtained from a simple analytical lumped spring-mass system using the equation of motion for the torsional DOF. The schematic sketch shown in the Figure 31 below shows the lumped masses representing the disks and the shaft sections as the torsional springs. The free-end of the shaft may be ignored, and the system is treated as a two degree of system setup.

$$[J]\{\ddot{\theta}\} + [K]\{\theta\} = \{T\} \quad (\text{Eq-12})$$

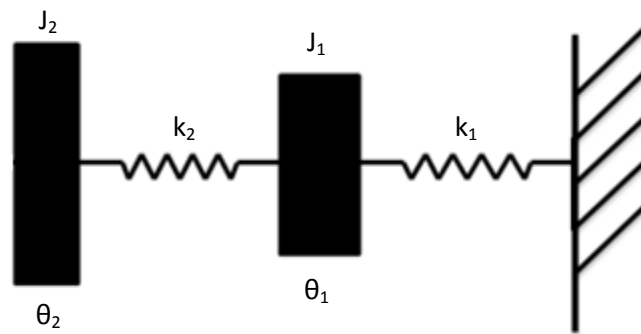


Figure 31 Schematic diagram of lumped spring mass system

The details of the lumped spring mass system may be viewed in Appendix B. Table 4 revealed the results from the simple analytical model in comparison with the FEM. As seen there is a close correlation between the two with just over 2% difference. This is quite a small error and a good basis that the FEM model is sufficiently modelled for further analysis to be carried out.

Table 4 Comparison of FEM and Analytical results

Torsional mode	Lumped	Patran	% Difference
1	136.04	133.01	2.27
2	420.17	408.95	2.74

3.3.7. Damage modelling

Analysis for the undamaged case is completed, and the analysis moves to a damaged case. Figure 32 below shows a transverse crack that was inserted into the centre of the shaft.

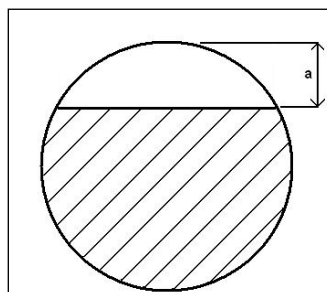


Figure 32 Cross section of the transverse crack inserted into the shaft of depth a

The method of modelling the crack into the mesh must be decided. When dealing with cracks in shafts in general, the system becomes nonlinear. This is the case in lateral vibration where a crack introduces a breathing mechanism whereby crack faces are in contact and

then not in contact during each rotation. This results in a variation in the stiffness as it rotates 360°. This means that the same natural frequency will have two different mode shapes depending on where in the shaft the crack is.

In the case of torsional vibration which is the current study, the breathing mechanism does not play a major role. Therefore, when modelling the damage it was decided as a start to assume that no contact between crack faces is present. This is not an incorrect assumption since in the experimental stage; damage was introduced by sawing the shaft. This left the two crack faces open and not touching. It was also found in Lissenden et al. (2007) that this approach was used with good comparison between the FEM and experimental results.

The damage was introduced at the centre of the shaft, in between the two disks. Once the shaft was modelled and meshed, the crack was introduced by simply not connecting the nodes at the specific location. The term used in Patran is where to “equivalence” the nodes. The figure below shows this process. Figure 33 (a) shows the centre shaft section with the selected nodes to be excluded from being equivalenced. Figure 33 (b) shows the process after this step and it is seen that all other nodes have a pink circle around them showing the nodes have joined but the cracked section does not, meaning the element nodes at those locations are separate.

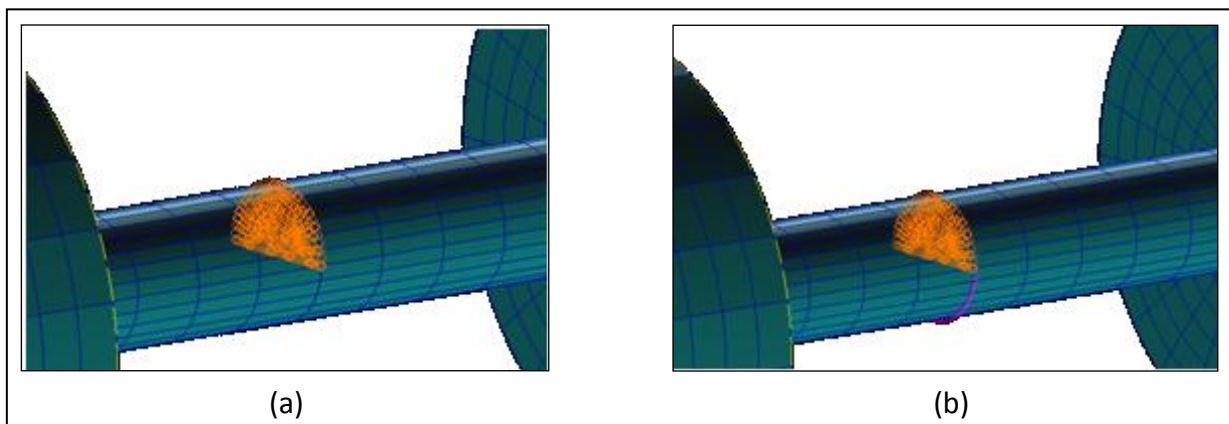


Figure 33 a) Selected nodes that are not equivalenced in order to represent a crack, b) Pink circles shows the nodes that were equivalenced

Various crack depths a as is in Figure 32 were modelled in the shaft and Table 5 below summarises the crack depths and well the 1st torsional frequencies obtained. Figure 34 shows how the natural frequency decreases with increasing crack size as is expected.

Table 5 Results of damaged rotor

Crack depth (a)	0.00	1.49	3.27	5.65	8.49	11.70	15.00	18.30	21.40	24.40	26.70	28.70
% Crack depth (a/D)	0.00	4.97	10.90	18.83	28.30	39.00	50.00	61.00	71.33	81.33	89.00	95.67
Mode 1	133.02	133.02	133.00	132.94	132.80	132.52	131.98	131.08	129.26	125.32	117.80	91.84
Mode 1 ratio	1.00	1.00	1.00	1.00	1.00	1.00	0.99	0.99	0.97	0.94	0.89	0.69
Mode 2	408.99	408.97	408.78	408.15	406.78	403.94	398.76	390.62	376.11	352.06	316.79	263.91
Mode 2 ratio	1.00	1.00	1.00	1.00	0.99	0.99	0.97	0.96	0.92	0.86	0.77	0.65

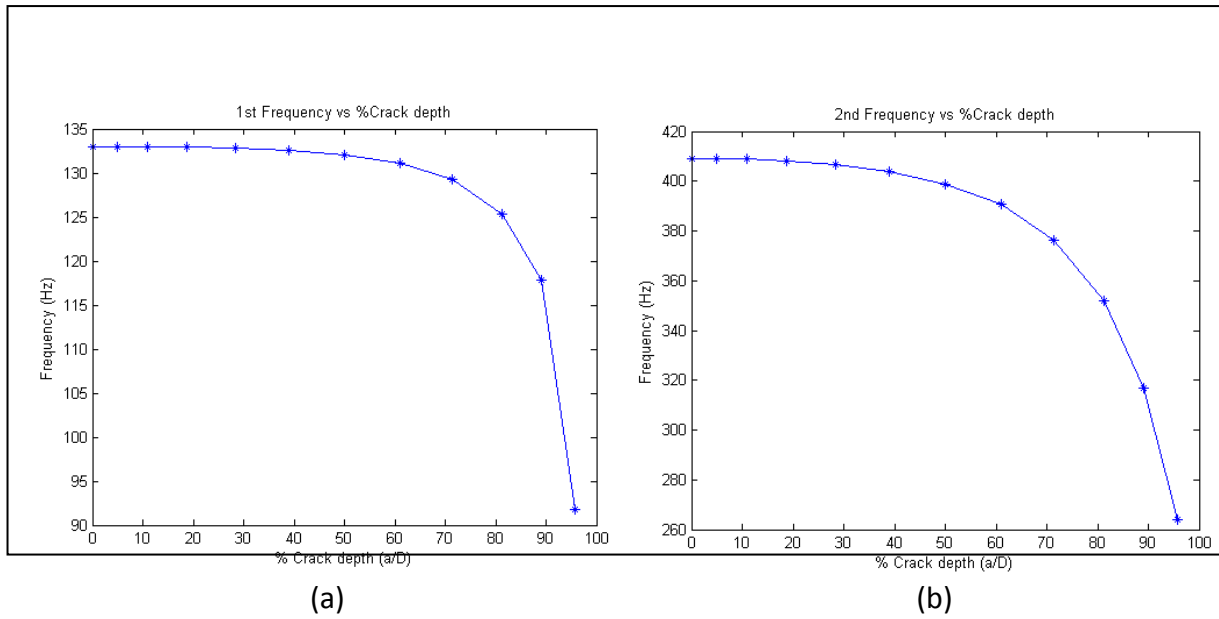


Figure 34 Change in torsional frequency with crack depth a) 1st mode b) 2nd mode

Dimarogonas et al. (1981), who did experimental studies on torsional frequencies in shafts with transverse cracks, developed a general graph relating the 1st torsional frequency ratio to the depth of the crack ratio. In recent studies, Lebold et al. (2003) did similar studies on steel shafts. The torsional frequency ratios obtained in this FEM analysis was compared to those from his work and is seen in Figure 35 below. There is good correlation between the two specifically for the first mode which is what he had studied. This verifies the method of damage implementation in the FEM model in this study. Obviously approaching it as a nonlinear problem and solving it using contact bodies and nonlinear software may result in more accurate result, but this method shows good correlation with existing methods.

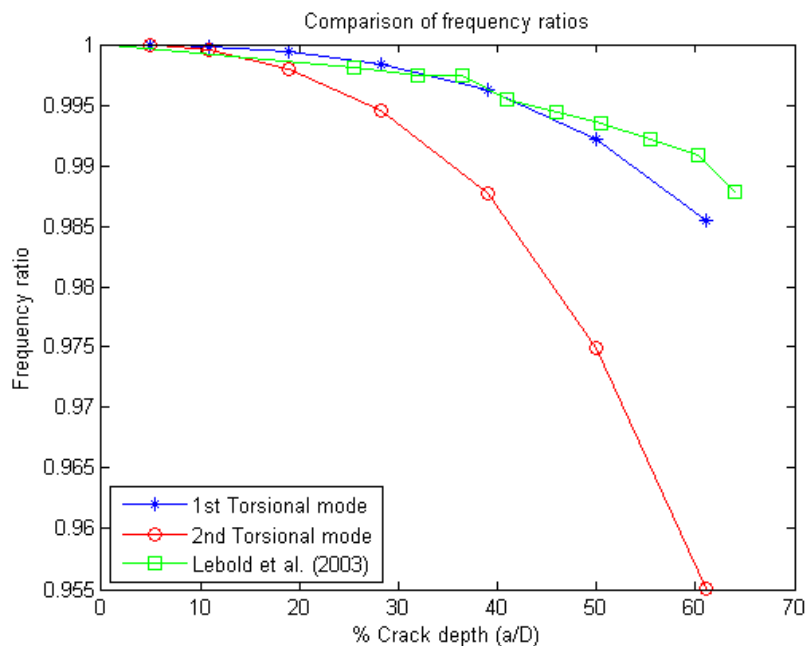


Figure 35 Comparison of Frequency ratio between FEM data and Lebold et al. (2003) experimental study

3.4. Equipment location analysis

The above analysis showed a frequency drop with an increase in crack depth. These are of measurable magnitude but it is essential to know where to mount the measuring equipment on the shaft to ensure optimum capture of responses. This means investigating the model and understanding which sections has higher displacement and strain response in order to make an informed decision about the location of the fibre-optic sensor and the telemetry strain gauge system.

When dealing with vibration monitoring, it is vital to understand the mode shapes of the object or system under investigation. This simple shape is what will guide the location of measuring equipment. This shape defines the magnitude of vibration of each area within the object/system. Thus, higher DOF system means a more accurate shape. Areas where zero magnitude vibration occurs are known as nodes. Each mode shape will have its own mode shape containing its own high magnitude and node areas. It is highly possible that transducers are mounted at these node locations and end up having no data or low magnitude data captured. This is not ideal and care must be taken when choosing a location.

The first mode shape provides useful guidance for selecting equipment locations in this study. Figure 29 in section 3.3.4 shows this mode shape. It is repeated again in Figure 36 below for convenience. From this figure it is clearly seen that the rotor increases in torsional angle-of-twist, starting from zero at the motor-end to a maximum at the free-end. The disks obviously show a higher response but it must be remembered that this is at a larger radius. In order to get a proper representation of the shape, only the shaft response is looked at, and from this it is seen that the highest response is at the free-end and the shape is just a simple twist of the shaft.

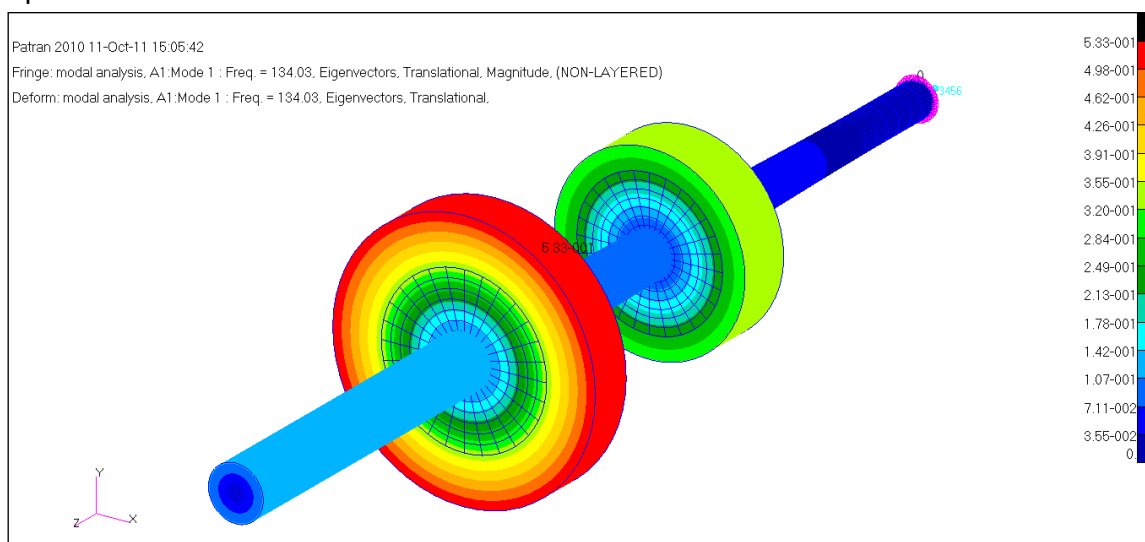


Figure 36 1st torsional mode shape for magnitude response analysis

This twist at the free-end represents rotational or angular displacement. It is precisely this parameter that the fibre-optic sensor measures. It measures the minute changes in the

rotational deviations which represent torsional vibration and measures it in a square wave voltage form. Based on this, the ideal location of this device is at the free-end.

A simple response analysis was done on the system. From this the elemental strain at the free-end and motor-end could be compared. Figure 37 shows the comparison of the responses and it is clear that the strain response is more sensitive at the motor-end, as expected.

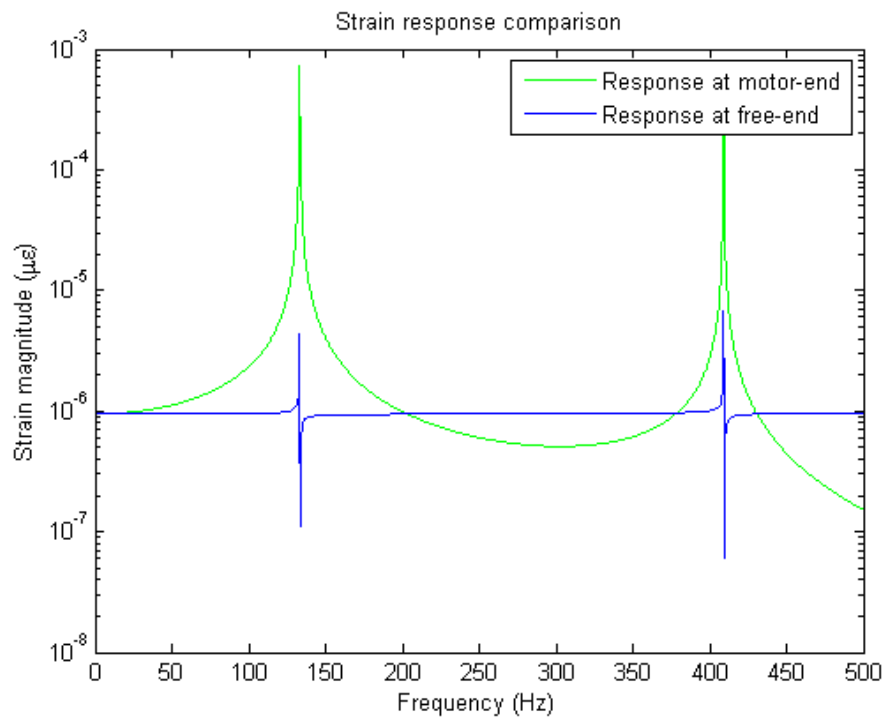


Figure 37 Comparison of strain response at motor and free-end

The location around the circumference of the shaft is also studied. Ideally, with damage introduced, the strain should change depending on the depth of the damage. The damage is introduced at the centre of the shaft and the gauges are mounted at the motor-end. St Venant's principle states that the strains that result from application, to a small part of a body's surface, of a system of forces that are statically equivalent to zero force and zero torque become negligible at distances which are large compared with the dimensions of the part.

In this case the strain gauge is mounted at a distance from the damage, so isolated strains that occur near the damage would not make a difference for the gauge mounted at a distance. It must be noted that the actual strain values as a result of damage is not the main interest, the frequency content within it is important. If for instance the gauge were to be mounted at the location of damage, then the position around the circumference would matter.

3.5. Conclusion

A FEM analysis was done and revealed important information about the dynamics of the system as well as the sensitivities associated with some of the measurable parameters that will be used during testing. The following can be drawn from the analysis done in this chapter and based on this the shaft may be manufactured and experimental testing can be carried out as explained in the next chapters:

- 1st and second 2nd torsional modes are expected to be seen at 133.02 Hz and 409 Hz.
- A damage of 61% crack depth would yield a 2 Hz and 18 Hz frequency drop in the 1st and 2nd torsional modes respectively
- These are measurable frequency changes and are expected to be seen during experimental testing
- Fibre-optic sensor response is expected to be higher at the free-end of the rotor
- Strain response is higher at the motor-end and the strain gauges should be mounted there
- Strain response is independent of the location around the circumference with damage present

4. Chapter 4- Experimental setup and Test procedure

4.1. Overview

This chapter briefly discusses the manufacturing of the rotor as well as all the components associated with the setup. There is a discussion of the torsional measurement techniques and equipment used for the measurement process. A discussion of what will be measured and in what fashion is given. The chapter then concludes with a set of results that are expected.

Figure 38 below shows the final setup used with all the components labelled. Some of the components were specially manufactured while others were taken from existing setups. This is further discussed in the sections to follow.

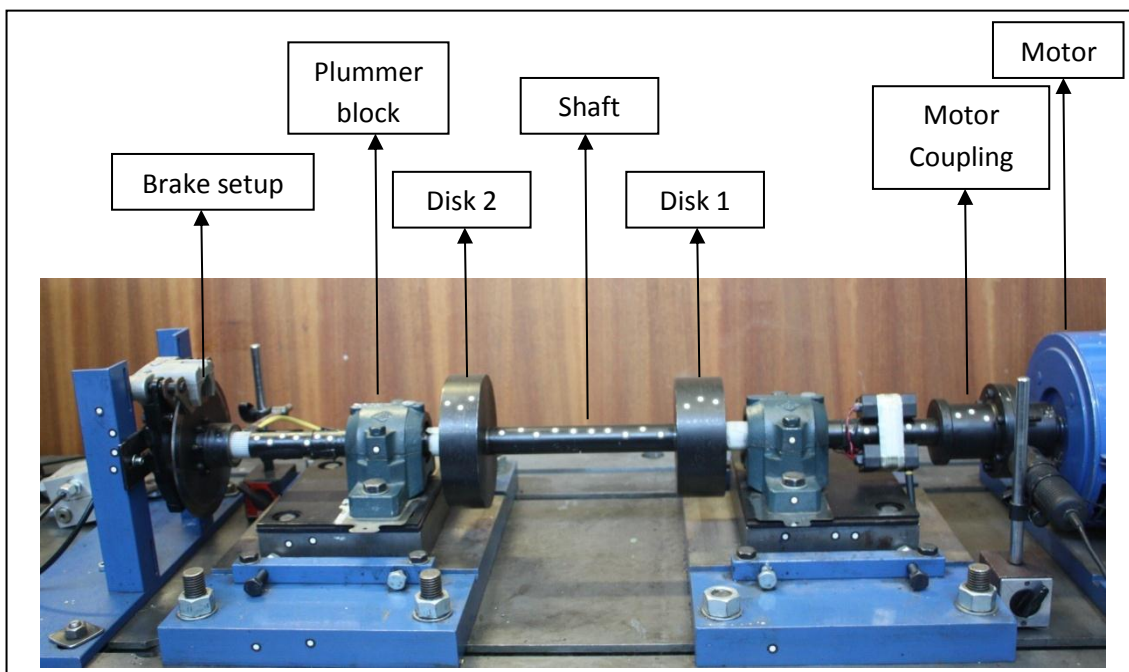


Figure 38 Rotor setup in bearings coupled to the motor on the right

4.2. Manufacturing

The manufacturing of the rotor was done at CSM Engineering. The dimensions used were the same as those used for the theoretical analysis. It contained three separate components put together. These were the two disks and the shaft. The outer diameters of the disks were machined to size as well as their widths using a lathe. The holes in the centre of the disks were bored out. They were then shrunk fitted onto the 30 mm shaft in their appropriate locations. This was done by heating the disks in order for the holes to expand and then moved to the location where it shrunk to form a tight fit. Two sets of keyways were cut into the shaft ends for coupling purposes. All components used were mild steel. The exact dimensions used may be viewed from a SolidWorks drawing found in Appendix A. The final rotor may be viewed in Figure 39 below.



Figure 39 Manufactured rotor used for testing

The manner in which the rotor was attached to the motor was through the use of a rigid coupling. The couplings were manufactured at the same company as the rotor. The main aim with the design of the coupling was for it to act like two flanges being bolted together without any flexible material that are commonly found in some couplings in order to assist in alignment problems. As mentioned before, damping in the torsional direction is much more than in the lateral direction. It is important to ensure that as little damping as possible is introduced into the system in order to obtain better results. For this reason rigid couplings were used without any rubber flexibilities. The coupling may be seen in the Figure 40 below.

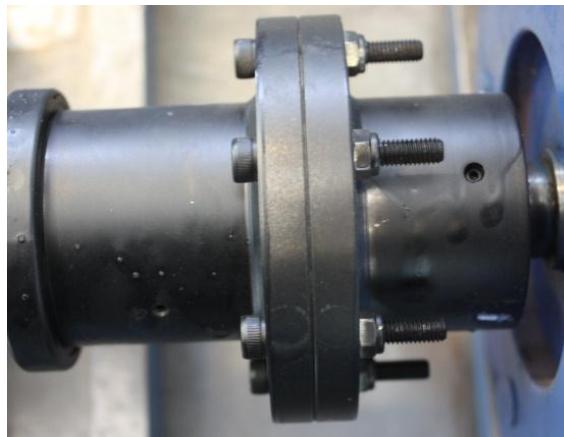


Figure 40 Rigid flange coupling used

At the other end of the shaft, another coupling was manufactured for the mounting of a brake disk that was to be used for strain tests during calibration of the torsional strain gauges. This coupling is similar to the one used at the motor end. The brake disk was then bolted to the flange section of the coupling. The brake setup was not manufactured, but was obtained from the universities' mini baja cars. It is a standard disk calliper brake system controlled using hydraulics.

Other components manufactured for the setup were spacers which were used for height adjustment of the rotor in order to align with the motor. For finer adjustments, standard spacers were used.

4.3. Setup

The rotor was coupled to a 3kW Brook Crompton MD112BS 3 phase 50Hz variable speed DC motor using the rigid couplings. The motor was controlled through a control box seen in Figure 41 whereby the speed could be varied from 0 up to 3000RPM.

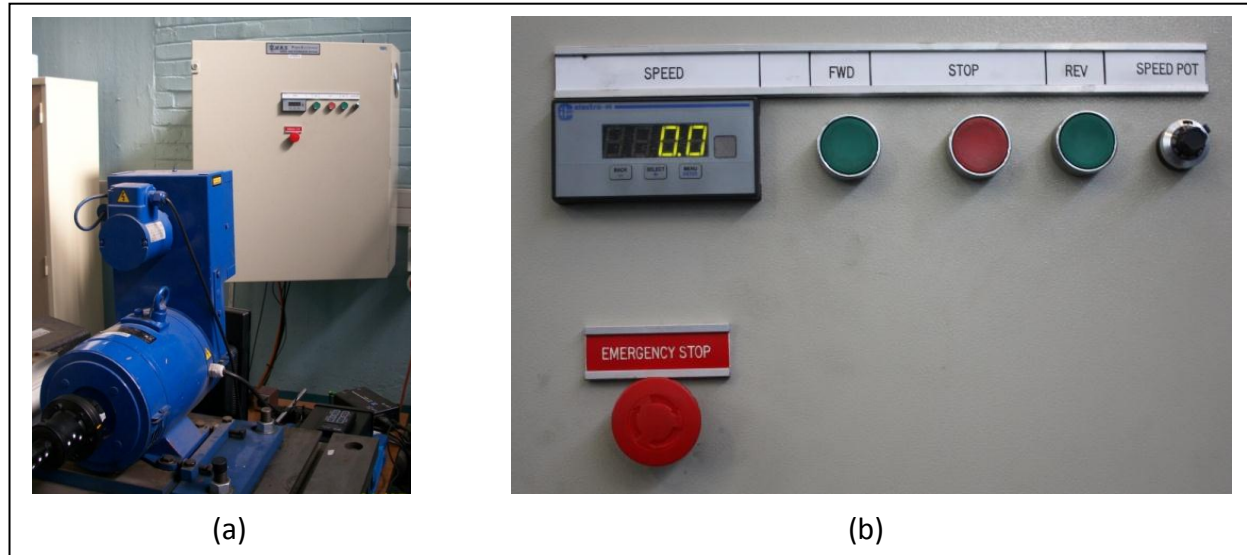


Figure 41 a) 3kW DC motor with controller box, b) Controller box controls

The setup was mounted on two self-aligning spherical roller bearings 22206 CCK with internal diameter of 30mm and housed in a felt sealed SNH 507 TC plummer block. These were chosen specifically because a rigid coupling was used. These bearings would allow for correction to be made should the rotor not be perfectly aligned when mounted. In order to reduce any high stresses as a result of the rigidity, the rotor was placed into the bearing and the housing was left to be loose. The coupling to the motor was then bolted and fixed tightly. The rotor was turned slowly which allowed the rest of the shaft to align into its own least stressful position. The holes for where the bearing housing was fixed were slots which allowed for this positioning. This method allowed for the horizontal direction alignment problem to be solved. For the vertical direction, spacers were used. These spacers were placed under the bearings as needed in order to align the rotor as accurately as possible. Once it was seen that the housings were firmly stable on the bench, the rotor was turned slowly again to ensure that no movement of the bearings were present and eventually tightened into position.

The brake disk and calliper setup involved mounting the disk onto the shaft as mentioned earlier. The callipers were mounted on fixed support frames and placed into its correct position over the disk. The entire setup with all the components and mountings may be viewed in the figures below.



Figure 43 Bearing and spacer setup

Brake calliper setup

Brake disk

Bearing housing

Alignment spacers

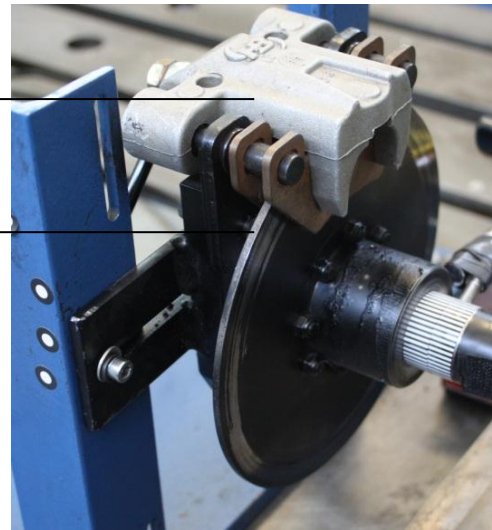


Figure 42 Brake setup on rotor

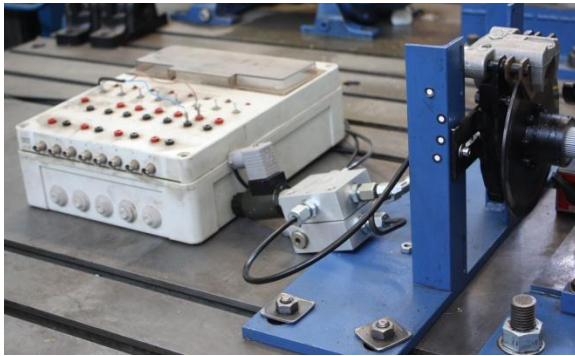


Figure 45 Complete brake setup with control switch on left and control valve in middle



Figure 44 Pump for hydraulic brake

4.4. Fibre-optical sensor setup

The fibre-optical sensor used for the experiment is an Optel-Thevon fibre-optical fibre probe capable of measuring 500,000 impulses per second powered by a 12V DC power supply. The fibre-optical sensor consists of two main parts that are directly linked to the setup, which are the black and white coded tape and the fibre-optical sensor. The tape is mounted directly onto the shaft and is pasted around the circumference. The fibre-optical sensor which is the receiver is located a small distance away from the tape. This fibre-optical sensor sends the reflected light signal back to the analyser whereby in the time domain it is viewed as a square wave. The square wave in this setup ranges from 0V to 5V whereby the 0V represents the black section and the 5V is associated with the white section and has a rise and fall time of 25 nanoseconds.

It is important to ensure that the coded tape is correctly mounted with the overlap section not causing too much deviation in terms of the width of the black and white stripes. Using the diameter of the shaft at that section which is 29mm, the circumference of the shaft is obtained. However since the tape itself also has a slight thickness, it must also be added to the diameter. The total diameter of the shaft with the tape thickness was found to be 29.3

mm. With this value, the circumference is obtained and therefore the length of the tape required is found.

$$C = 2\pi r \quad (\text{Eq-13})$$

$$C = 2\pi(14.65) = 92.04\text{mm} \quad (\text{Eq-14})$$

The tape itself contains black and white stripes of 1mm width. From the length required it is seen that this would result in an approximately 92 black and white stripes being used. This essentially means that there would be 46 pulses per revolution. The presence of the extra 0.04 mm means that there is an overlap and would result in one of the pulses not being the same as the others. According to Resor et al. (2005), if these pulses differ from a perfect and ideal pulse section, the calculated torsional vibration will be subject to bias errors manifested as high-level order content. Since a method to eliminate the order content has been studied, this extra 0.04 mm should not pose a major problem provided the order content is eliminated.

Since only one sensor was available, it is important to locate the fibre-optic sensor setup in the correct position in order to obtain the best results. According to the FEM analysis, the first mode shape had the most response at the end of the shaft furthest from the motor. The 2nd mode shape however showed better response to be found closer to the disks. However as mentioned earlier, measurements is to be taken near couplings as this would be the most accessible points on rotors in industry. For these reasons the sensor and coded tape was mounted at the free-end of the shaft.

The distance of the sensor from the shaft is not extremely important but must be maintained within a zone such that the sensor will pick up changes in the strip. The main calibration of the sensor is in the gain setting. Once the fibre-optic sensor is mounted at a specific position, the gain setting is adjusted such that the output of the sensor is a perfect square wave. If the gain is set too high or too low, it would result in a biased square wave whereby either the 5 V or 0 V would be dominant. If the gain is set to its extremes, it would result in a constant DC output of 0 V or 5 V depending in which extreme the gain was set. This means that no square wave is obtained even if the shaft rotates.

For this setup, an oscilloscope was used to calibrate the system to the correct gain settings. This was done by starting the motor and visually adjusting the gain until a proper square wave was visible. For further refinement, the mean of the wave was observed and the gain adjusted such that the mean would be as close to 2.5 V as possible. The figures below show the sensor setup as well as the oscilloscope reading from different gain settings as compared to a good gain setting.

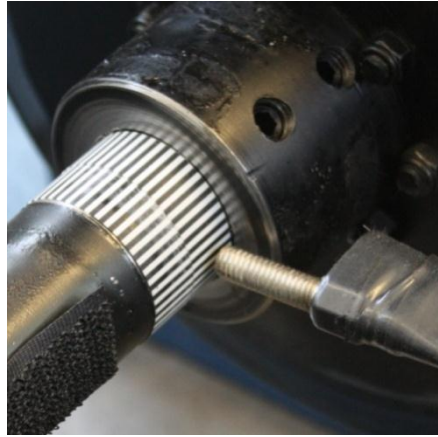


Figure 46 Optic sensor with coded "zebra" tape

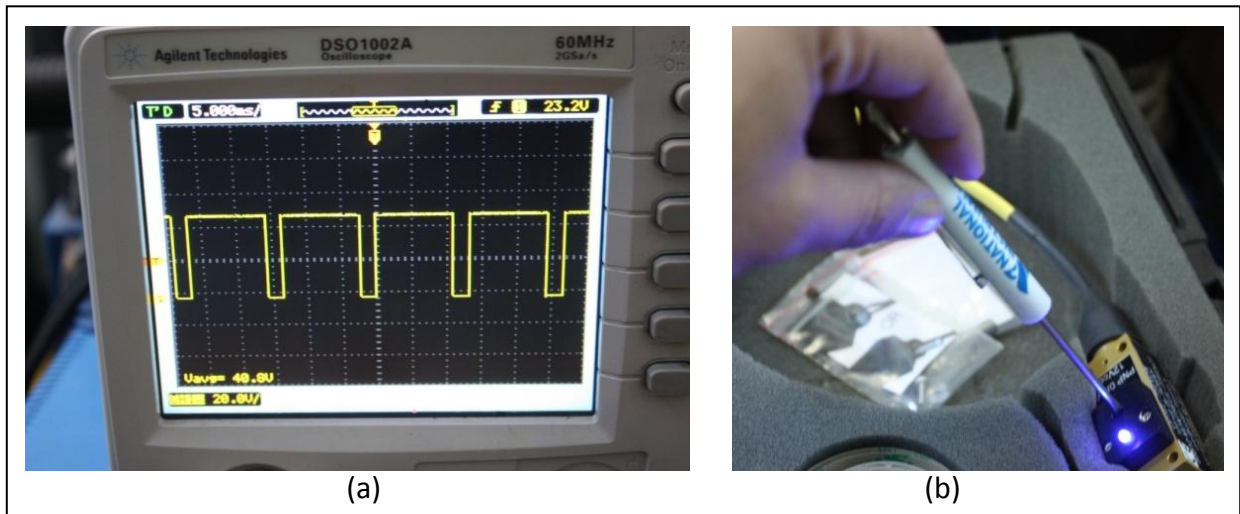


Figure 47 (a) Square wave with too much gain, (b) gain adjusted using screw driver

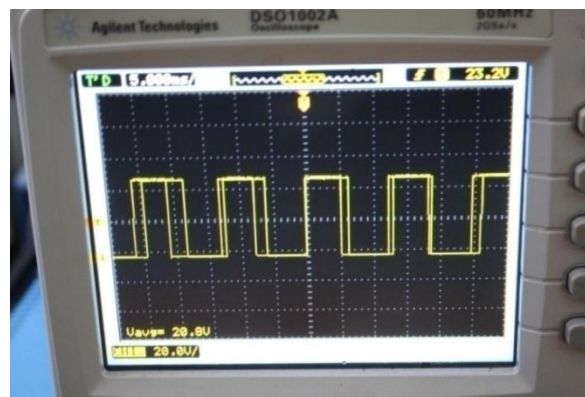


Figure 48 Gain set to produce a better square wave

4.5. Telemetry setup

Strain response of the system was measured using a telemetry setup. This wireless method ensures that no extra wires and slip rings are required for the strain measurement. The system used in this setup is the TorqueTrak 10K Torque Telemetry system. It utilizes digital radio frequency (RF) technology to transmit the data over a certain distance. It comprises two main components. The TX10K-S transmitter, which is mounted directly onto the shaft, is

connected to the strain gauge. The transmitter is powered by a 9V battery pack which is also mounted onto the shaft. The transmitter sends the signal to the second component which is the RX10K receiver. The receiver is placed a certain distance away from the transmitter. The signal at the receiver is then conditioned and processed according to user specifications before it is sent to the analyser where the time domain data may be viewed. The settings that can be adjusted and the processing are as follows (Binsfeld Engineering Inc.):

- Receive signal from TX10K-S
- Check for errors and display if any detected
- Check for simulated signal and apply if enabled
- Apply Filter (Specified by user)
- Apply AutoZero (Specified by user)
- Apply Polarity (Specified by user)
- Apply Gain (Specified by user)
- Apply Output Offset (Specified by user)
- Send signal to display, voltage output, and digital output

The components associated with the telemetry system may be viewed in Figure 49.

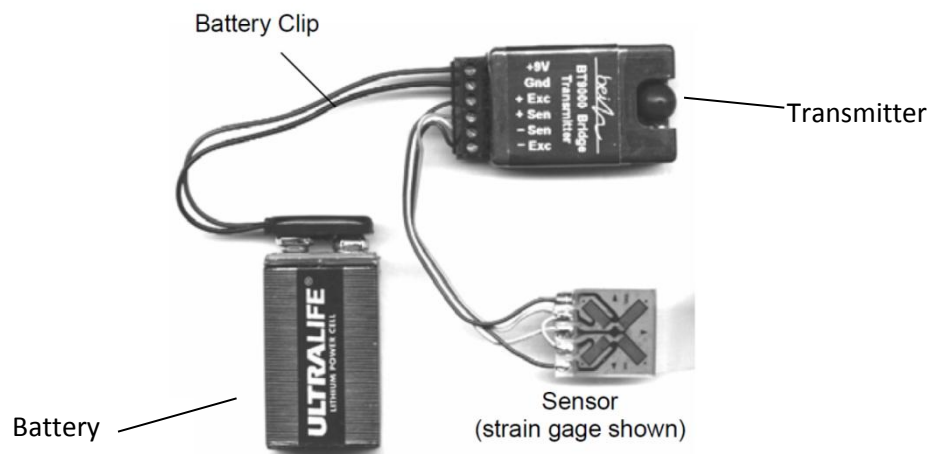


Figure 49 Components of telemetry system (Binsfeld Engineering Inc.)

Since torsional measurements are done, a torsional strain gauge was required. It is possible to use normal strain gauges mounted at 45° in order to capture the torsional strain, but for this study it was decided to use torsional strain gauges. The torsional gauges used were the KFG-2-120-D2-11 biaxial 120Ω strain gauge. Two gauges were required and were mounted 180° apart on the shaft. Figure 50 shows a diagram of the gauge used in this investigation and it is seen that the wires are at 45° representing a torsional gauge.

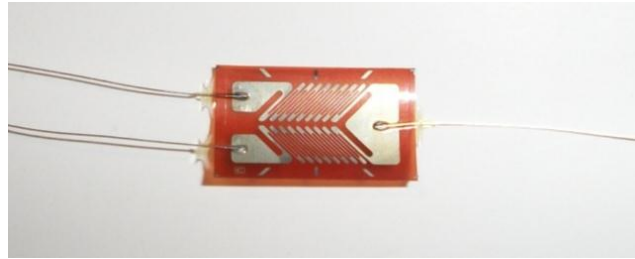


Figure 50 Torsional strain gauge

It is important to locate the strain gauge in a location where optimum results may be obtained. According to the FEM results, it suggests that slightly higher strain is obtained at the motor-end. For practical purposes of mounting the transmitter onto the shaft, it could not be mounted right next to the coupling and so it was mounted slightly more inward from the end. In order to correctly mount the gauge, the surface had to be cleaned correctly so that the gauge could be stuck firmly on the shaft. If this does not happen, there are possibilities of bubbles appearing representing the gauge is not perfectly in contact with the shaft, which would result in incorrect results. Once it is stuck, it is important to ensure that it is properly insulated so that there is no shorting of the strain bridge circuit. This was done using a thin film of insulation solution. The gauge was then covered using insulation tape for further insulation as well as to protect it from any damage.

Once the gauge was properly located, the wires were connected to the transmitter which could then be fixed to the shaft. This was done by first placing Velcro strips onto the shaft and the underneath of the transmitter and battery housing. This was done to put it roughly in its position. It was then tightly taped up using fibre glass tape to keep it firmly in position. This is very critical as if it is not tight, it can be potentially dangerous running at high rotational speeds. Figure 51 shows the telemetry setup on the shaft.

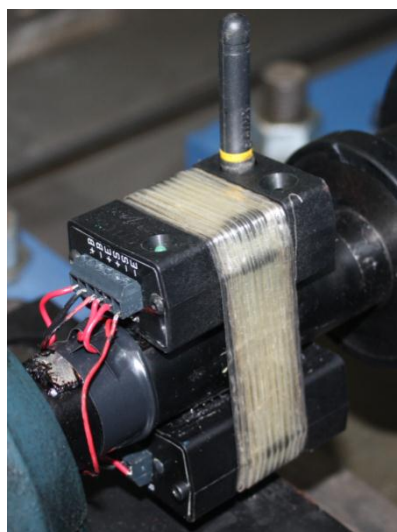


Figure 51 Telemetry system mounted on the shaft

The location of the receiver antenna is also extremely important. Sometimes interference may disrupt the signal and result in a poor time domain results. The receiver was located at

the far end of the test bench in line with the shaft. The loss in signal results in the reading over-ranging as it goes to an extreme value indicating that something is not correct. Figure 52 shows some over-ranging problems that would corrupt the signal. It is seen that until around 11 seconds, strain is measured. However due to a loss of signal, the telemetry loses the signal and goes into an over-range strain. This magnitude is quite high and would affect the time signal which is why it is important to ensure good signal transfer is continuously been made. This had occurred a considerable number of times during testing. A variety of checks were done by testing the wire and battery connections, the transmitter and receiver antennae as well as checking the strain gauge. None of these seemed to solve the problem. Eventually a new system was tested and this worked fine. Further tests were done with the new system.

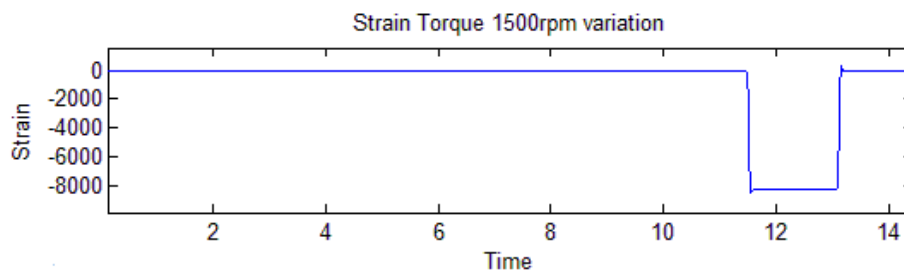


Figure 52 Loss of strain signal resulting in over-ranging

Once the telemetry system was setup, calibration was performed. Since the output from the system would be a voltage reading which would be meaningless in the analysis, the calibration process was to relate the voltage to strain values. The method used for this was the shunt calibration method. This involved applying a high resistance to the bridge equivalent to a torque being applied to the system. This would change the voltage reading as would happen if a torque was applied.

It was further decided to verify this calibration by using the brake system to keep the free-end of the setup fixed while a torque was applied, through the use of a weight, at the motor-end of the shaft. Since the torque applied is known, one can verify the expected strain values due to the twist in the shaft from analytical methods.

4.5.1. Shunt calibration

As mentioned, this involves applying a resistance over the bridge which would alter its resistance in a similar way it is altered if a torque is applied to it and is shown in Figure 53. There are specific resistances that may be applied which result in known strains being represented. For this case 120 Ω gauges are used and therefore a 120 k Ω was used as a shunt resistor. The equivalent microstrain due to this load is 500 $\mu\epsilon$. A table of this is shown in Appendix D. The strain is still measured in volts thus far. Therefore applying the load would result in a voltage reading. This change in voltage is related to the equivalent microstrain. From this calibration it results in a 620 mV change in voltage. Thus,

$$620mV = 500\mu\epsilon \quad (\text{Eq-15})$$

$$\frac{620mV}{500\mu\epsilon} \tag{Eq-16}$$

This results in a calibration factor of 1.24 mV/μϵ, which is applied to the volt signal to convert it into strains.

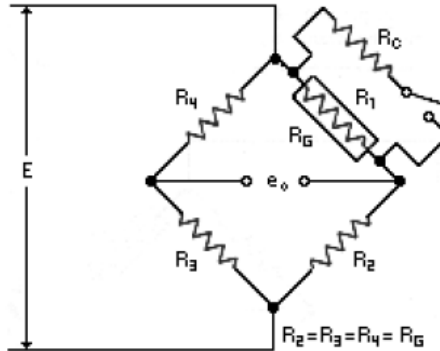


Figure 53 Shunt resistor applied to bridge (Technology, 2000)

4.5.2. Torque-Load calibration

In order to verify the result, a brake was applied to the free-end of the shaft while a load of 10 kg was applied at the motor-end. This was applied to the coupling off-set from the centre which resulted in a known torque in the shaft. By doing some simple analytical calculations, the torque that results is computed. This mass is applied at a radius of 40mm for the shaft centre and results in an applied torque of 3.92 N.m.

$$T = Fr \tag{Eq-17}$$

$$T = (10)(9.81)(0.04) \tag{Eq-18}$$

$$T = 3.92N.m \tag{Eq-19}$$

Using this in a FEM model, the expected strain may be computed numerically by doing a linear static analysis. Figure 54 shows the result of this. It is seen that a surface strain of 5.26 μϵ is expected.

In the experimental test, the strain was zeroed at A and then the load was applied during B. This resulted in a strain reading shown in Figure 55 below. This result shows that the load caused a stabilised strain at C of 5.124 μϵ. This correlates well with the numerical model and verifies that the strain gauge calibration is correct and also validates that the gauges were mounted correctly.

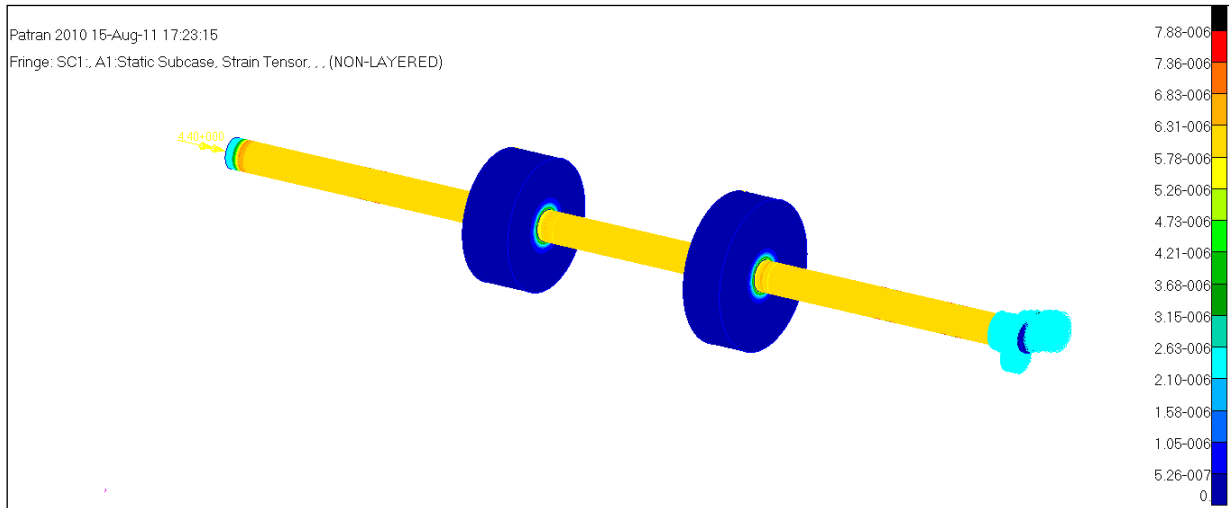


Figure 54 Torque load applied to FEM model for strain result

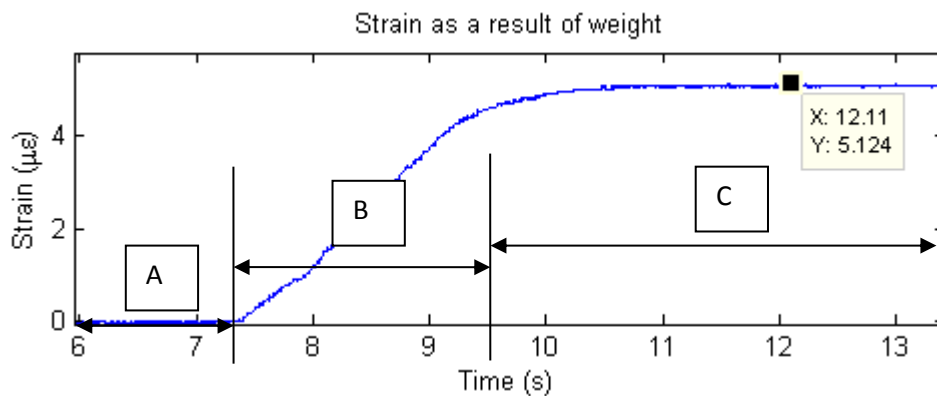


Figure 55 Resulting strain from torque load calibration

4.6. Digital Image Correlation (DIC) system setup

The setup using the photogrammetry system was done using the PONTOS system from GOM. This system is a non-contact optical 3D image capturing measurement system. It analyses, computes and documents object deformations, rigid body movements and the dynamic behaviour of the measuring object. PONTOS is software which can precisely locate round markers that are stuck onto the object by the user and to continually monitor the changes in their 3D orientation with reference to its starting point. This is done by a digital stereo camera system that records different load or movement states through a series of images. The software then assigns coordinates to the image pixels and compares digital images in order to compute relative displacement of the markers and other reference points. The Figure 56 below shows a schematic view of the camera setup and some dimensional terms that will be used for calibration and testing.

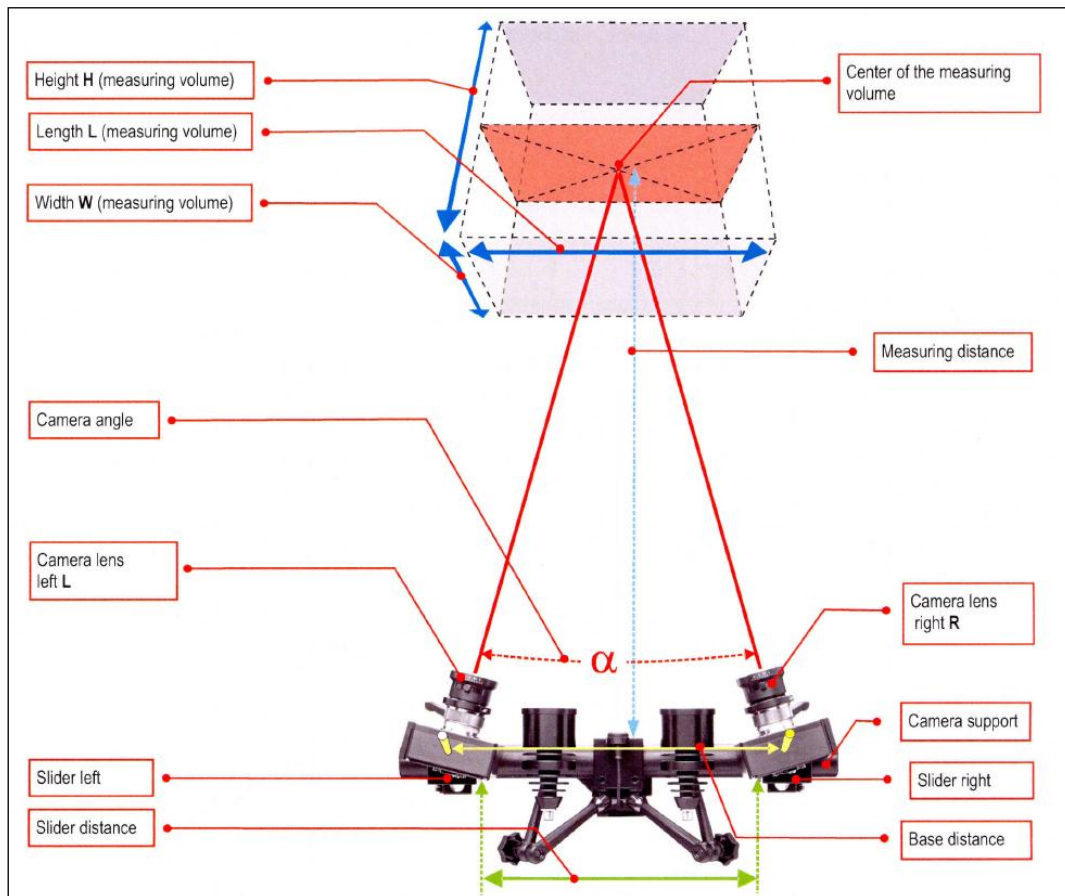


Figure 56 Camera setup and dimension descriptions (GOM, 2010)

The setup of the system involves two parts. The first is to calibrate the system according to the object to be measured and the second is to ready the measuring object and set it up according to how the system was calibrated. The calibration procedure is discussed first. This will then be followed by the setup done specifically for this project.

Calibration is done by doing a simple measurement process on a calibration object in order to adjust the measuring system, in this case the cameras, such that the dimensional consistency of the measuring system is ensured. This basically can be interpreted as ensuring that both cameras are properly focussed and that the orientation of each camera relative to each other is known. Based on this information the software can then take the 2D image from image from each camera and combine them in order to accurately create a 3D image of the system thus insuring accurate results. During the calibration process, images of the calibration object will be taken in different orientations to capture the entire measuring volume. It is also important that the lighting used during calibration must be the same during testing.

For this calibration, the calibration cross object will be used. Since the main testing involves capturing images of a rotating shaft, it makes it a dynamic analysis. In order to properly capture the object which is moving at high speeds, the system uses strobe lights. This in essence allows the object to look stationary while the strobe light is illuminated allowing for

the camera to capture an image that does not look blur and may be used for post analysis. For this reason, the strobe light must also be present for the calibration since the same lighting is required as mentioned before. Figure 57 below show the calibration cross object as well as the camera setup with the strobe lights.



Figure 57 Calibration setup, calibration cross and strobe light positions

In order to complete calibration the following need to be completed. All references to distances and names are referred to as in Figure 56. Reference to PONTOS specifications in terms of measuring volumes may be found in the Appendix D.

- Adjust measuring distance- This value is dependent on the measuring volume. For this setup which comprises of a 880 mm long shaft and maximum width and height of 144 mm, the closest measuring volume as stated by PONTOS is 1080x730 which results in a measuring distance of 1285 mm.
- Slider distance- The slider distance according to the PONTOS specification for the measuring volume is 542 mm.
- The camera is then adjusted such that the laser in each image coincides with the cross hairs on the screen. An example of this is shown in Figure 58.
- The focus of each lens is then adjusted. This is done by zooming in onto one of the coded marking and adjusting the focus until both images are as clear as is possible.
- It is recommended that the aperture be left completely open. However for cases where extra lighting is used, in this case the strobe lights, the aperture was closed slightly to avoid over exposure.

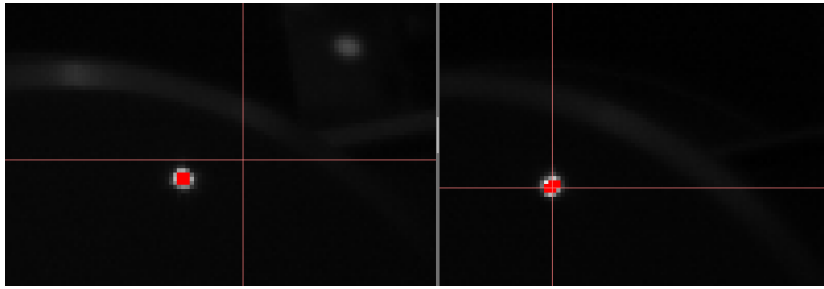


Figure 58 Camera adjusted such that laser appear on cross-hairs, Left camera not set, right camera correctly set



Figure 59 Focus set such that blurry images like left camera adjusted to focus as in right camera

Once the above settings are completed, the calibration process may begin. The calibration comprises of taking 16 images of the cross in 16 different orientations. Once the calibration is completed, a summary is created by the software specifying 2 vital details about the setup. The first is the calibration deviation value and the second the pixel value. It is important that these values fall within a certain limit otherwise the calibration is not valid and further testing would result in inaccurate results. Table 6 shows this summary and according to PONTOS specifications, the values do fall within the limits and therefore the calibration process was successful.

Table 6 Calibration table parameters

Results	Value
Calibration deviation	0.017 pixels
Scale deviation	0.008 mm

After calibration, the first step is to setup the camera unit at the same distance from the object as was done during calibration. As mentioned earlier the measuring distance is 1285 mm. The lighting must also be set the same with the strobe lights set in position. The main setup of the object to be measured may now be set for testing.

The first step is to mark the measuring object with point markers. These are the round white stickers that the software will look for during the analysis procedure and therefore must be applied to the areas of interest on the object. The PONTOS system uses markers with a defined geometry and high in contrast whereby it has a black background and white centre in order for better capturing during analysis. These markers come in a variety of sizes and the correct size must be chosen which depends on the size of the object or measuring volume as it will now be referred to as. It is suggested that the size must be chosen such

that markers in the camera image should span between 6 to 10 pixels for it to automatically be detected by the software. For this setup the 8 mm markers proved to be sufficient and may be seen in Figure 60. Additional markers are also required on non-moving parts. These will serve as reference points during the analysis.

As mentioned earlier, the markers are designed for high contrast in colour. Since the shaft is made of steel, the surface is shiny and may cause high reflection and possibly make the markers hard to find. For this reason, it was decided to spray the shaft with a matt black paint. This would ensure less reflection and better visibility of the markers. The figures below show the overall setup of the DIC system.

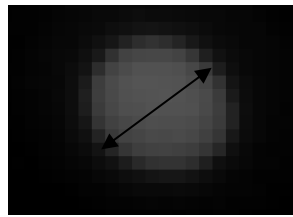


Figure 60 Object markers showing a span of 10 pixels



Figure 61 Overall rotor and test equipment setup

4.7. Tachometer setup

The tachometer setup was used in order to capture a one times per revolution signal. This was done using an SKF tachometer. This would eventually be used to get data about rpm speed and also during post analysis for order removal. The setup involved using a tachometer at the motor end of the shaft and used a reflective tape as the 1x trigger. This may be seen in Figure 62.



Figure 62 Tachometer setup with reflective tape

The fibre-optic sensor renders 46 pulses per revolution. Figure 63 below shows the constant periodic tacho pulse that is expected during a constant speed run. A zoomed in plot shows that there are 46 square wave pulses from the fibre-optic sensor. However when tests were done with the DIC system and the strobe lights were in operation, it corrupted the tacho signal. Figure 64 shows this corrupted signal whereby multiple pulses occur in one revolution. It was therefore decided to abandon this tacho setup.

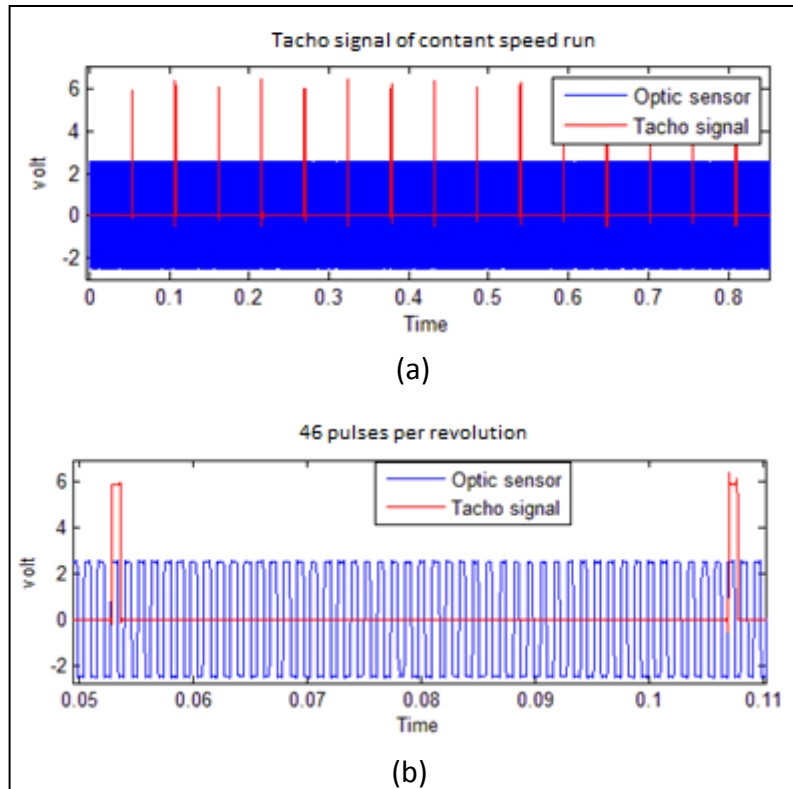


Figure 63 a) Periodic tacho signal for constant speed run, b) Tacho signal showing 46 optic sensor pulses per revolution

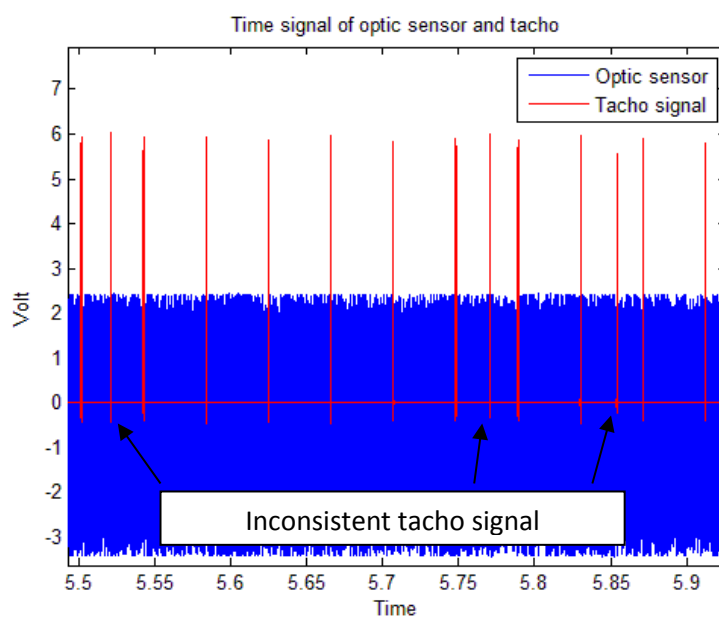


Figure 64 Inconsistent tacho signal due to strobe lights

4.8. Test procedure

It was decided to run the shaft while recording data using all three methods simultaneously. This was done so that the data collected could be under same running conditions. This also allowed for comparison of the results and to see which results gave the best responses. It was decided to do three types of tests. A run up test and two tests at constant speeds were carried out.

The run-up test involved running the shaft from 0 RPM and gradually increasing the speed. This allowed for the response to be monitored under a constantly changing condition. The constant speed tests were done at 1100 RPM and 1640 RPM running for 2 minutes. These specific speeds were chosen for reasons that will be explained later in this section. The constant speed tests were done so as to monitor and investigate the shaft response under normal operating conditions. For the fibre-optic sensor and the telemetry system, the time domain data was recorded in the analyser directly and saved in order to be later analysed in Matlab. The DIC on the other hand has its own software system and the data was recorded there as well as partially analysed there before bringing it to Matlab as will be explained in the next chapter.

Once these tests were done on a healthy rotor, damage was inserted into the shaft and the same procedures were followed again. Damage was introduced by using a hacksaw and sawing the shaft at the centre removing material which eventually looked like an “open crack” developing in the shaft. This was done for seven damage states where each state represented a bigger damage. This damage started with a 5% crack depth until a 66% crack depth was created for the last test. Once all these tests were performed, post analysis could be done and the results compared and analysed.

There was however some challenges encountered, especially with the DIC system, with the regards to the test procedure used. These are addressed below:

The shaft would be running at high speeds and though the camera has the capability of capturing images up to 480 Hz, which would result in measurable frequency content of the system up to 240 Hz according to the Nyquist sampling theory, the dynamic case means the strobe lights are needed. The strobe lights available had a limitation of operating at 15 Hz. Even though 15 Hz was possible, operating at this frequency for long periods of time lead to some delay problems which resulted in images being taken under dim lights. For optimum results it was suggested to use 7.5 Hz. It was decided to push the limit slightly and a test was done at 9 Hz which resulted in good results. Therefore for all DIC system tests, 9 Hz was used as the sampling frequency.

It is due to this fact that undersampling methods were introduced to the analysis. In order to effectively use undersampling the shaft could not be operated on 9 Hz or any multiples of 9 Hz either as this would simply result in the camera taking the same image each time. The shaft needed to be run just over the 9 Hz frequency. However at such a low speed, no

response is expected. Therefore it was decided to use speeds just over 2x and 3x the 9 Hz frequency. This resulted in the tests being done at 1100 RPM and 1640 RPM which are 18.33 Hz and 27.33 Hz. This meant that the camera would capture the image every 2nd and 3rd rotation respectively.

Another problem faced was that during the run-up test, the shaft speed is constantly increasing. This meant that undersampling using the DIC system would result in images being taken completely out of sync to what is required which would result in meaningless data to be analysed. For this reason it was decided not to use this system for the run-up tests and only data from the fibre-optic sensor and telemetry would be used.

The last challenge faced was that due to the strobe lights being used, it results in the tachometer reading incorrect data due to extra triggering as a result of the light from the strobes. Even though shielding was attempted, the tachometers results were not consistent and for this reason it was decided not to use it for further testing. Instead, the fibre-optic sensors square wave was used. Through some post analysis coding using Matlab, a 1x revolution signal could be obtained from the 46 pulse per revolution fibre-optic signal.

5. Chapter 5- Post-processing and Observations

5.1. Overview

The previous chapter discussed the equipment used as well its setup for testing. Using the test procedure mentioned earlier, the procedure of conducting the experimental testing is undertaken in this chapter.

This chapter discusses individually the post-processing techniques, observations and initial results obtained from each of the test equipment used. Explanation for each of the results obtained is examined and discussed and from this some conclusions and a few recommendations are made.

5.2. Post-Processing and Observations

The results from each of the three measuring devices are all investigated in the time domain. From there they are converted into the frequency domain using the FFT algorithm in order to investigate the frequency content of the system. As mentioned in the previous chapter, each run would take 2 minutes. This was done in order to allow for averaging of the signal to be done, once processed. In order to look at the result of this, the time signal needed to be processed and plotted on a waterfall or spectrogram plot. This would allow a clear visualisation of the operating frequency change through time as well as all structural dynamics that exist in the system.

For the constant speed runs, the time signal would be divided into four equal parts meaning that each time signal analysed would be 10 seconds long. This therefore meant that 12 averages could be taken of a test run. At 10 seconds per run, this meant a frequency resolution of 0.1Hz could be attained. In order to obtain this sort of resolution the FFT must be created in a way so that this can happen. Frequency resolution in terms of an FFT is defined as the sampling rate divided by the number of FFT points. For this case the sampling was done at 51200 Hz. In order to obtain a 0.1Hz resolution, an FFT size of 512000 was used.

In the case of the run-up tests, the speed is constantly changing. This means that taking a longer time average would result in not fully capturing the changes in speed. In order to counter this problem and capture the changing speed better, the signal was divided into 100 sections which resulted in each time length of 1.2 seconds. This allows for better visualisation of the changing conditions. Although this compromised the frequency resolution for detecting damage, it was no big concern since the main focus was to detect damage under constant operation and not transient operation. The main purpose of doing the run-up speed test is to basically separate the harmonics of operation from the structural vibration present during operation as will be seen a little later in this chapter. However once a good visualisation was done in order to see where exactly the dynamics are present, an analysis was done with a longer time signal in order for damage detection.

The above discussion therefore meant that the spectrogram plots of the run-up test would contain 100 frequency plots bunched together to form an even distribution of the changing conditions. The constant speed runs on the other hand would only contain 4 plots bunched together since no changing conditions would need to be captured and allowed for better averaging and frequency resolution for better damage detection.

The spectrogram is good for visual understanding of how the system operates over time. In order to look at specific frequencies and the changes thereof, it makes more sense to look at the averaged signal on a 2D frequency magnitude plot. The average signal of the divisions mentioned above were taken and plotted using the FFT algorithm. It is in this signal that the expected changes due to damage should be seen. Although it is visible in the spectrogram, the 2D plot shows this comparatively better. The spectrogram and 2D plots are implemented for all the tests carried out for all the measuring techniques.

5.2.1. Fibre-optic sensor

Figure 65 below shows a spectrogram plot of the run-up test. The colour map is an indication of the magnitude of the response at that specific time and frequency. In this figure there are clearly distinguishable diagonal order lines. These order lines show the change in frequency with time which represents the increase in shaft speed. The first order line visible on the left side and marked with an A represents the actual run-up frequency. The other diagonals present are higher orders of the running frequency, which are expected to be there as they are commonly found in rotating machinery. Another clear feature is the vertical line that does not change with frequency over time, marked with B. This is a structural resonant frequency of the system and represents the torsional resonance of the rotor. This fact is further revealed once damage is introduced into the system. Once damage is introduced, the flexibility increases and the natural frequency would decrease which is the case of this frequency as will be seen later in chapter 6. As can be seen it roughly lies between 100 Hz and 150 Hz and with further investigation shows it to be in the 120Hz region. The expected frequency according to the FEM analysis was 133.02Hz. A second frequency was also expected to be observed at 409 Hz; however, it is not picked up in the spectrogram plot in Figure 65.

This plot also reveals dynamic behaviour mirrored around the structural resonance frequency, and represented by C. Further investigation revealed that these responses are equally spaced on each side and the width D is equal to the rotational frequency at that time. These are side-bands and result from amplitude modulation whereby two signals, in this case the operating and structural resonant frequencies are multiplied together. In some instances it may pose a problem where multiple signals are modulated and even harmonics of these side-bands are present and the signal requires demodulation. In this specific case, a faint first side-band is present with no harmonics visible. The structural resonant frequency is clear and as will be seen in later figures, further processing is not required.

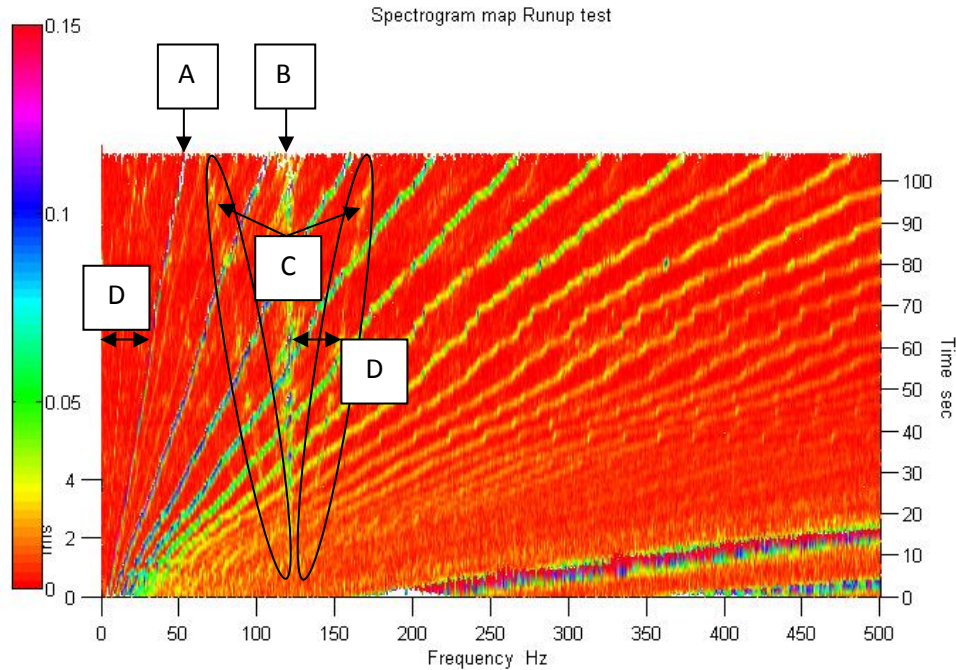


Figure 65 Spectrogram of runup test

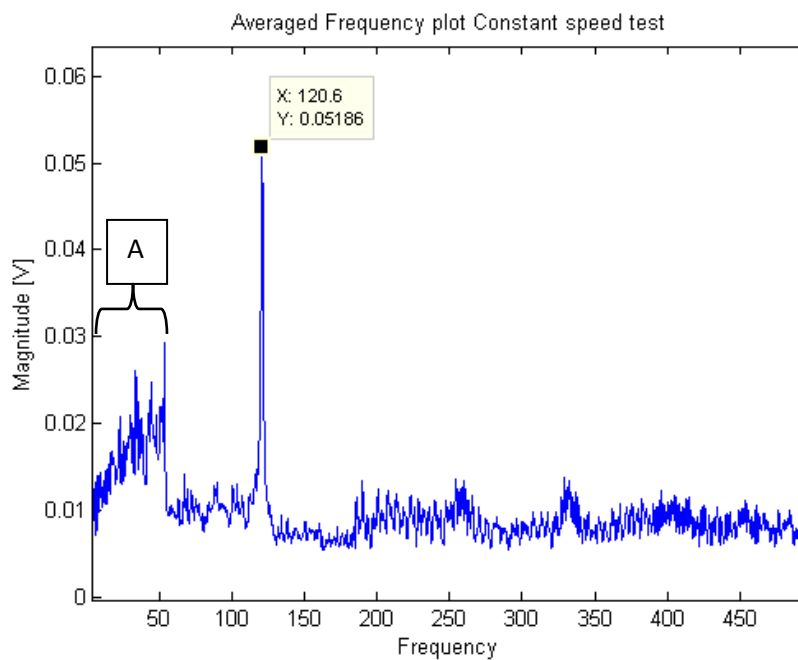


Figure 66 Averaged 2D plot of runup test

Figure 66 is an averaged 2D frequency plot of the run-up test. It is now known that there exists some dynamic frequency in the 120Hz region. But in order to get an exact value, an average over the entire time run was taken and plotted. As seen, the first peak at A is a distribution over a range of frequencies which is representative of the averaged running frequency. The frequency that is of interest would be a distinct peak at a specific frequency. In this test run it was found to be at 120.6 Hz. This represents the first torsional frequency of the rotor. Also seen in the figure is another range of peaks to the right. These are the averaged harmonics that result.

From the above figures it is clear that the fibre-optic sensor does indeed pick up a torsional frequency. The results of the constant speed run can now be studied. The spectrogram of the constant run at 1105.8 RPM or 18.43 Hz is seen below in Figure 67. Here the diagonals seen earlier are absent since the frequency remains constant. Instead there are clear vertical lines present. The first line A is at 18.43 Hz and represents the rotational frequency with many harmonics of this frequency visible. In this way it would be hard to identify which frequency represents the structural frequency and now it is clear how helpful the run-up test proved to be. However it is now known that the frequency occurs at 120.6 Hz and in Figure 67 it can be seen there exists some extra activity in that region represented by B.

As in the case earlier, the signal was then plotted on a 2D plot with 4 averages. This is seen in Figure 68. In this figure it is apparent that the harmonics are very dominant. The natural frequency is present but very much hidden amongst the rotational frequency orders. With a close look at the frequency region of interest, the torsional peak is visible at 120.6 Hz. However, this is not ideal and therefore the order removal technique was employed.

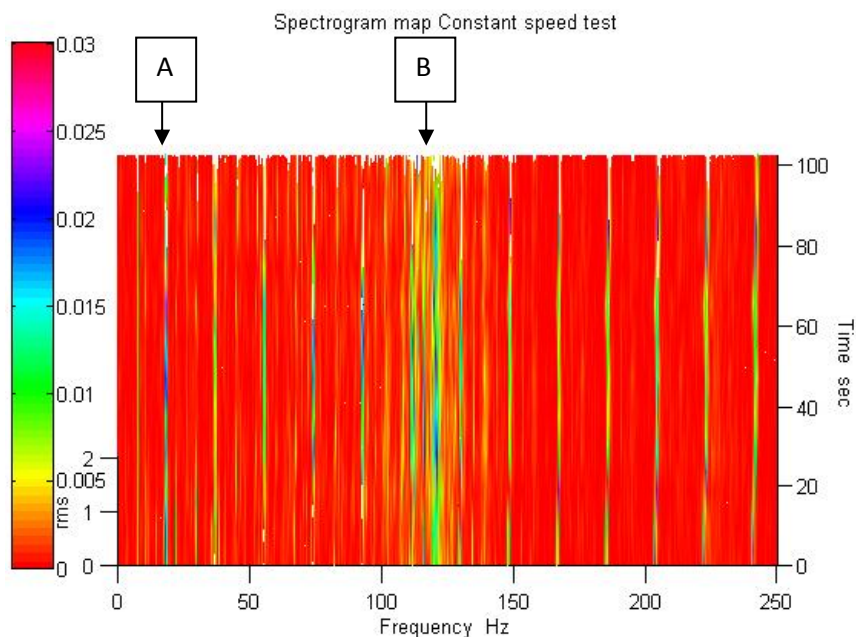


Figure 67 Spectrogram plot of Constant speed test run

Further processing was done in order to remove the orders. The steps followed were those mentioned in chapter 2.3 and briefly mentioned here. The constant time sampled signal is converted to a constant angle sampled signal. An FFT is applied to this signal and a magnitude order plot is obtained. From this the orders are removed and an inverse Fourier transform is applied to convert it back to a constant angle signal. Through interpolation, this is converted back to a constant time sampled signal. An FFT may then be applied to obtain an order free frequency domain response.

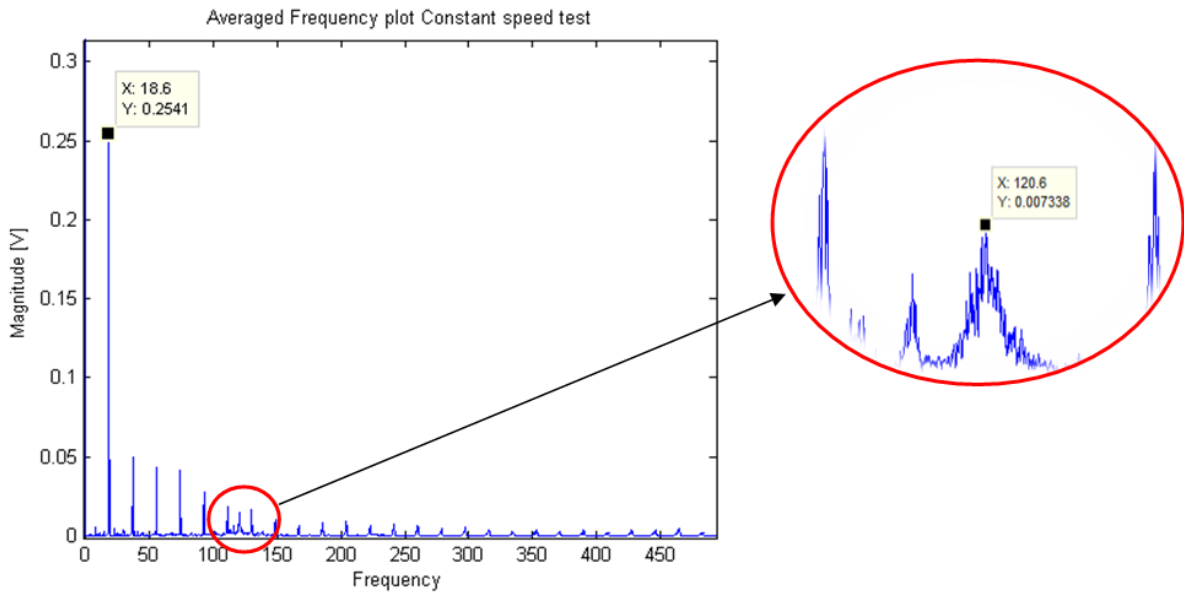


Figure 68 Averaged 2D plot of the constant speed test run

Below are the results from this process. Figure 69 shows the square wave with constant time and constant angle sampling. It might look like they are the same but the constant angle signal will simply contain information about the rotational frequency which is related to the orders. Figure 70 then shows an FFT plot of the constant angle signal. According to the frequency plot in this figure, the torsional frequency is to be present at 120.6 Hz which in the order domain should be present between the 6th and 7th orders which do occur. The orders are then removed and this may be seen in Figure 71 where it is compared to the original plot.

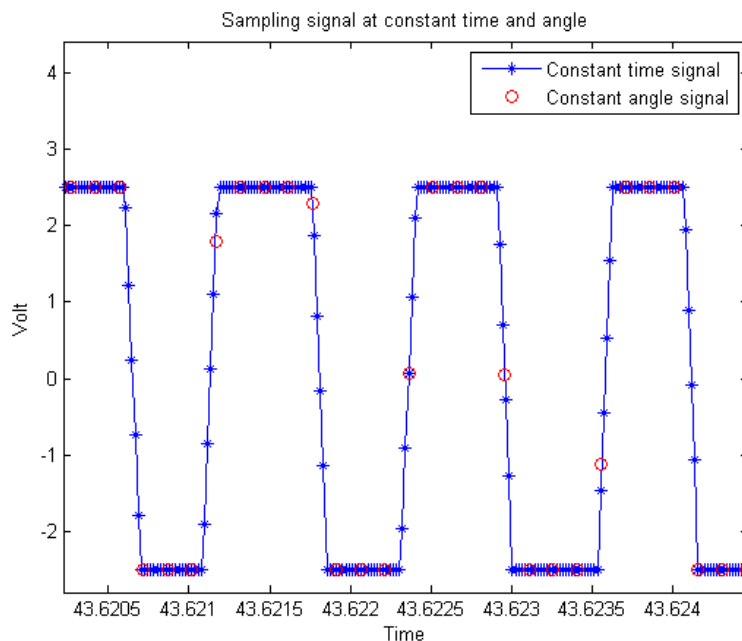


Figure 69 Constant time and angle sampling

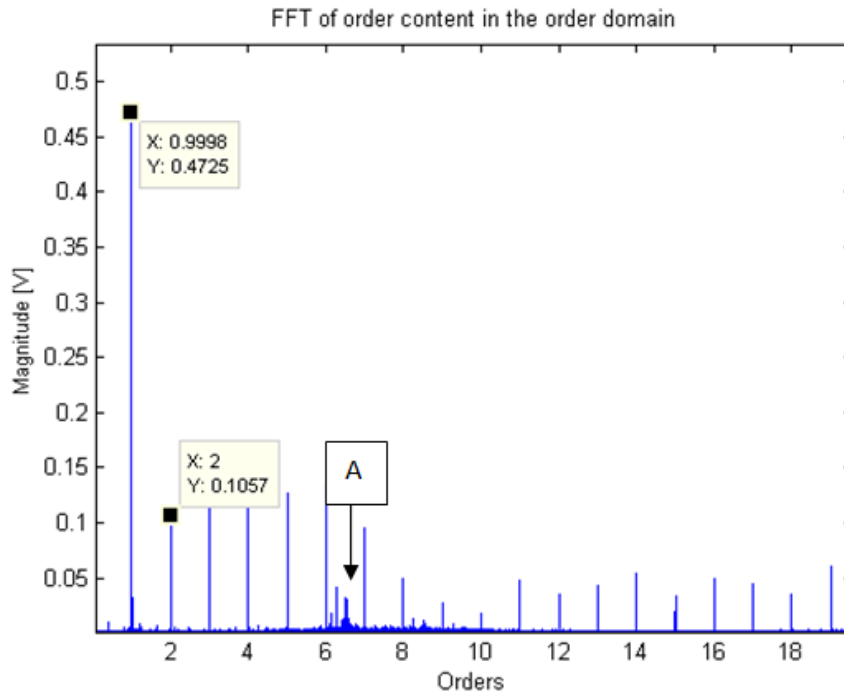


Figure 70 Order content FFT

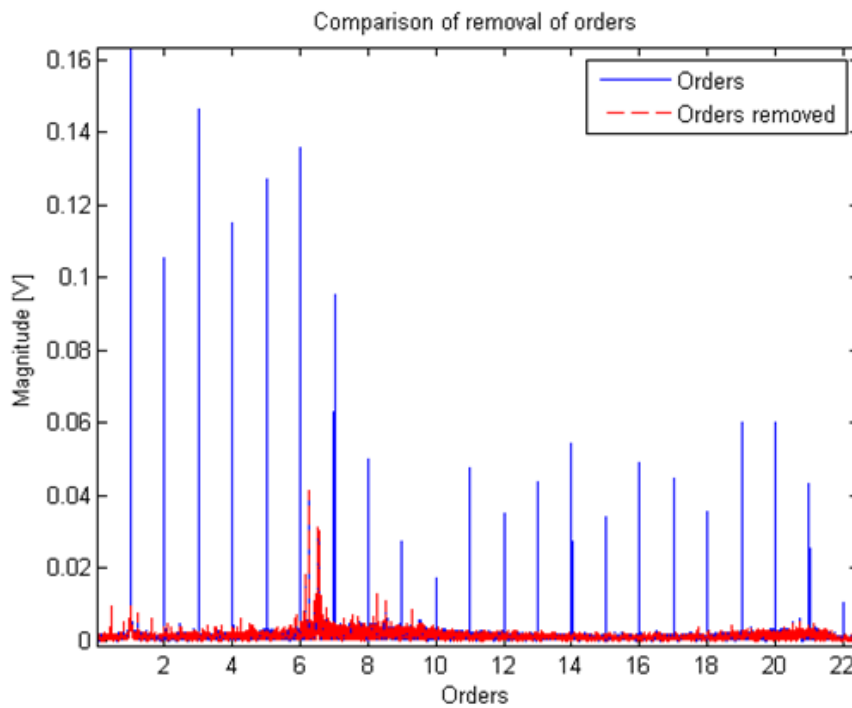


Figure 71 Comparison of order plot before and after orders removed

Once this is complete, the signal is moved back to the constant time sampling domain and an FFT may be applied to it. Figure 72 shows the frequency domain plot of the order removed signal. Although the orders are still slightly present, the torsional frequency that is of interest has a better relative magnitude and now has a clear presence. This same technique is applied to all the other fibre-optic sensor tests done including the damaged case and the final results may be seen in the next section.

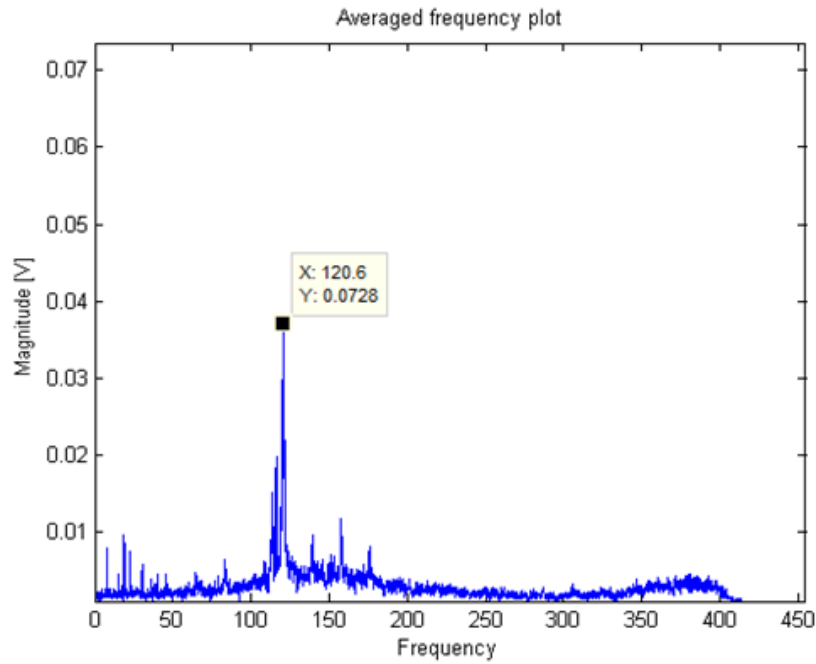


Figure 72 Frequency domain with harmonics removed

Tests were also done at approximately 1640 RPM. The order removed result of this is seen in Figure 73. However at this speed, although the torsional frequency is present it is not as clear as for the 1640RPM results. It is possible that at this speed the torsional mode is not excited as much as at 1100 RPM. Therefore further results using the fibre-optic sensor will mainly be concerned with those done at 1100 RPM with some references made to the higher speed runs.

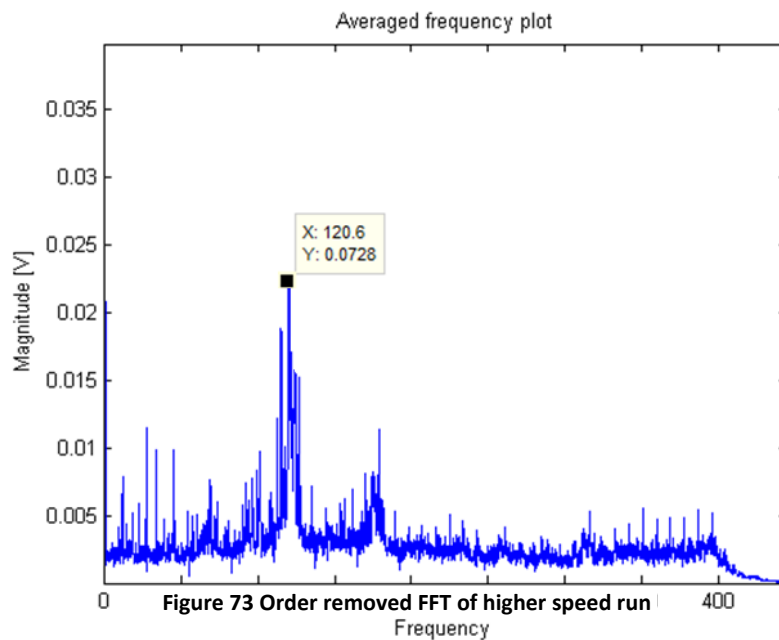


Figure 73 Order removed FFT of higher speed run

5.2.2. Telemetry strain gauge system

The spectrogram of the run-up test using the telemetry system that measures strain may be seen in Figure 74. Similar to the fibre-optic sensor, the diagonal peaks representing the operating speed and harmonics is observed. However, it is seen that there are no distinct peaks at the 120.6 Hz frequency. There does however seem to be peaks at multiples of 50

Hz. This most likely represents electrical noise of the system since the electrical line frequency is 50 Hz and this is present from time 0 s which suggests it cannot be structural.

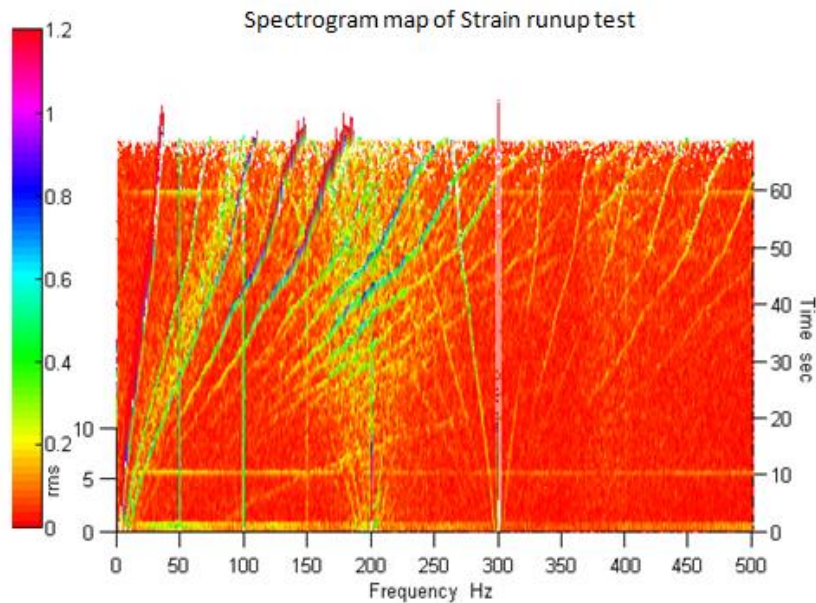


Figure 74 Spectrogram of Runup test for strain

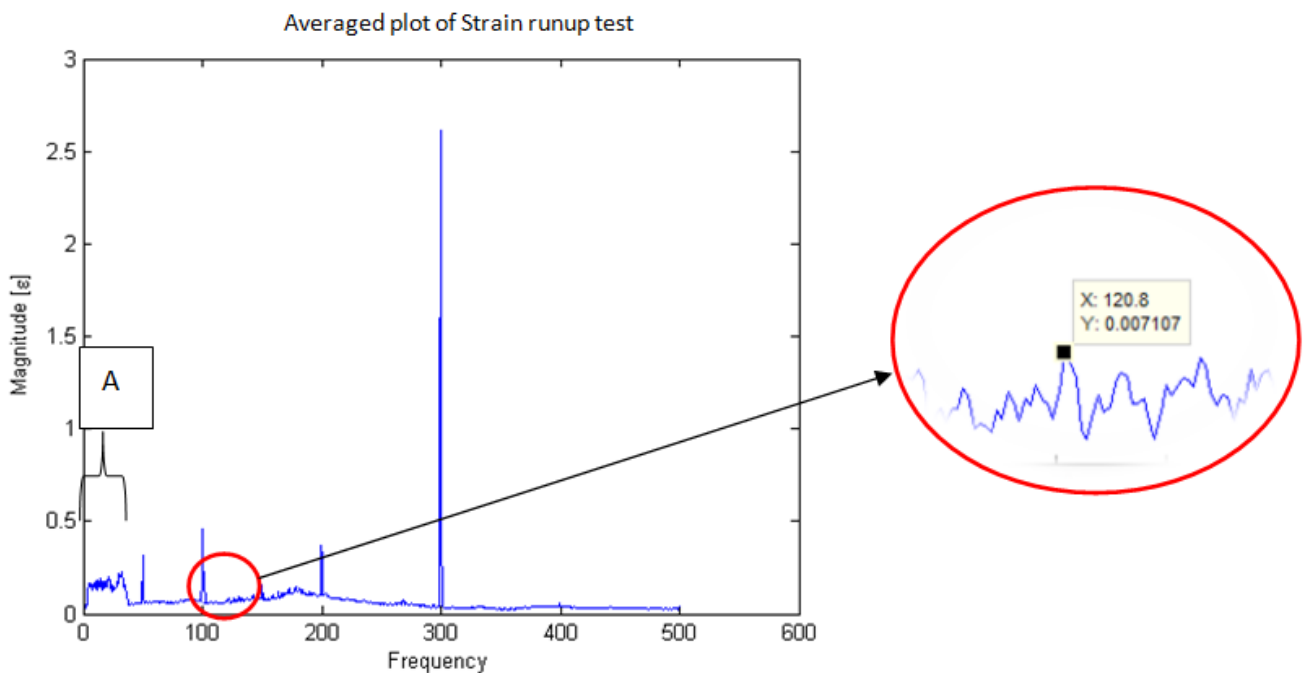


Figure 75 Average 2D plot of Runup test

Figure 75 above shows the averaged plot of the runup test. In here we see the expected distribution of energy over the frequency band indicated by A which represent the runup frequencies. However as seen in the spectrogram, there is no distinct peak at the natural frequency. A zoomed in investigation shows some sort of peak at 120.8 Hz. This is however not a distinct peak and would be hard to identify if the fibre-optic sensor did not give a clue of where to look. It can clearly be seen that the operating frequency is much more dominant than anything else. The electrical noise frequencies are also present which might look like

rotational speed harmonics but are in fact electrical line frequency harmonics. From the run-up test it was seen that no discrete dynamics were present despite the speed changes.

A constant run test was investigated and its result is shown in Figure 76. Again it is observed that the rotational frequency is present but nothing relating to torsional frequency. Order removal was applied as done for the fibre-optic sensor and the result is seen in Figure 77. On this plot there is no distinct peak at the 120.6 Hz or 120.8 Hz as found in the runup test. Instead there is a variety of peaks in the 118 Hz region. It is still unknown whether this represents anything meaningful until further analysis is done.

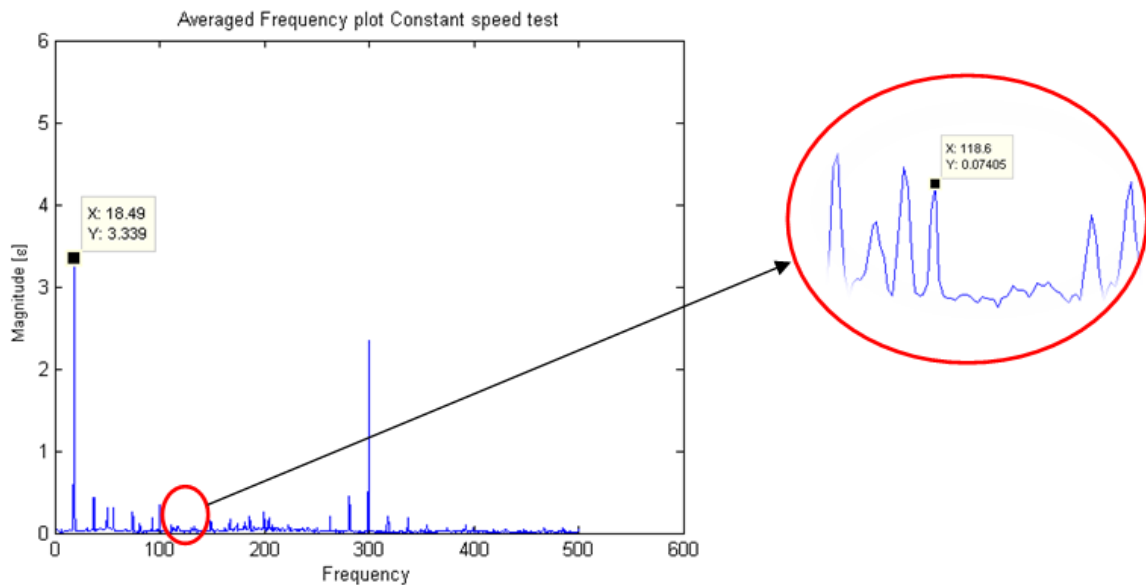


Figure 76 Constant run test of strain

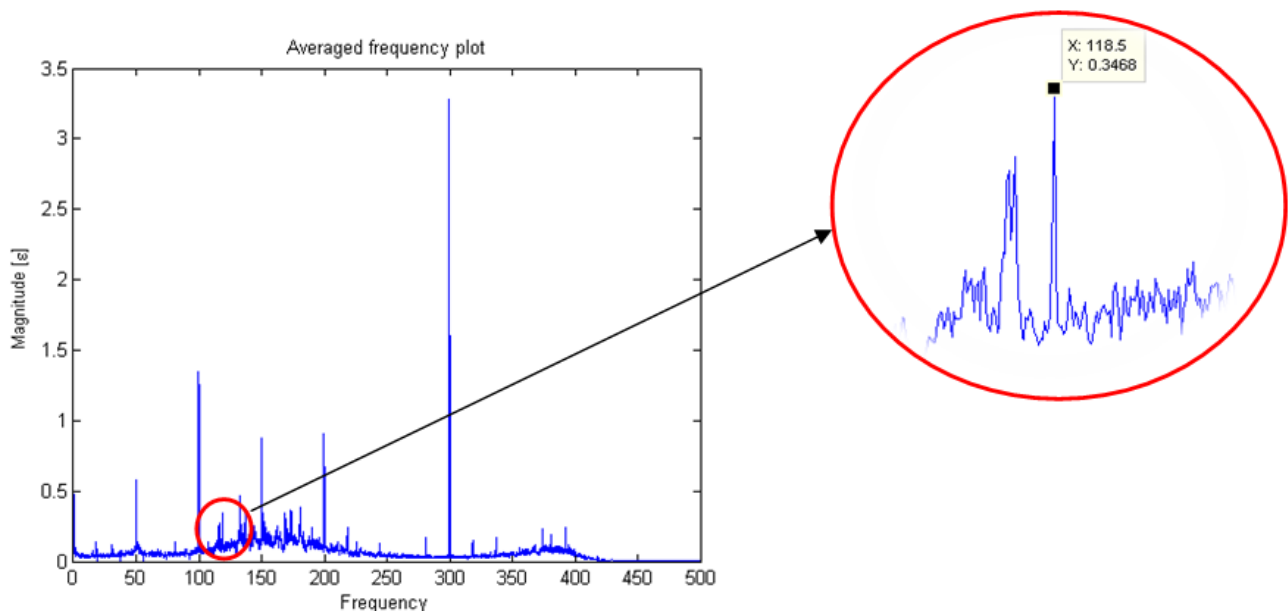


Figure 77 Harmonics removed Strain Frequency plot

The test was then done at the higher speed constant run, and even here nothing conclusive was observed. This is shown in Figure 78. It is seen that the peaks observed before have diminished. To examine why no result was picked up in the frequency domain, the strain signal in the time domain was investigated.

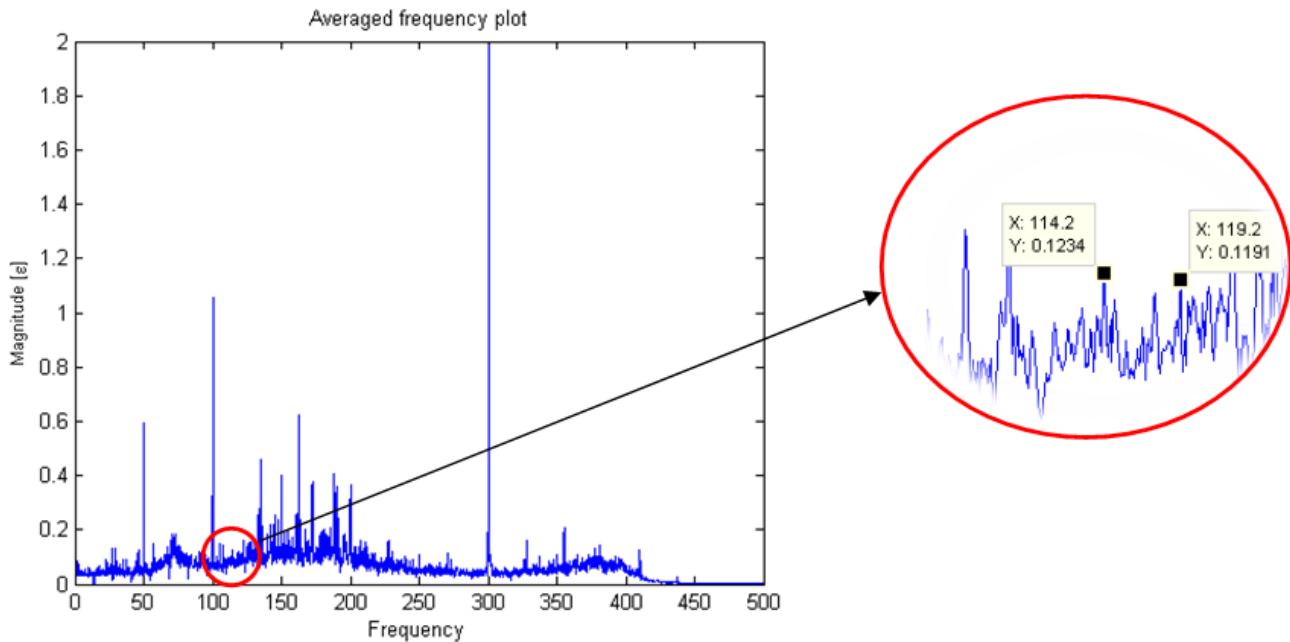


Figure 78 Order removed Frequency plot of higher speed test run

Figure 79 below shows the time signal of the strain. Already here it is seen that the strains are quite small ranging from -10 to 10 $\mu\epsilon$ resulting in a range of 20 $\mu\epsilon$. Even though it may be small, a closer look shows a periodic signal which is the rotational frequency and this was clearly seen as a peak in Figure 76. This means that the signal is at least capturing some useful correct data. What it does suggest in terms of the dynamics is that essentially not enough strain exists in the system that sufficiently excites the torsional mode with high enough strain to be investigated. Further investigations' regarding this issue is addressed in chapter 6.4. Another observation is that a higher frequency signal is present within this and some quick calculations on the length of each pulse reveal that this is the 300 Hz.

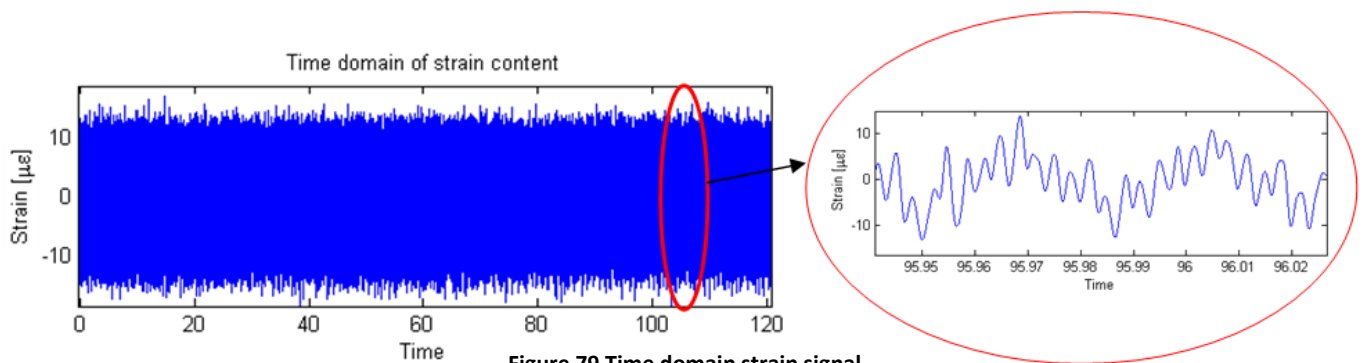


Figure 79 Time domain strain signal

5.2.3. DIC

The signal obtained from the fibre-optic sensor and telemetry systems are already time domain signals and ready to be processed. However, the DIC requires a bit of further processing before the signal is ready in the same way to be processed. Since the DIC measures marker location across the entire shaft, it has the advantage of having data over a wide range of area of the rotor unlike the fibre-optic sensor and strain gauge which only measure at specific locations. It is likely that not all the markers will have been captured in all the images since they are not distributed in a perfectly straight line. As seen in Figure 80 below, it shows that for this specific image not all the markers were captured even though it may be seen by the camera. This could make the collection of data difficult as it would require manual sifting through the images to find proper images, a process which is not ideal.

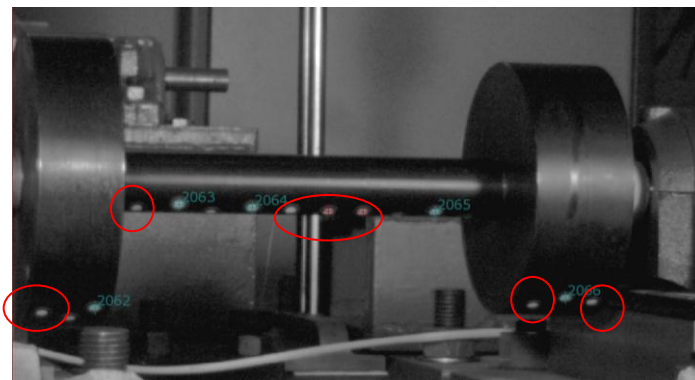


Figure 80 DIC image where some markers are picked up while others are not

In order to counter this problem, the rotor is divided into two components. These are not actually two separate components but just software means of identifying the whole setup better. In this case the rotor is split into a left and right component. Each component is defined by the orientation of the markers within it. When doing this, a number of markers are set as “identification points” and when at least 3 of these points are visible, the entire rotor section may be defined. This means that even though some markers might not be visible, the orientation of a component will still be known based on the few that are visible. The Figure 81 below shows where the rotor is divided. The rotor could only be divided into two components since a sufficient amount of markers per component is required. If more markers were added to the setup, it would be good for defining more components but it is not recommended since the markers would tend to be cramped together and it would be hard for the camera to pick them up. The division may be seen in Figure 107 below.

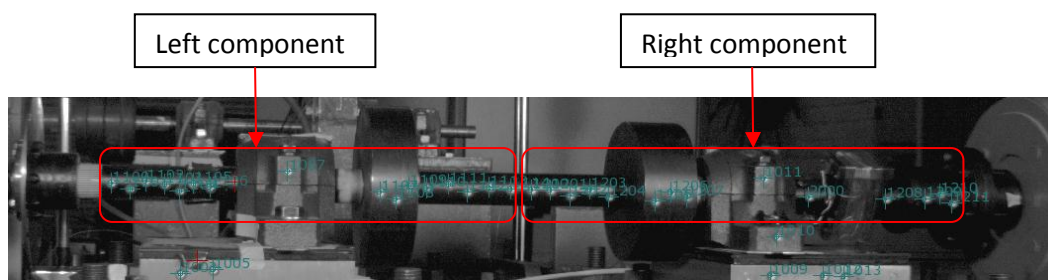


Figure 81 Distinction between left and right components

The 3D image that is created as a result of the combination of the left and right camera is seen in the figure below. These figures also reveal the left, right and relative orientation of the shaft. Figure 82 shows the reference state and its orientation is zeroed. Figure 83 is that of an image taken during a run. Since it has been moved from its initial state, the boxes contain translation and rotation information. For this study, the roll angle is of interest.

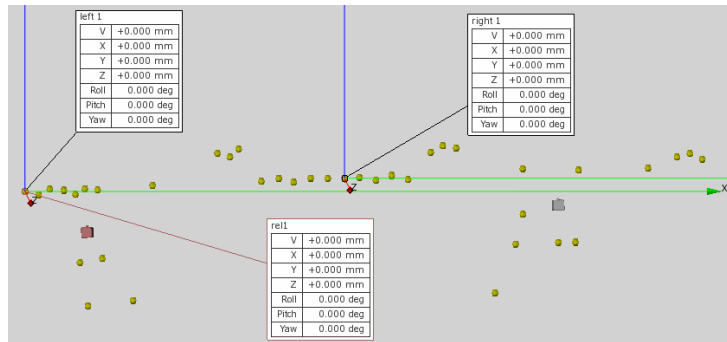


Figure 82 DIC 3D image of the reference state

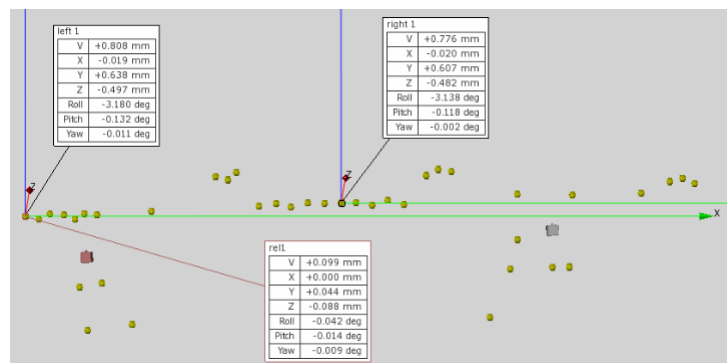


Figure 83 DIC 3D image of an image during running

Now that the orientation angles may be obtained since the left and right components are defined, a new challenge arises. As the shaft rotates, there is a brief time through each rotation where the markers would be on the wrong side of the shaft resulting in images being where no markers are present. It would be incorrect to simply mirror the results as this is not what is occurring and one does not have the vibration detail of this. It would also be incorrect to simply ignore those images as this would corrupt the time signal and mean a completely incorrect frequency analysis. It was decided to simply assume a constant angle value during the back rotation section. This ensured that the time signal would still be continuous and also that no additional frequency content be inserted since it would be a constant value. The figure below shows the time domain signal of this.

It must be remembered that the DIC system undersamples the data and each data point represents an image taken every 2 or 3 revolutions plus a Δt time increment. Now that the entire signal is in a good time domain format, frequency domain analysis could be carried out. Another important note that was mentioned earlier is that the run-up test will not be done using the DIC method since it would result in random images being taken at different speeds and would not yield decent results. Therefore the tests were only carried out using

the constant speed runs. Figure 85 shows the averaged plot of the 18.43 Hz test. As seen before, there are peaks at regular intervals which suggest rotational frequency and its harmonics.

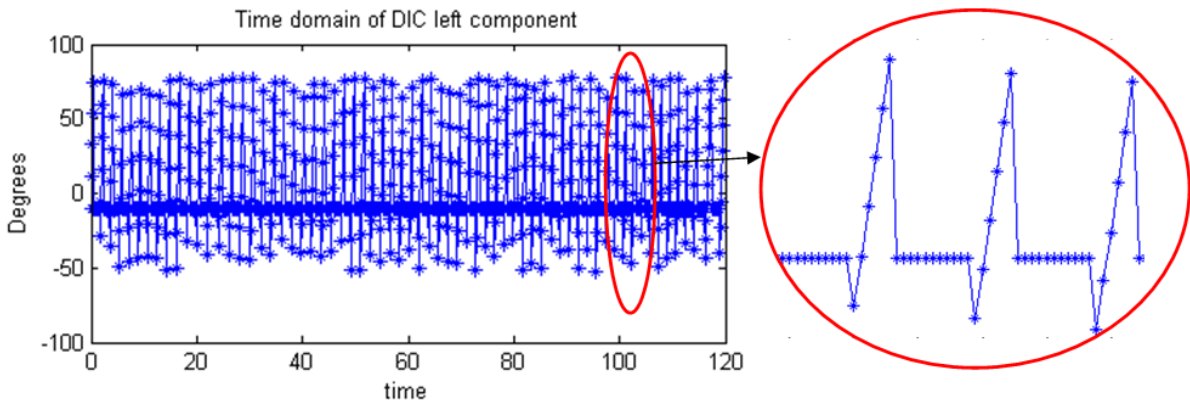


Figure 84 DIC time domain signal

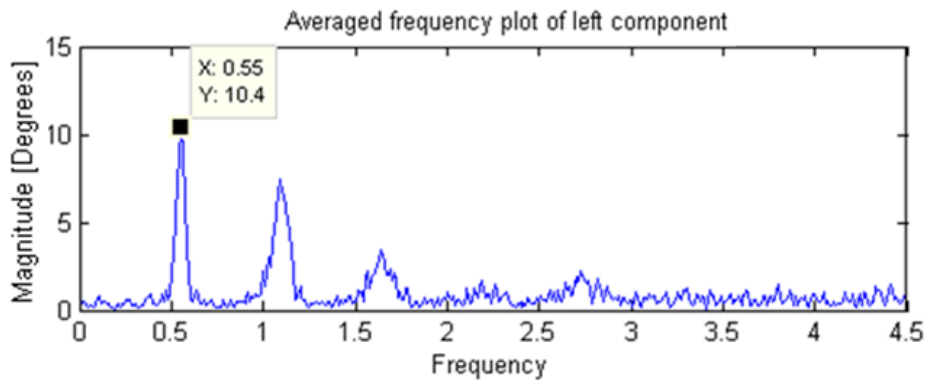


Figure 85 FFT of the undersampled DIC signal

In order to understand the undersampled results better, the fan-paper method must be applied. The figure below shows a colour coded folded paper that must be used for undersampling. Indicating the sampling frequency means that f_s and $f_s/2$ are known and stated in the table. The green folds indicate that the signal may be viewed as is. The red fold indicates areas which fall on a reverse fold and therefore the signal must be reversed in order to understand it properly. All the measuring equipment recorded data simultaneously. The operation speed may therefore be obtained from the fibre-optic sensor result in Figure 68 which shows 18.43 Hz. According to the fan-paper, this frequency lies on a green fold. Within that fold it is represented by 0.43 Hz.

1	2	3	4	5	6	7	8	9	10	11	12	13	14	15	16	17	18	19	20	21	22	23	24	25	26	27	28
4.5	9.0	13.5	18.0	22.5	27.0	31.5	36.0	40.5	45.0	49.5	54.0	58.5	63.0	67.5	72.0	76.5	81.0	85.5	90.0	94.5	99.0	103.5	108.0	112.5	117.0	121.5	126.0

Figure 86 Fan-paper representation of location of undersampled frequencies

Figure 85 above shows the 2D frequency plot of the test run. The first peak appears at 0.55 Hz which according to the undersampling is close to the rotational frequency with a difference of 0.12 Hz. Similarly it is seen that the next peaks are the harmonics of this frequency which appear at 1.1 Hz, 1.65 Hz and 2.2 Hz. The torsional frequency of 120.6 Hz,

according to Figure 86, is meant to appear at 3.6 Hz. A detailed view shown in Figure 87 shows a slight peak in this region but it is not very distinct. It occurs in a region where the surrounding content has similar magnitude and is difficult to isolate it.

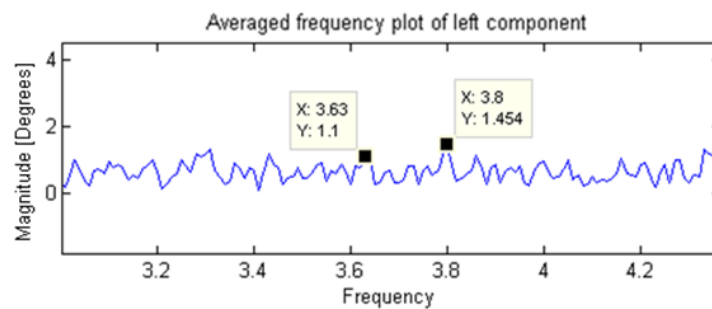


Figure 87 Zoomed in plot on area of interest for natural frequency

Further investigations were done at the higher speed run. This may be seen in Figure 88 below. Using Figure 86 again and realising that the new operating frequency is 27.5 Hz, it may be seen that the peaks at 0.49 Hz, 1.01 Hz and 1.5 Hz are the rotational and harmonic frequencies. The rotational frequency is much closer to what it should be according to Figure 88, which is 0.51 Hz. However, the result is still not conclusive as seen in Figure 88 below.

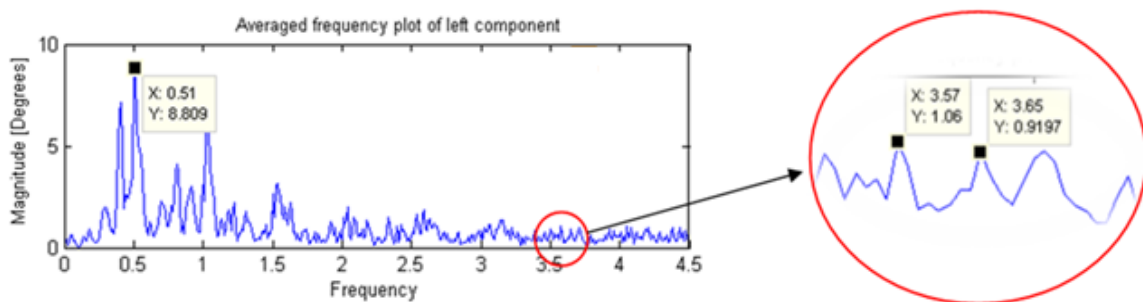


Figure 88 High speed DIC test run

The DIC system measures rotational displacement vibration much like the fibre-optic sensor. The fibre-optic sensor looks at volt pulses representing angle change whereas the DIC does the same thing but measures the actual angle values. It was therefore decided to undersample the fibre-optic sensor signal at the same rate as the DIC system. Figure 89 is the frequency content of this undersampled time signal. The approach applied is the same as that done for the DIC. The undersampled signal was divided into equal increments and from there an averaged frequency plot is obtained. By using the fan-paper method the frequency content may be analysed. A similar figure as found with the DIC system is obtained whereby the operating frequency and its harmonics are visible. The expected torsional frequency of 120.6 Hz should be at 3.6 Hz and there seems to be something present in that region.

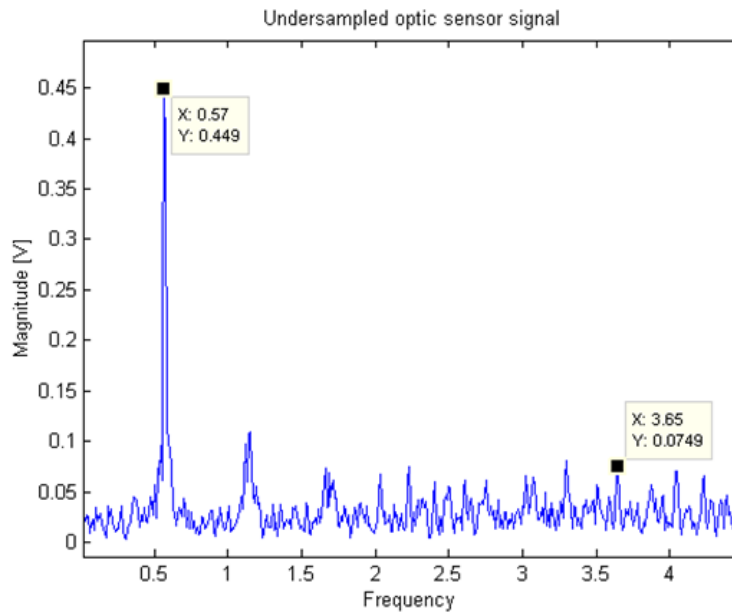


Figure 89 Undersampled frequency plot of optic signal

By doing this to the order removed signal, it is found that there exists some sort of peak at 3.6 Hz. Figure 90 shows the order removed frequency plot signal. But, it is also clear that this peak is not the most distinct and one needs to know where to look in order to make it have any meaning. By simply looking at this, it is not conclusive whether it represents anything in particular and similar tests need to be applied to the damaged case and seen if this peak changes accordingly.

As seen in the literature, the DIC is commonly used for its capability of developing full strain field plots of an object. However it was found out that this DIC system has a base strain sensitivity of $150 \mu\epsilon$ meaning that strain lower than this would not result in decent results. As was seen with the strain results, the strain is quite low and it did not make sense to investigate the DIC results in a strain format and only the angular displacement and the frequency content of that was looked at.

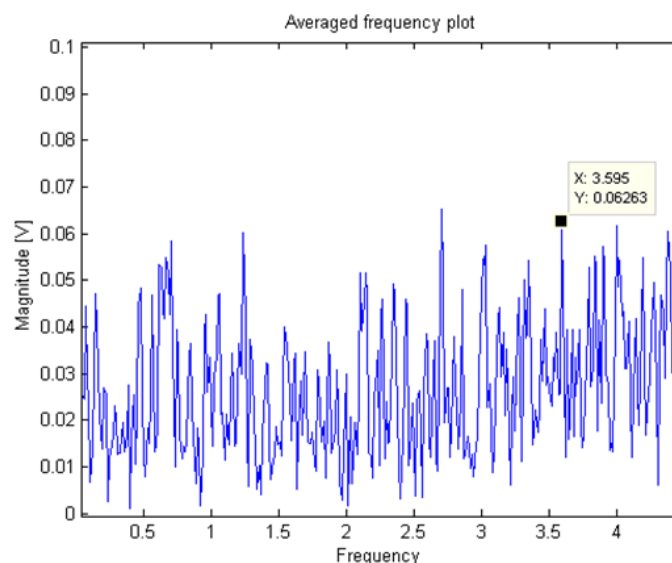


Figure 90 Undersampled frequency plot of optic signal

5.3. Remarks

Based on the above post-processing and observations of the initial results, the following comments and remarks can be made before looking at the final results:

- The fibre-optic sensor clearly identifies a torsional natural frequency at 120.6 Hz during runup tests as well as constant speed runs which one of the main goals of this study.
- This is seen moderately in the normal frequency plot and distinctly in the order removed frequency plot.
- The strain result shows operating frequency peaks and its harmonics as well as peaks at multiples of 50 Hz. It is believed that this is electrical noise since it is present before rotation of the shaft occurs which implies it is not a structural dynamic frequency.
- Applying order removal did not help significantly. Some peaks, though not distinct, were identified in the frequency region of interest.
- This could not have been done if the fibre-optic sensor result did not give clues of where to look since the strain runup test did not reveal any isolated structural frequencies.
- These peaks are of low magnitude since there is low strain in the system during operation and would not mean anything unless further investigations with damage are done to see if the dynamics would change.
- The DIC method revealed operating frequencies, though not perfect with actual setup, but close enough considering the signal is undersampled.
- There were no clear indications of natural frequencies, although as seen for the strain case, some sort of peak is present if one knows where to look.
- These cases also require further damage investigation to quantify how meaningful these supposed peaks are.
- The fibre-optic sensor in some ways may be comparable with the DIC and undersampling this signal revealed similar results as the DIC whereby the operating frequencies were present.
- Using undersampling on the order removed fibre-optic sensor signal, a peak was found in the region of interest. However it among other peaks and an informed conclusion of this peak may only be stated once it is studied for damaged cases.

Based on the above points, it gives a guideline of how one is to look at the results in the next chapter. The fibre-optic sensor thus far gives good results while close attention must be given when looking at the strain and DIC results. This chapter has discussed the method in which the results were processed and viewed. The same methods are used for analysing the damaged shaft cases.

6. Chapter 6- Model updating and final results

6.1. Overview

This chapter looks at some model updating that was carried out with the intention of better matching the FEM and experimental results. This is important for model and testing verification and ensures that the dynamics were captured properly. The chapter then takes a look at the final results.

For the FEM updating section, the changes that were made to the original model and how it is expected to change the results are addressed. The results obtained using the post-processing methods discussed in the previous section are viewed and compared to damaged case results. Finally a comparison and discussion is given between the old FEM, the updated FEM and the experimental results.

6.2. Model updating

6.2.1. Parameter modification

As was observed in the experimental results, the first torsional frequency occurs at 120.6 Hz for the undamaged case. This meant a 13 Hz difference from the original FEM results obtained which was 133.02 Hz which is an error of 10.8%. It was decided to update the model in order to verify the results accurately. The major changes that were made to the model were to update the geometry in order to closely represent what the actual setup looked like. Some of the other parameters that were looked at were the material properties and damage modelling.

a) Geometry

The original FEM rotor contained a simple shaft with two disks on it. The actual experimental setup contains this plus a coupling with a brake disk at the free-end and another rigid coupling joint at the motor-end. These components were built in the model. The implications of adding this to the model means that the mass would increase slightly resulting in a drop in the natural frequency. Since all the components are bolted together and to keep the model as simple as possible, it was all treated as one component with the rotor. This assumption is also backed by the fact that these components are made from the same material and would have the same material properties. Figure 91 shows the updated rotor setup with the experimental setup in order to show better similarity.

b) Material properties

The material used for the experimental setup was mild steel. In the initial FEM model a value of 207 GPa was used for the elastic modulus as found in Callister W.D. (2003). In general, there is a very wide range of steel containing similar material properties. Further investigations showed that the elastic modulus ranges from 200-210 GPa. Decreasing this value closer to the 200 GPa bound would lower the frequency and result in a closer match.

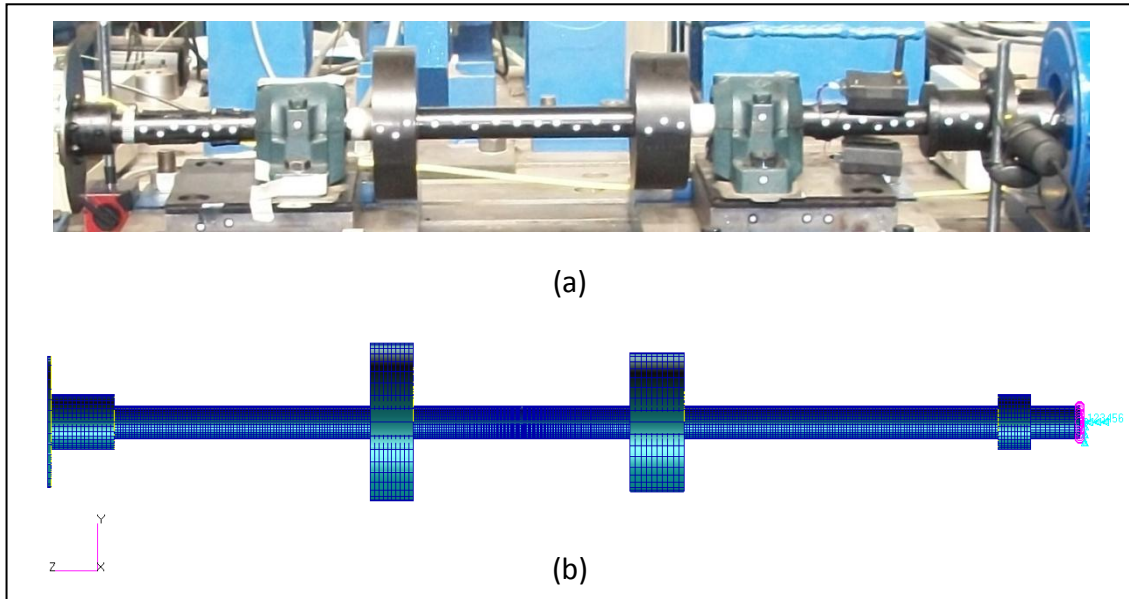


Figure 91 a) Experimental rotor setup, b) Updated FEM model setup

Ideally this process is often done using certain software like FEMtools whereby material updating can be performed on localized individual elements. Since the model was too big for the program, a manual approach was utilised. This involved a sort of trial and error process. Eventually, limited by the 200-210 GPa bounds, 200 GPa was found to best match the results.

c) Damage modelling

Initially the nodes were simply disconnected from each other. After conducting tests and damaging the system, an idea of the geometry of the damage is known and could be modelled to more appropriately match the test setup. In order to conduct this in a proper manner, the mesh at the centre section the rotor was changed to a finer mesh. Even though the model is simple, meshing was a bit more complex and the best way to refine the mesh was to apply this to the entire length of the shaft.

For damage, specific elements, depending on the depth of damage was deleted as shown in Figure 92 a). The width was ensured to be the same as the actual case which was 1.9 mm. A comparison of this may be seen in Figure 92 b).

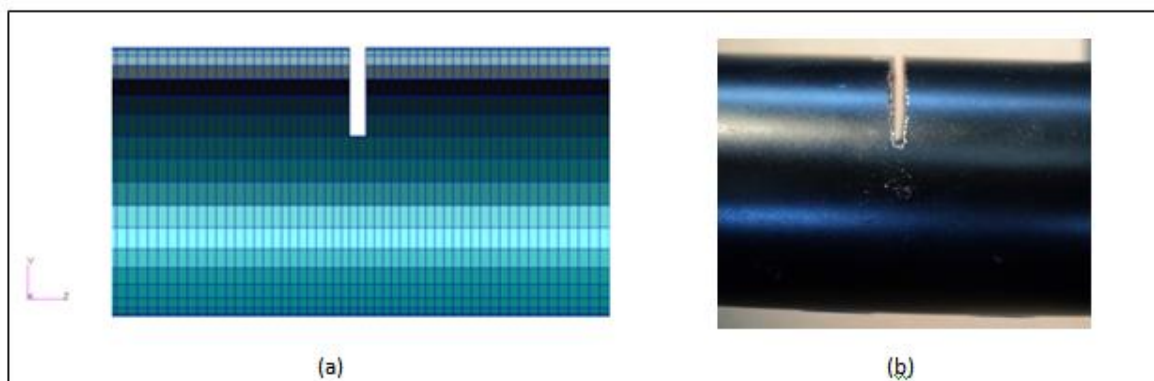


Figure 92 Damage modelling, a) FEM, b) Experimental

6.3. Undamaged comparison of experimental and FEM

Using the above changes, a new analysis was done. This was the same normal modes analysis as before, but with the recent changes implemented. A FEM analysis of this latest model was done and the result of the 1st torsional mode is shown in Table 7 below. A clear decrease in error is evident and verifies the model is in good correlation with the experimental data. The mode shape shown in Figure 92 does not change much but fundamentally still shows the response increasing from the motor-end to the free-end. Since the experimental results only revealed the 1st torsional mode, comparison done with the 2nd mode was not possible.

Table 7 Result comparison between experimental and updated FEM model

Test	Frequency	% Error
Experimental	120.60	-
Initial FEM	133.02	10.30
Updated FEM	121.65	0.87

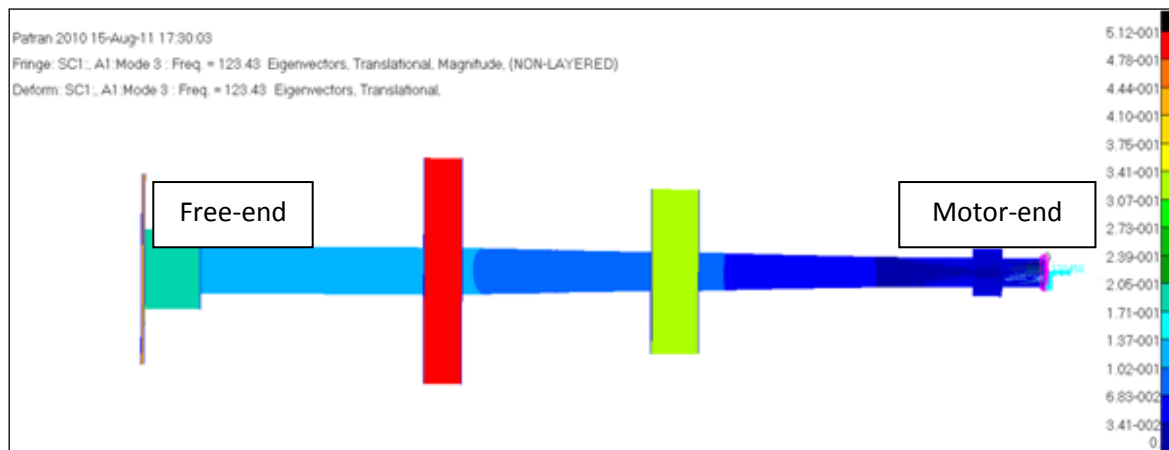


Figure 93 1st torsional mode shape of updated model

6.4. Strain response investigation

As was seen in the experimental testing, the telemetry strain gauge system did not yield ideal results. It did not pick up the dynamics of the system and the strain seemed quite low. An investigation of simulating the rotor was done to obtain the strain response. This was done by carrying out a frequency response analysis. This entailed applying some sort of motor torque load at the motor-end and observing the response.

In order to properly define this torque loadcase, the following input parameters must be addressed:

- The excitation frequency. Since the motor operates from 0-3000 RPM, this represents 0-50 Hz. Therefore the excitation will operate within these frequency limits.
- The input torque. Since the experimental testing was done, an idea of the applied motor torque is known. This was characterised based on the calibration that was

done and the torque voltage values that the motor creates. The torque was found to be 1.725 N.m. Details of this is given in Appendix C.

- Motor BC. The preliminary model had the motor represented by a fixed BC. However, it is not possible to apply any type of load to a node that has a prescribed displacement. This was addressed by modelling the motor as a OD mass or point element. This allowed the rotor to have the same dynamics as before but also allow a motor torque to be applied at the point element.
- Element output. When doing an analysis of this nature, the computation time may be large since responses must be obtained for each of the nodes and elements. Based on the test setup and for practical purposes, a group of specific elements were chosen for their elemental strain response. These elements were at the locations of where the experimental strain gauges were mounted.
- Method of torque application. A torsional frequency response analysis requires an excitation torque being applied to the system. The interesting thing about solid elements in Patran is that it only perceives 3 translation DOFs and no rotational DOFs. This therefore means that a torque cannot directly be applied to a node since solid elements do not allow rotational inputs at their nodes (ESTEQ, 2006).
- In order to counter this problem, an MPC (multiple point constraint) must be created. This is a single node to which the load will be applied and to which other nodes will be dependent upon. The dependent nodes are all those nodes to which the torque must actually be applied to. The torque loading may now be applied directly to this single node which will then transfer it as a rotational excitation to the rotor.

The above mentioned torque load, MPC connection, output elements and point element may all be seen in Figure 94 and 95 below. Label A shows the area of the chosen elements to be monitored. Labels B and C represent the dependent and independent nodes of the MPC respectively. The OD mass element is seen as a triangular element with the torque load applied to it at D.

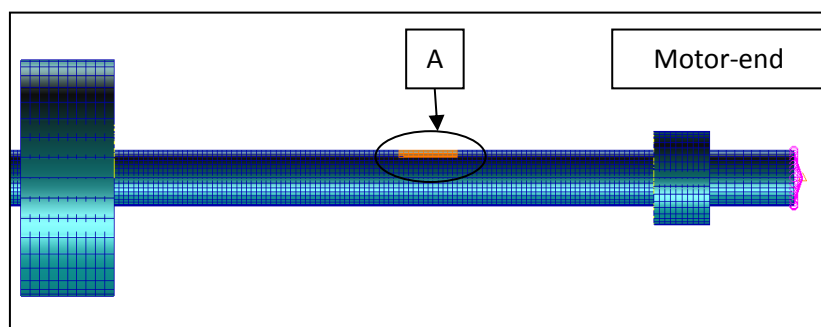


Figure 94 Selected elements to be measured

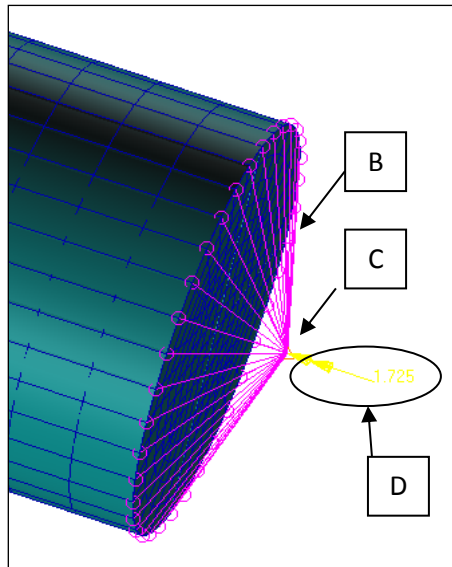


Figure 95 Detail of MPC, motor-element and torque load at motor-end

The 1.725 N.m torque was applied at the OD element with the response recorded at the specific elements. Figure 96 below shows the strain response in the frequency domain. As can be seen the order of magnitude of the strain produced at the natural frequency is extremely small. This explains why the experimental results could not measure the resonant frequency under normal constant operating conditions using strain methods.

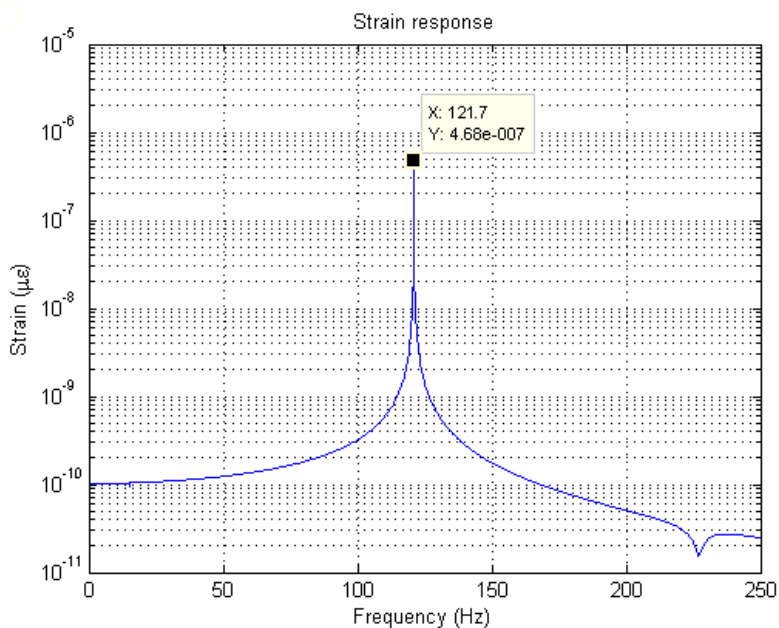


Figure 96 Strain response as a result of motor torque

It is thus interesting to investigate under what conditions the strain response would be detected. Further investigations were done so as to determine this. It was seen in section 5.2.2 that with a strain magnitude of 10 µε, the FFT plot revealed the operating frequency. The current settings for the telemetry system used a gain setting of ±500 µε. According to the system, a worst case error of 0.1% results in a response being correct to 1 µε. This also

shows that the $10 \mu\epsilon$ magnitude of the operating frequency is high and therefore resulted in good visibility in the FFT plot. Thus a lower limit of $2 \mu\epsilon$ would be used. The strain response is related to the applied torque and therefore a torque load of a single order of magnitude higher revealed a response of an order of magnitude greater as seen in Figure 97. This shows a linear relation and therefore a torsional strain response of $2\mu\epsilon$ would be obtained with torque input of 7.37 N.m

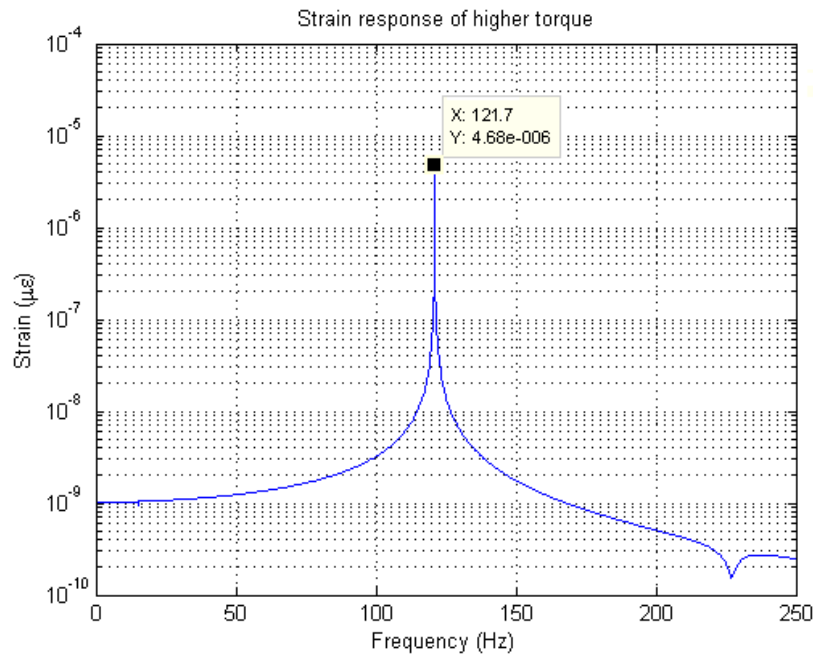


Figure 97 Strain response from a higher torque load

Another investigation was attempted whereby an excitation torque was applied at the free-end of the rotor. This was done in a similar manner in which the motor load was applied to the motor-end. A torque needed to be chosen such that the response of the systems torsional frequency would be of the $2\mu\epsilon$ magnitude. It was found that a 0.37 mN.m resulted in approximately $2 \mu\epsilon$. This is rather small and one would need an extremely sensitive force transducer to achieve this. Since the main purpose was to excite the system in any way as to obtain a good torsional response, a 1 N.m torque was applied and may be seen in Figure 98 below.

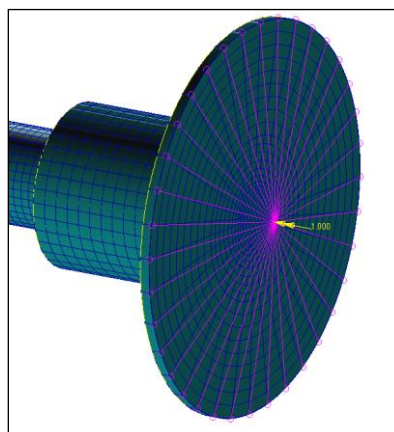


Figure 98 Excitation torque load applied at free-end

The result of this is seen in Figure 99. It can clearly be seen that this increased the response of the strain to around 5300 $\mu\epsilon$ magnitude which could result in experimental testing revealing the natural frequencies using strain methods. It must be noted however, this approach was merely a possible solution of the problem to obtain better results. This dissertation investigates the use of various measurement techniques under normal constant operating conditions whereby no external load is applied and therefore experimental excitation measurements were not carried out.

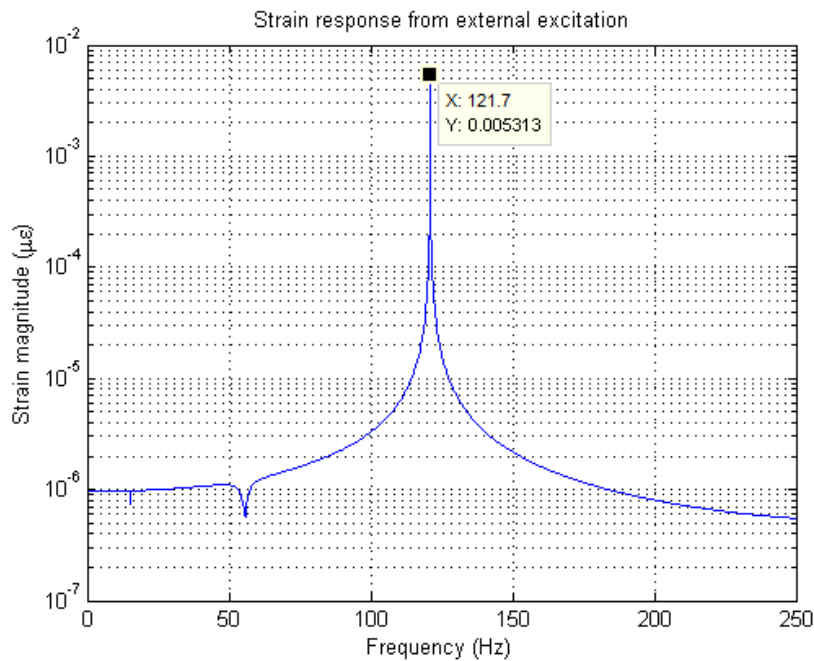


Figure 99 Strain response from external excitation

6.5. Conclusion of updated FEM

The initial FEM model was updated in order to achieve a closer correlation with the experimental results. The geometry, material properties and damage modelling was where major changes were made. The results showed better comparison between the updated model and the experimental testing with an error of less than 1% achieved for the undamaged case. From this it can confidently be stated that the current modelling method provided good comparison with the experimental setup. Using the damage modelling method above, further simulations was done and these results are viewed in the next section where they are plotted with the experimental findings.

Further investigations about the experimental strain responses obtain were done. Applying the motor torque of 1.725 N.m showed that this resulted in an extremely low strain response and explained why the experimental results contained nothing about structural frequencies. Further investigations showed that at the least a resonant strain response of 2 $\mu\epsilon$ is required and could be obtained but a motor torque of 4.23 times higher than the current torque or an external loading at the free-end is required.

6.6. Final Results

6.6.1. Fibre-optic sensor

The fibre-optic sensor yielded the best results in that the dynamic torsional frequency of the system was obtained. By following through with the post-processing and applying this to the damaged case analysis, the changes in frequency could be evaluated. Figure 100 below shows a plot of the torsional frequency against the depth of damage compared to the FEM analysis. It is clearly seen that the torsional frequency at 120.6 Hz gradually decreases which is expected since the stiffness of the shaft is decreasing.

Even though the FEM matched the experimental quite closely, it was still not the exact value and therefore plotting them on the same graph as done does not give the best option of comparison. Instead, the ratios of the frequencies were plotted. This essentially means that the change in frequency as a result of depth of damage can be compared and gives a better representation that damage is detected of the correct magnitude in each case. This may be seen in Figure 101. It is seen that with the effect of damage the ratio matches closely for small crack depth and matches to a lesser amount at higher damage. The actual consequence of this may be seen when plotting the error between the experimental and FEM as a function of crack depth percentage.

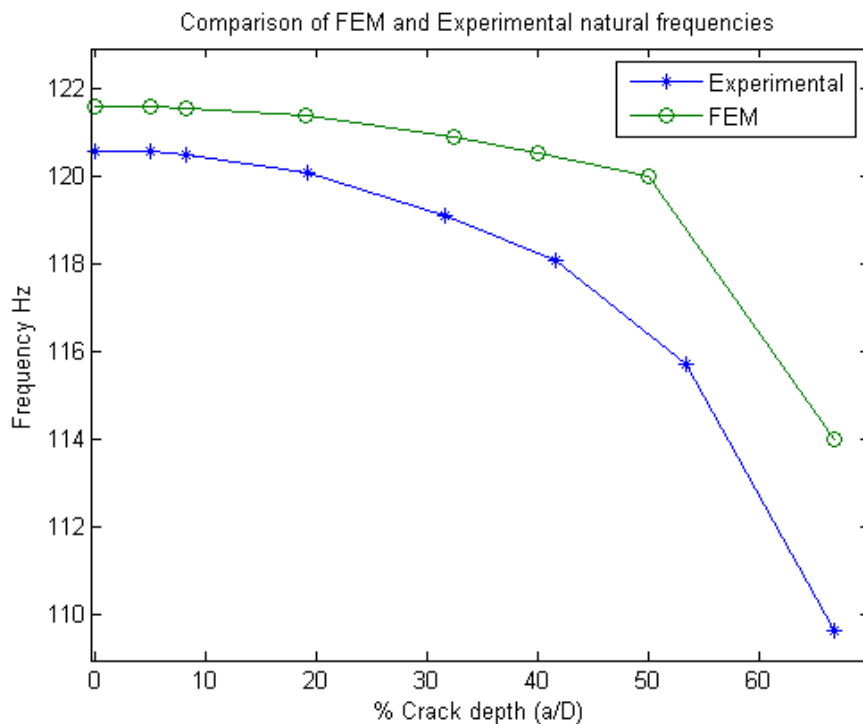


Figure 100 Frequency variation as a function of damage

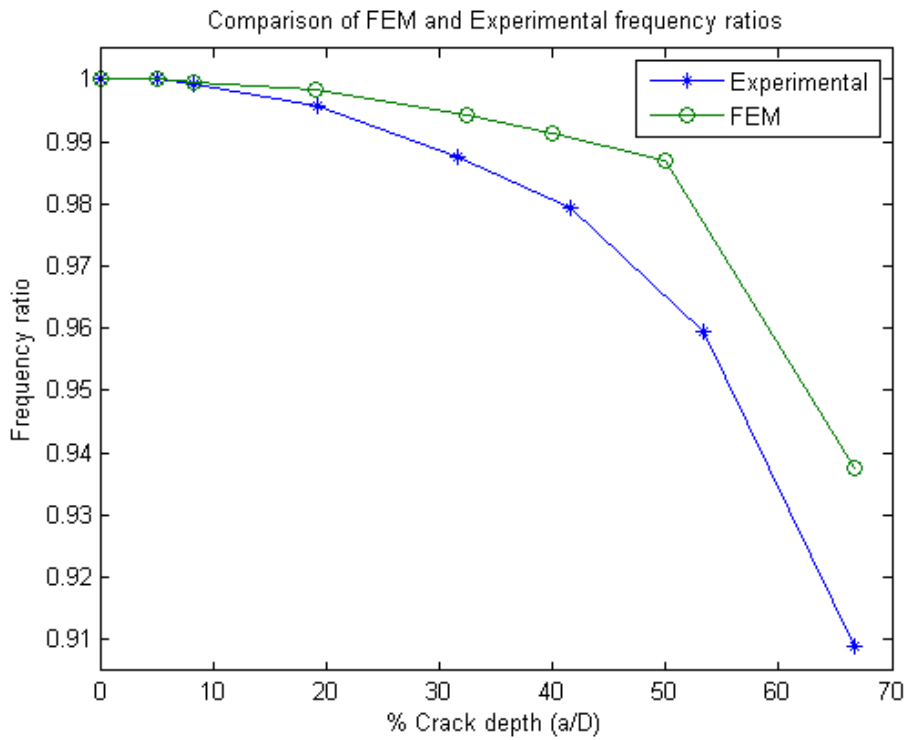


Figure 101 Frequency ratio comparison

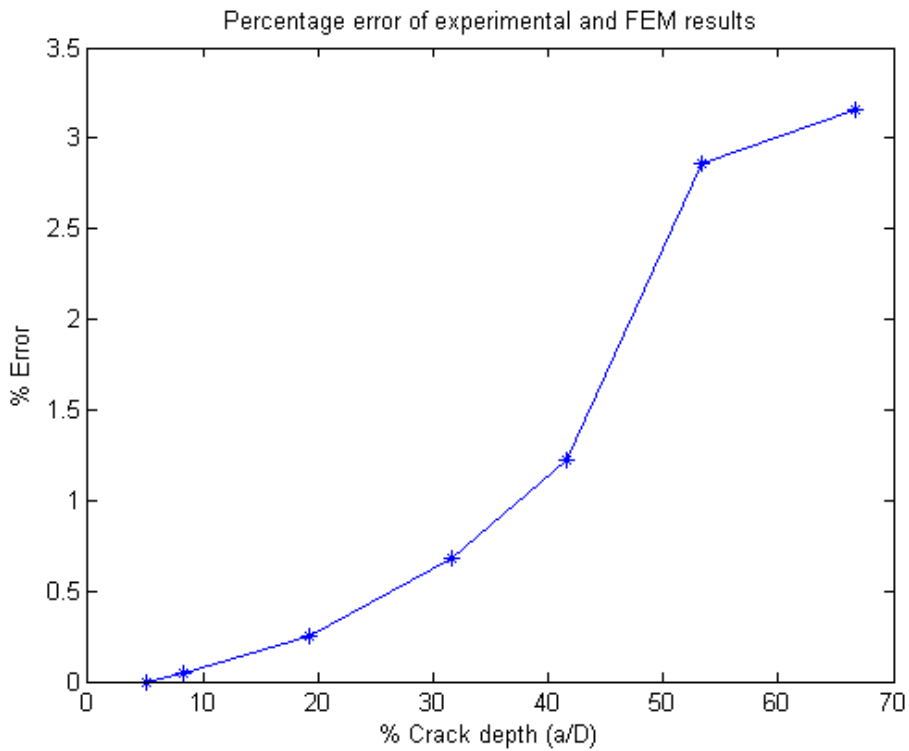


Figure 102 Percentage error between Experimental and FEM results

Figure 102 shows the error, and it is seen that a maximum error of 3.16% is obtained. This is quite a low error and it can be said with confidence that the experimental results were verified with the FEM model within approximately 3% error.

The FFTs of the damaged cases was then plotted on the same figure as a comparison of the change when viewing in the frequency domain. Figure 103 shows this for a few of the damage runs since putting all these tests in one would look a bit cluttered.

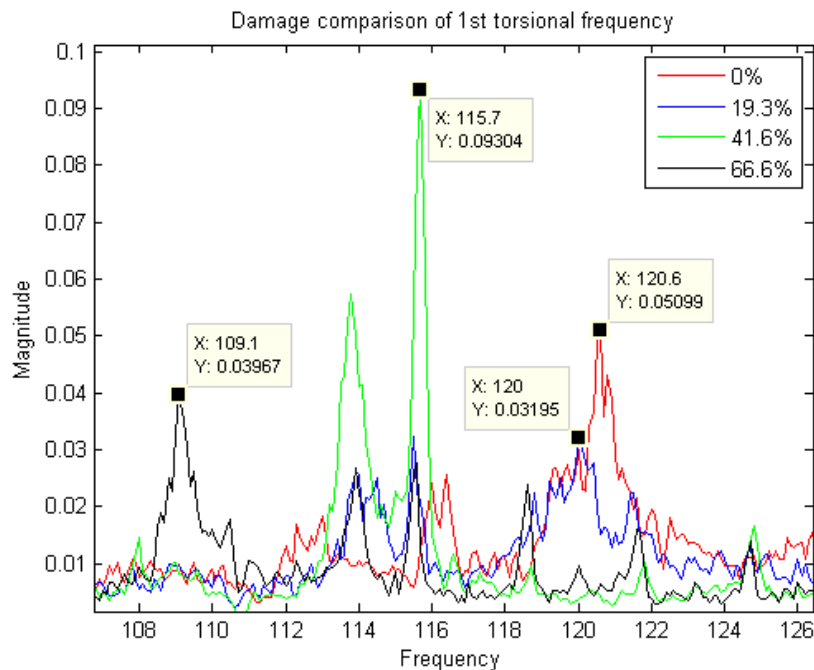


Figure 103 FFT comparison of undamaged and damaged cases for optic sensor

From these results, it may be concluded that the fibre-optic sensor successfully monitored and detected damage of a rotor under transient conditions of runup tests but more importantly under constant speed running conditions.

6.6.2. Telemetry system

From the investigations and analyses done on the strain results, it is clear that the telemetry strain gauge system did not yield the results that were sought after. It is not entirely strange that the fibre-optic sensor gives useful results while the strain gauge does not since they measure different parameters. As was seen in the strain response analysis in section 6.4, the operating conditions resulted in low torsional strain responses. Therefore the strain results are not usable.

Nonetheless, Figure 104 shows a comparison as was done for the fibre-optic sensor. This was done mainly to see if any changes might have occurred. From this it is seen that nothing distinctive may be concluded. The peaks that are visible do not change or correlate with the fibre-optic sensors and as a result shows that the strain gauge method does not achieve the goals of damage monitoring.

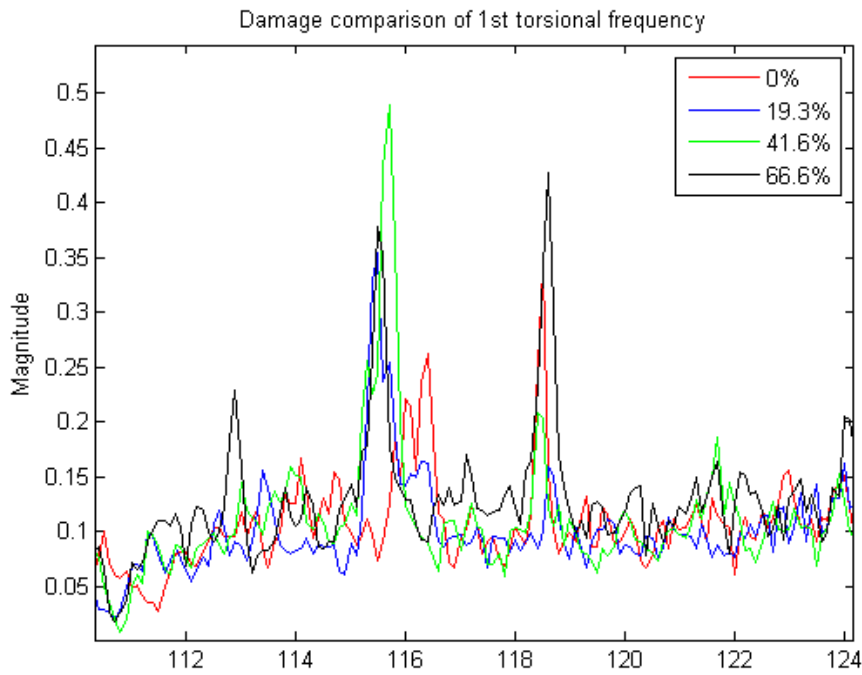


Figure 104 FFT comparison of undamaged and damages cases for strain gauges

6.6.3. DIC

The DIC results using undersampling methods also did not reveal very promising results as was seen earlier. But as done with the strain sensor, investigations for damaged cases were looked at in any case. Using the available information from the fibre-optic sensor, an idea of where the damaged natural frequencies would lie is known. Using Figure 86 shown earlier of the fan-paper method, these frequencies may be converted into the base-band range. This is presented in Table 8 below.

Table 8 Conversion of damaged frequencies to base-band frequency of undersampled methods

Damage %	Actual frequency (Hz)	Base-band conversion frequency (Hz)
0	120.6	3.6
5	120.6	3.6
8.3	120.5	3.5
19.3	120.1	3.1
31.6	118.9	1.9
41.6	118.1	1.1
53.3	115.7	1.3*
66.6	109.1	1.6

*This specific range of frequencies may be seen in Figure 105 below. As can be seen, the 115.7 Hz falls in the red fold representing that the base-band needs to be reversed and for this reason falls at 1.3 Hz.

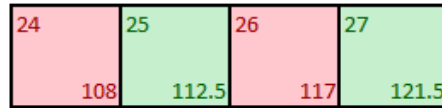


Figure 105 Frequency section of reversed frequency base-band

However as was seen in the previous chapter, the results did not reveal any specific natural frequency peaks that were of interest other than operating frequencies and harmonics. This was a similar case as damage was increased. Since all the frequencies are in different locations in the base-band, it does not make practical sense to view it in one graph because as seen in Table 8, 66.6% damage would lie at a higher base-band than the 53.3% and 41.6%. But since damage could not be detected at all, it renders this testing method not usable.

As was seen, when the good fibre-optic signal was undersampled with its orders removed, it revealed some information about natural frequencies. This therefore suggests that using the fibre-optic sensor might result in some good information for damaged case. This can only be concluded once it is tested.

6.6.4. Further undersampling investigation

The results above and in the previous chapter clearly shows that the DIC system is not ideal for damage detection using undersampling techniques. This is somewhat not surprising and surprising at the same time. The surprising part is that for a simple analytical example done in chapter 2; this method was carried out successfully. It clearly found the operating 10 Hz as well as the other 80Hz signal in its base-band frequency range. Obviously it is an ideal situation with no major effect of operating conditions noise and other external effects. But fundamentally this method should work provided the conditions are good with an ideal signal.

It is unsurprising since, undersampling techniques have not always been followed or investigated when it comes to measuring dynamics of a structure. The Nyquist theorem states that the sampling rate needs to be at least twice the frequency of interest. The application of undersampling methods was capitalised on since it is still a periodic signal and useful results could be obtained as was done by Vanlanduit et al. (2009). The problem however, came from the fact that not enough strain existed in the system. The strain gauge is more sensitive than the DIC system, and even it had not displayed results. Therefore it is not surprising that the DIC system had not revealed any conclusive results either.

To investigate this fact further, it was decided to apply the undersampling frequency to the fibre-optic sensor signal as mentioned in the previous chapter. These tests were done on all the damaged cases. The undersampled base-band results found in Table 8 must be looked at for in the fibre-optic sensor results as well. As mentioned before, it would not make practical sense to compare them on a single graph. Therefore each of them is plotted individually as shown in Figure 106. It is found that undersampling the fibre-optic sensor had revealed the expected change in the base-band frequency range.

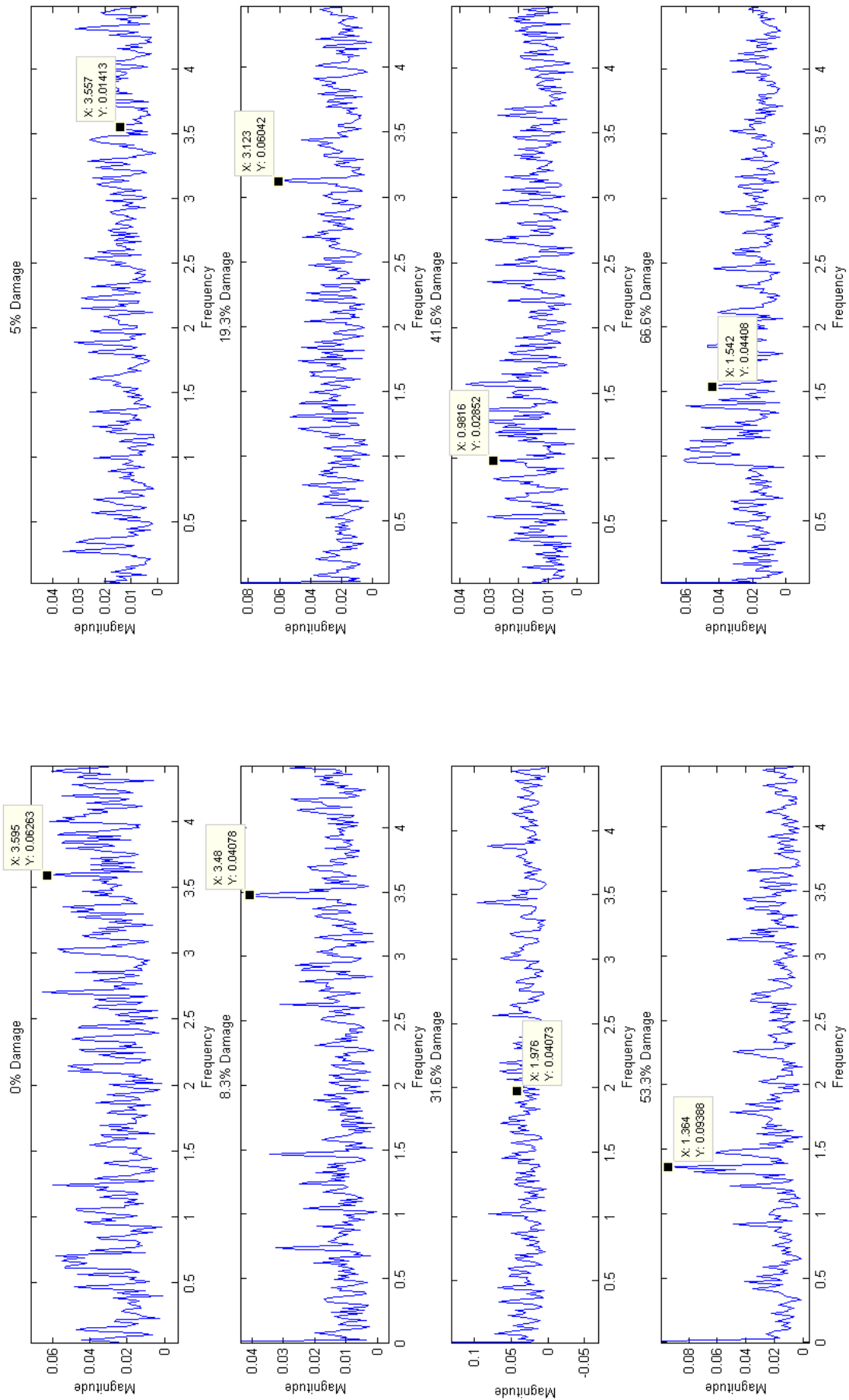


Figure 106 Subplots of each damage case in the base-band range showing peaks representing torsional frequencies

Table 9 summarises the peaks obtained and compares them to the as expected peaks of the actual frequency representation. Although the values are not exactly as expected, it must be remembered that the signal was undersampled which would alter the results slightly. This is affected due to the resolution not being the same as before as mentioned in chapter 2.2. A resolution of 0.1 Hz was used for the fibre-optic sensor and revealed good graphical content. For the DIC system, the signal was not dependent on the sampling frequency as was done in the example. Here the FFT size could be chosen. A low number of FFT points would result in unclear plots whereas a high number of points would make the result very noisy. A good balance is essential for decent plots. An FFT size of 900 points was chosen and resulted in a resolution of 0.01 Hz. For this reason, Table 9 below shows the undersampled data at second decimal place and showing slight deviations from the base-band equivalent.

Table 9 Representation of undersampled frequencies obtained

Damage %	Actual frequency	Base-band equivalent	Undersampled data
0	120.6	3.6	3.59
5	120.6	3.6	3.55
8.3	120.5	3.5	3.48
19.3	120.1	3.1	3.12
31.6	119.1	2.1	2.13
41.6	118.1	1.1	0.98
53.3	115.7	1.3	1.36
66.6	109.1	1.6	1.13

This result shows that undersampling methods may be applied for damage detection. However, it was obtained by undersampling a signal that was known to give good results. The DIC systems results were based solely on the undersampled data and no other information.

6.7. Conclusion of results

The results have been critically analysed, and the following may be concluded:

- Fibre-optic sensor picked a structural frequency during runup tests
- This was further witnessed during normal constant running conditions with high magnitude order content.
- Order removal process was successfully implemented and lead to better viewing of the natural frequency content.
- Fibre-optic sensor was able to detect damage and a change in the first torsional natural frequency was noted with a 9% change in frequency for 66.6% damage.
- These matched the FEM results quite accurately with a 0.87% error for the undamaged case and a 3.2% error for the largest damage case.
- The strain gauge and the DIC methods did not reveal any distinct structural frequencies during runup or constant run tests.

- The strain gauge had picked up operating speeds but was also filled with electrical frequencies of 50Hz and harmonics of this.
- Even in the damage case, there were no detectable changes in the frequency content relating to damage.
- Further FEM analysis showed that the strain response was too low and that higher motor speeds or external excitation could remedy the problem.
- Using undersampling it was apparent that it was able to obtain operating frequencies and harmonics.
- No clear distinct peaks in terms of the natural frequency could be seen.
- Applying undersampling to the fibre-optic sensor revealed changes in natural frequencies as viewed in the base-band.
- This therefore indicates that undersampling would work in certain cases

7. Chapter 7- Conclusions and Recommendations

7.1. Conclusion

The purpose of this study was to investigate the changes in the dynamics of a rotor setup under constant operating conditions. Specifically in the investigation, the focus was placed on analysing the torsional vibration and the torsional dynamic changes as a result of damage being present. The torsional measurement equipment of interest in this study was the fibre optic sensor, telemetry strain gauges and the digital image correlation system. As many researchers have investigated torsional dynamics using various techniques, there had been no study in the comparison of which method proves to be most ideal and advantageous for damage detection. These specific techniques used covers signals from analog in the form of the strain gauge, to digital discrete signals in the form of the fibre-optic sensor and photogrammetry. One of the aims of this dissertation was to answer this question as well as understand and investigate the use of undersampling for measurement techniques. The whole project has been carried out by doing a numerical and experimental analysis.

The FEM analysis was carried out using the Patran finite element software and solved using the Nastran solver. Initial modal analysis revealed that a torsional frequency was present at 133.02 Hz. Damage was inserted by simply not connecting the nodes at specific locations. This proved to be a successful method that had been used in the past. The results showed a decrease in frequency with increasing damage size. Once the experimental testing had been completed, the model could be updated based on the results obtained. By updating the geometry of the setup, the analysis results matched the experimental result much closer with an error of 0.87% for the undamaged case. It may be concluded that the model built and updated was successful in carrying out an initial test and to test sensitivity of different parameters.

For the experimental testing, the rotor was manufactured and testing using three different types of measuring equipment had been conducted. The fibre-optic sensor, which measured square waves from the black and white coded tape, contained information about torsional vibration hidden in the width variations of the square wave pulses. The frequency content of this result revealed high magnitude operating frequency content with its harmonics. Torsional dynamics of the system was found hidden amongst these high peaks. An order removal technique was successfully carried out and the torsional frequency could be viewed much better. A change in this frequency was also observed once damage was inserted. This proved that the fibre-optic sensor successfully monitored and detected damage in the rotor during constant operation.

The strain gauge system was mounted onto the shaft and used telemetry system to send the signal to the analyser. The frequency domain content revealed operating frequencies but nothing about the structural dynamics of the rotor. By further investigating the time domain data, it was seen that the strain had information about the operating frequency but the dynamics was too low. Based on this, it may be stated that under normal constant speed

operation, not enough natural excitation was present in the system in order to obtain high enough torsional strain for the strain gauge to pick up. It is therefore concluded that the strain gauge did not successfully detect a torsional mode and hence damage during normal operation.

The DIC system used undersampling techniques to record the data. By doing this, the frequency content needed to be analysed and converted to the fan-paper base-band domain in order to understand the content better. This proved to be successful as the operating frequency content and its harmonics were observed. However, the dynamics of the system were not obtained and therefore damage could not be detected using this method. But, because some of the order content was visible, it proved that undersampling was able to gather some sort of information.

The fibre-optic sensor that also measured rotational displacement was undersampled and also revealed operating frequencies and a tiny hint of some structural content. By using the order removed signal, a better view of the dynamics were obtained. For the case of the damaged shaft, changes according to the base-band frequency range were seen. Based on the above conclusions, the following conclusive points may be stated:

- The fibre-optic sensor proved to be the successful torsional measuring equipment for online monitoring and damage detection.
- The strain gauge provided order content but nothing about dynamics which suggests it requires more excitation into the system.
- The DIC also revealed order content which was successfully obtained through undersampling techniques.
- Undersampling was successfully used with the fibre-optic sensor results to obtain changes in the dynamics for a damaged shaft.

7.2. Recommendations and Future work

Since certain methods did not work in this investigation, it does not mean it has to be completely disregarded. Various changes and alterations may be applied in order to counter some of these problems and possibly create new developments for future research explorations. These possible ideas, recommendations and potential future research areas are listed below:

- By creating the crack this way, it allows for various investigations of modelling cracks in FEM software. Comparison study may be done between methods of simply not connecting the nodes, as was done in this study, and modelling contact areas to simulate the breathing mechanism of cracks.
- Strain modal analysis may be investigated by applying external excitation or loading on the system to excite the modes of interest in order to increase the strain response to $2 \mu\epsilon$ for strain gauge systems.

- By creating a setup with a low enough dynamic frequency and having a high enough strobe light available, one can investigate systems without undersampling techniques.
- The DIC system in this study only looked at the markers while they were in camera view. There are methods by which the markers may be studied during the full rotation and thereby giving a better full scale representation of what happens during each revolution. The implementation of such a setup together with the external loading for higher strain could prove useful.
- Once the above methods have been implemented, it would be interesting to apply them on a system with an actual crack. Since the current damage was created by sawing the shaft, future analysis could be done by growing a crack onto the shaft. This is done by cutting a notch into the shaft and then applying 3 point bending loading in order to grow the crack through fatigue and thus representing a proper crack.

The initial objectives and what was learnt from them are listed below:

- Measurement and comparison of results using three torsional techniques was carried out with the fibre-optic sensor proving to be the most suitable under normal constant speed operation
- Undersampling methods for vibration monitoring had been studied and better understanding of its use was gained. It proved successful with the fibre-optic sensor

The secondary objectives were met:

- The numerical analysis was successfully carried out using the Patran software.
- Sensitive areas in the shaft were obtained for different parameters.
- The rotor was measured and tested using three different measuring techniques.
- Frequency content from the results of each method was analysed and the fibre-optic sensor revealed the best result for damage detection.
- The FEM and experimental results showed good correlation.

8. Chapter 8- References

Aspragathos, N. & Dimarogonas, A.D. (1981). Fatigue damage of turbine-generator shafts due to fast reclosing, IEE Proceeding. 129: Part C.

Avitabile P., Niezrecki, C., Helfrick, M., Warren C. & Pingle, P. (2010). Non-contact measurement for model correlation, *Sound and Vibration*, 8-12.

Batchellor, C.R. & Edge, C. (1990). Some recent advances in fibre-optic sensors, *Electronics & Communication Engineering Journal*. 175-184.

Bieryla, D.J., Tretherway, M.W., Lissenden, C.J., Lebold, M.S. & Maynard, K.P. (2005). Shaft crack monitoring via torsional vibration analysis; Part 1- Laboratory tests. Unpublished manuscript.

Binsfeld Engineering Inc. TorqueTrak 10K, Torque Telemetry System, Users Guide.

Bumby, J.R. & Wilson, J.M. (1982). Structural models and undamped torsional natural frequencies of a superconducting turbogenerator rotor, *Journal of Sound and Vibration*, 87(4):589-602.

Callister, W.D. (2003). Material science and engineering An introduction, 6th Edition, John Wiley & Sons Inc.

Cao, J.J., Yang, G.J., Packer, J.A. & Burdekin F.M. (1998). Crack modelling in FE analysis of circular tubular joint, *Engineering Fracture Mechanics*, 61(537-553).

Carboni, M. (2007). Strain-gauge compliance measurements near the crack tip for crack closure evaluation: Applicability and accuracy, *Engineering Fracture Mechanics*, 74:563-577.

Chu, T.C., Ranson, W.F., Sutton, M.A. & Peters, W.H. (1985). Applications of digital-image-correlation techniques to experimental mechanics, *Experimental Mechanics*, 232-244.

Cook, R.D. & Malkus, L. (2002). Concepts and application of finite element analysis, 4th Edition, John Wiley & Sons Inc.

Dimarogonas, A. (1996). Vibration of cracked structure: A state of the art review. *Engineering Fracture Mechanics*, 55(5):831-857.

Dimarogonas, A., & Massouros, G. (1981). Torsional vibration of a shaft with a circumferential crack, *Engineering Fracture Mechanics*, 15(3-4):439-444.

ESTEIQ. (2006). Linear Static, Normal modes and Buckling Analysis using MSC Nastran and MSC Patran, NAS 120 Course notes, May 2006.

GOM. (2010). Optical Measuring techniques, Pontos User information- Hardware.

- Gounaris, G. & Dimarogonas, A. (1988). A finite element of a cracked prismatic beam for structural analysis. *Computers & Structures*, 28(3):309-313.
- Groover, C.L., Trethewey, M.W., Maynard, K.P. & Lebold, M.S. (2005). Removal of order domain content in rotating equipment signals by double resampling, *Mechanical Systems and Signal Processing*, 19:483-500.
- Hameed, Z., Hong, Y.S., Cho, Y.M., Ahn, S.H. & Song, C.K. (2009). Condition monitoring and fault detection of wind turbines and related algorithms: A review, *Renewable & Sustainable Energy Reviews*, 13:1-39
- Helfrick, M.N., Niezrecki, C., Avitabile, P. & Schmidt, P. (2008). 3D Digital image correlation methods for full-field vibration measurement, Proceedings of the 26th International Modal Analysis Conference, held in Orlando, FL, February.
- Helfrick, M.N., Pingle, P., Niezrecki, C. & Avitabile, P. (2009). Optical non-contacting vibration measurement of rotating turbine blades, Proceedings of the 26th International Modal Analysis Conference, held in Orlando, FL, February 9-12.
- Heng, A., Zhang, S., Tan, A.C.C & Mathew, J. (2009). Rotating machinery prognostics: State of the art, challenges and opportunities, *Mechanical System and Signal Processing*, 23:724-739.
- Heyns, P.S. (2008). Digital Analysis Techniques, Vibrations MEV 732 Course note, April 2008.
- Hosking, R.H. (n.d). How to use undersampling, Pentek Inc.
- How strain gauges work, Available from: <http://www.kyowa-ei.co.jp/english/products/gauges/pdf/howsgw.pdf> (Accessed on 18 June 2011).
- Ishida, Y. (2008). Cracked rotors: Industrial machine case histories and nonlinear effects shown by simple Jeffcott rotor, *Mechanical Systems and Signal Processing*, 22:805-817.
- Janssen, W. (n.d), Welding on rotors for power plant turbo sets State of the art, Siemens AG, Power Generation, Germany, Available from: http://www.energy.siemens.com/us/pool/hq/energy-topics/pdfs/en/steam-turbines-power-plants/2_Welding_on_Rotors.pdf (Accessed on 17 October 2011).
- Kim, S. & Lee, J. (2000). Use of modal testing to identify damage on steel members, *KSCE Journal of Civil Engineering*, 4(2)75-82.
- Kobayashi, H. & Nitta, A. (1974). Burst of steam turbine in fossil power plant, *Failure Knowledge Database/100 Selected cases*.
- Kumar, C. & Rastogi, V. (2009). A brief review on dynamics of a cracked rotor, *International Journal of Rotating Machinery*, 2009 Article ID: 758108.

L&K GmbH. (2011). Element types of finite element system MEANS V5, Available from: http://www.fem-infos.com/Element_types/Element_types_of_FEM_system_MEANS.html (Accessed 14 May 2011).

Lall, P., Panchagade, D., Iyengar, D., Shantaram, S., Suhling, J. & Schrier, H. (2007). High speed digital image correlation for transient-shock reliability of electronics. Electronic Components and Technology Conference, 924-939.

Laws, C.W. (1986). A brief history of cracked rotor saves—turbine generators in the U.K. rated 60MW to 660MW (1971–1981), Seminar on Shaft Crack Detection, Bently Rotor Dynamics Co.

Lebold, M.S, Maynard, K.P., Trethewey, M.W., Bieryla, D.J., Lissenden, C.J., Tossot, S.P., Verrier, P. & Metz, J. (2003). Technology development for shaft crack detection in rotating equipment, EPRI International Maintenance Conference, held in Chicago, IL, August 18-20.

Lissenden, C.J., Tissot, S.P., Trethewey, M.W. & Maynard, K.P. (2007). Torsion response of a cracked stainless steel shaft, *Fatigue Fracture Engineering Material Structure*, 30:734-747.

Machorro-Lopez, J.M., Adams, D.E., Gomez-Mancilla, J.C. & Gul, K.A. (2009). Identification of damaged shafts using active sensing—Simulation and experimentation, *Journal of Sound and Vibration*, 327:368-390.

Maynard, K., Trethewey, M., Gill, R. & Resor, B. (2002). Gas turbine blade and disk crack detection using torsional vibration monitoring A feasibility study. Unpublished manuscript.

Maynard, K.P. & Trethewey, M. (2001). Blade and shaft crack detection using torsional vibration measurements Part 2: Resampling to improve effective dynamics range, Applied research laboratory, The Pennsylvania State University, Unpublished manuscript.

Maynard, K.P. & Trethewey, M. (1999). On the feasibility of blade crack detection through torsional vibration measurements, Conference proceedings of the 53rd meeting of the Society for Machinery Failure Prevention Technology held in Virginia Beach, April 19-22.

Mguil-Touchal, S., Morestin, F. & Brunet, M. (1997). Various experimental applications of digital image correlation method, Unpublished manuscript.

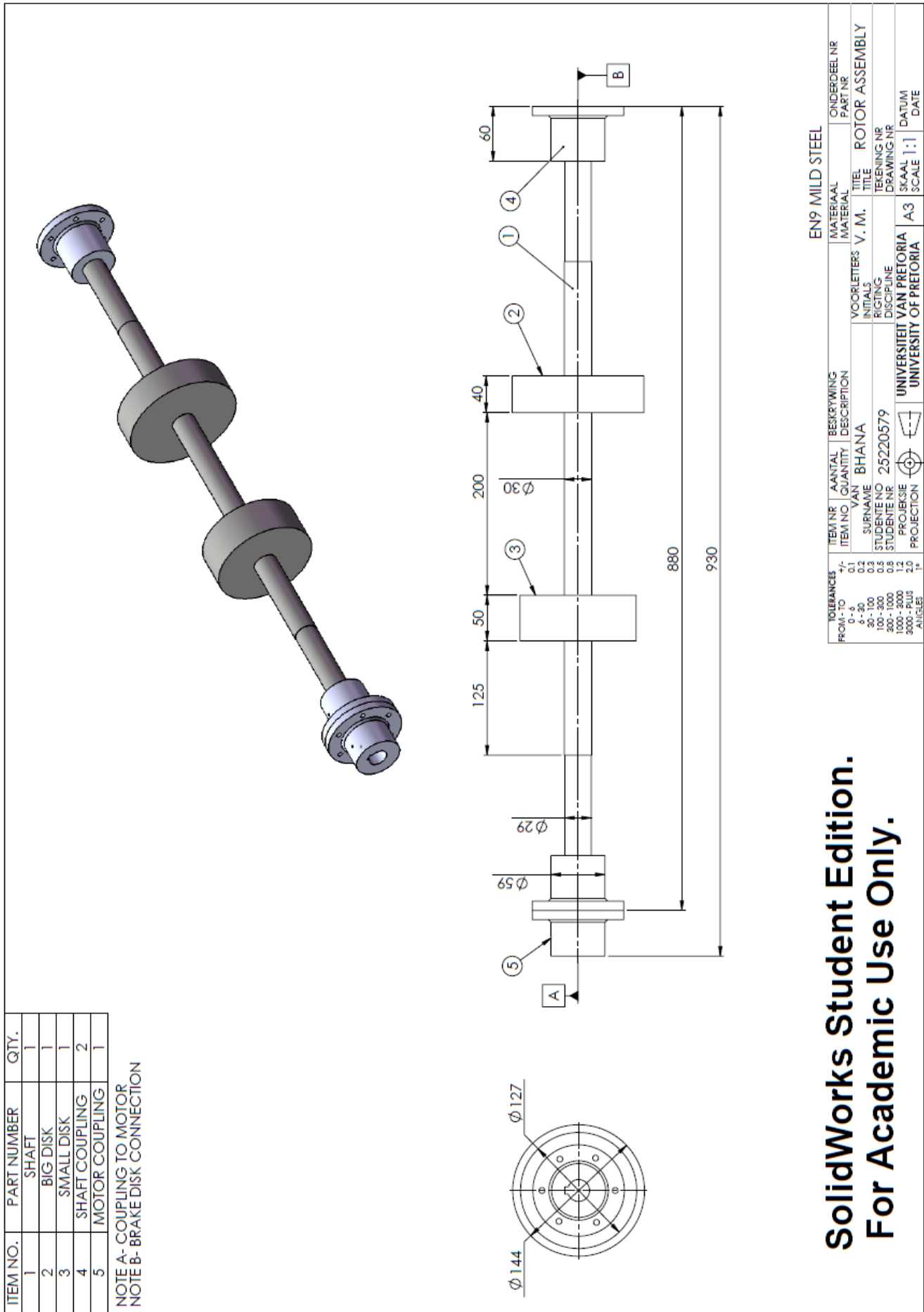
National Instruments. (1998). Strain gauge measurements- A tutorial, Application Note 078.

Papadopoulos, C.A. (1994). Torsional vibrations of rotors with transverse surface cracks, *Computers & Structures*, 51(6):713:718.

Patran's Element Library, Available from: http://www.mscsoftware.com/training_videos/patran/Reverb_help/index.html#page/Finite%2520Element%2520Modeling/elem_lib_topics.16.9.html (Accessed 18 June 2011). Rankin,

- A.W. & Seguin, B.R. (1956). Report of the investigation of the turbine wheel fracture at tanners creek, *Transactions of the ASME* 78(10):1527.
- Raskovic, D. (1949). On some characteristics of the frequency equation of torsional vibrations of light shafts with several disks, Unpublished manuscript.
- Resor, B.R., Trethewey, M.W. & Maynard, K.P. (2005). Compensation for encoder geometry and shaft speed variation in time interval torsional vibration measurement, *Journal of Sound and Vibration*, 286:897-920.
- Sanderson, A.F.P. (1992). The vibration behaviour of a large steam turbine generator during crack propagation through the generator rotor, Proceedings of International Mechanics Conference, p.263.
- Schabtach, C., Fogleman, E.L., Rankin, A.W. & Winne, D.H., (1956). Report of the investigation of two generator rotor fractures, *Transactions of the ASME*, 78(10):1567.
- Sekhar, A.S. & Prabhu, B.S. (1992). Crack detection and vibration characteristics of cracked shafts, *Journal of Sound and Vibration*, 157(2):375-381.
- Sekhar, A.S. & Prasad, P.B. (1997). Dynamic analysis of a rotor system considering a slant crack in the shaft, *Journal of Sound and Vibration*, 208(3):457-474.
- Sekhar, A.S. (1999). Vibration characteristics of a cracked rotor with two open cracks, *Journal of Sound and Vibration*, 223(4):497-512.
- Technology. (2000). Shunt Calibration of strain gauge instrumentation
- Vanlanduit, S., Vanherzeele, J., Longo, R. & Guillaume, P., (2009). A digital image correlation method for fatigue test experiments, *Optics and Lasers in Engineering*, 47:371-378.
- Vari, L.M. & Heyns, P.S. (1997). Strain modal testing- a critical appraisal, *R & D Journal*, 13(3)83-90.
- Yam, L.H., Leung, T.P., Li, D.B & Xue, K.Z. (1996). Theoretical and experimental study of modal strain analysis, *Journal of Sound and Vibration*, 191(2):251-260.
- Ziebarth, H. & Baumgartner, R.J. (1981). Early detection of cross-sectional rotor cracks by turbine shaft vibration monitoring techniques, ASME Paper 81-JPGC-Pwr-26.

9. Appendix A: Solidworks drawing of setup for manufacturing

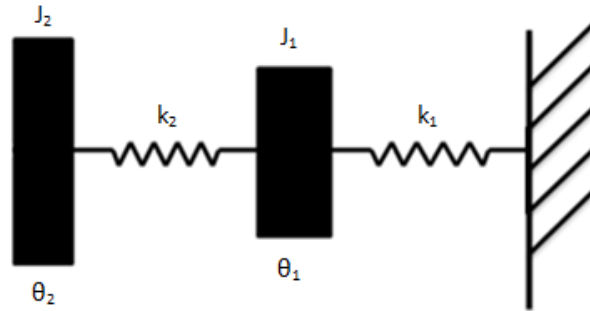


**SolidWorks Student Edition.
For Academic Use Only.**

10. Appendix B: Detailed lumped spring-mass calculations and FEM matrices derivation

10.1. Lumped spring-mass system

The FEM modal analysis torsional frequencies were verified by using a simple lumped spring-mass system. The calculations were based on the figure shown. From this, a system mass or rotational inertia in this case and stiffness matrices can be obtained. This is shown below.



Disk 1: J_1

$$J_1 \ddot{\theta}_1 = -k_1 \theta_1 + k_2 (\theta_2 - \theta_1) \quad (\text{Eq-B.1})$$

$$J_1 \ddot{\theta}_1 + k_1 \theta_1 + k_2 \theta_2 - k_2 \theta_1 = 0 \quad (\text{Eq-B.2})$$

$$J_1 \ddot{\theta}_1 + (k_1 + k_2) \theta_1 - k_2 \theta_2 = 0 \quad (\text{Eq-B.3})$$

Disk 2: J_2

$$J_2 \ddot{\theta}_2 = -k_2 (\theta_2 - \theta_1) \quad (\text{Eq-B.4})$$

$$J_2 \ddot{\theta}_2 + k_2 \theta_2 - k_2 \theta_1 = 0 \quad (\text{Eq-B.5})$$

Equation B.3 and B.6 may be summarised in a matrix form:

$$\begin{bmatrix} J_1 & 0 \\ 0 & J_2 \end{bmatrix} \begin{Bmatrix} \ddot{\theta}_1 \\ \ddot{\theta}_2 \end{Bmatrix} + \begin{bmatrix} (k_1 + k_2) & -k_2 \\ -k_2 & k_2 \end{bmatrix} \begin{Bmatrix} \theta_1 \\ \theta_2 \end{Bmatrix} = \begin{Bmatrix} 0 \\ 0 \end{Bmatrix} \quad (\text{Eq-B.6})$$

$$[J]\{\ddot{\theta}\} + [K]\{\theta\} = 0 \quad (\text{Eq-B.7})$$

Assuming solutions of Equation B.7 to be:

$$\{\theta\} = \{\bar{\theta}\} \sin \omega t \quad (\text{Eq-B.8})$$

Substituting into Equation B.8 and solving, an eigenvalue problem is developed as shown.

$$([K] - \omega^2 [J])\{\bar{\theta}\} = \{0\} \quad (\text{Eq-B.9})$$

$$[K]\{\bar{\theta}\} = \omega^2 [J]\{\bar{\theta}\} \quad (\text{Eq-B.10})$$

The disks dimensions are as found in Appendix A. Using this; the values for the J and K matrices may be calculated.

$$J_1 = \frac{mr^2}{2} = \frac{(\pi)(0.0635)^2(0.05)(7800)(0.0635)^2}{2} = 9.96e-03 \text{kg.m}^2 \quad (\text{Eq-B.11})$$

$$J_2 = \frac{(\pi)(0.072)^2(0.04)(7800)(0.072)^2}{2} = 1.13e-02 \text{kg.m}^2 \quad (\text{Eq-B.12})$$

$$K_1 = \frac{GJ_p}{L} = \frac{(80e09)(7.9e-08)}{0.3} = 21.07 \text{kN/m} \quad (\text{Eq-B.13})$$

$$K_2 = \frac{GJ_p}{L} = \frac{(80e09)(7.9e-08)}{0.2} = 31.6 \text{kN/m} \quad (\text{Eq-B.14})$$

$$J_p = \frac{\pi d^4}{32} = \frac{\pi(0.03)^4}{32} = 7.9e-08 \text{m}^4 \quad (\text{Eq-B.15})$$

Solving for the determinant of the system results in obtaining the natural frequency ω . This may simply be done in Matlab using the *eig* function which produces a diagonal matrix D of generalized eigenvalues and a full matrix V whose columns are the corresponding eigenvectors so that $K*V = J*V*D$. The diagonal matrix is still an eigenvalue and the square root must be used in order to obtain the natural frequency (MATLAB).

$$[V, D] = \text{eig}(K, M) \quad (\text{Eq-B.16})$$

Solving gives:

$$f_1 = 136.04 \text{Hz}$$

$$f_2 = 420.17 \text{Hz}$$

11. Appendix C: Torque calculation for frequency response analysis

During the motors normal running condition, a specific torque value is applied to the rotor. For the constant speed runs, this torque remains at a steady value. The constant 1100 RPM run resulted in a voltage torque reading of 0.69 V. It is imperative that the N.m torque of this voltage reading is found.

This is done by utilizing the 10 kg weight calibration results and combining it with the results of a different set of testing done. This testing involved applying the brake to the rotor as was done before, but this time instead of applying the weight, the motor was switched on, and the voltage torque applied was recorded. Figure 107 and 108 below shows the strains and voltages of the 2 setups.

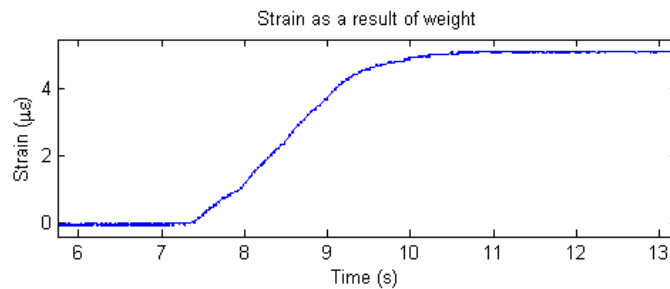


Figure 107 Strain due to weight

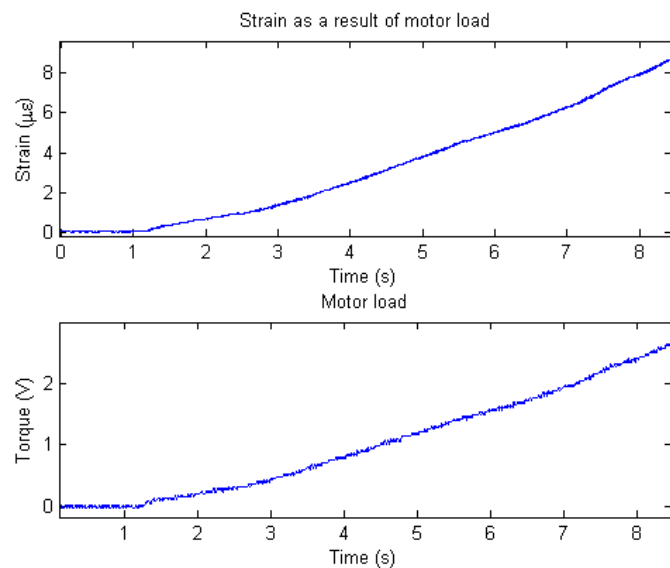


Figure 108 Strain and motor torque due to motor load

From the above plots, a relation can be developed linking the strain to the weight or torque applied. For instance at 0 µε there is no load and once the 10 kg is applied as a torque it results in 5.124 µε. This strain value increases linearly and since the magnitude of the loads are still in the elastic region it is safe to assume that the relation between strain and weight applied is also linear. Thus the relation below may be established, where in this case y is Torque (N.m) and x is strain (µε).

$$y = 0.77x$$

(Eq-C.1)

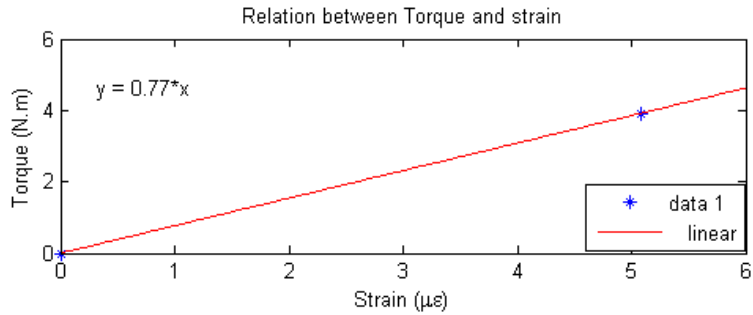


Figure 109 Torque (N.m) strain relation

A linear relationship can also be developed between strain ($\mu\epsilon$) and torque (V) in Figure 110. This is represented by Equation C.2 and shown in Figure 110. y is torque (N.m) and x strain ($\mu\epsilon$)

$$y = 0.3x \tag{Eq-C.2}$$

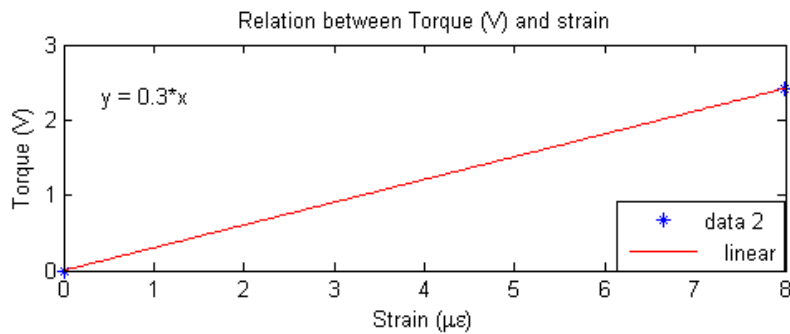


Figure 110 Torque (V) strain relation

From Figure 109 and 110, strain ($\mu\epsilon$) is a clear common factor and therefore a final relation between T (V) and T (N.m) can be achieved. Here, y is T (N.m) and x is T (V).

$$y = 2.5x \tag{Eq-C.3}$$

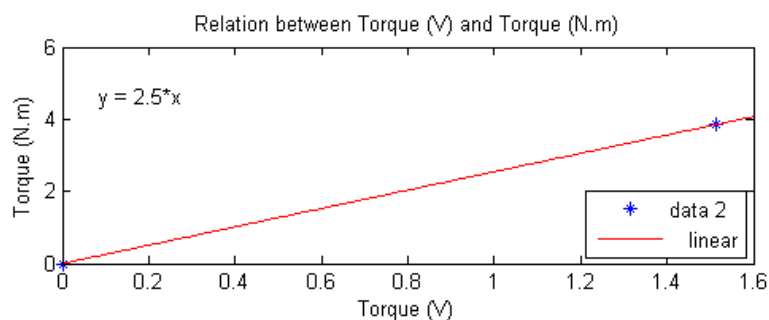


Figure 111 Calibrated Torque values

This relation, together with a applied torque of 0.69 V for a constant run, results in an actual torque of 1.725 N.m. This is the torque to be represented when doing the frequency response analysis.

12. Appendix D: Equipment Specification sheets

12.1. Digital Image Correlation System

System types	PONTOS 5M	PONTOS 4M	PONTOS HS
Measuring volume in mm ³	10x8 to 5000x4150	10x7 to 4000x2900	10x8 to 3500x2800
Camera resolution	2448 x 2050 pixels	2352 x 1728 pixels	1280 x 1024 pixels
Camera chip	2/3 inch, CCD	1 inch, CMOS	1 inch, CMOS
Connection camera to PC	Gigabit-Ethernet via sensor controller	Camera Link	Camera Link
Main hardware components	<ul style="list-style-type: none"> ▪ 19" PC ▪ Sensor ▪ Sensor controller ▪ LED lighting 	<ul style="list-style-type: none"> ▪ 19" PC ▪ Sensor ▪ Sensor controller ▪ LED lighting 	<ul style="list-style-type: none"> ▪ 19" PC ▪ Sensor ▪ Sensor controller
Laser pointer	yes	yes	yes
LED lighting with polarization filters	yes (10° or 30°)	yes (30°)	no
Measuring results	3D coordinates, 3D displacements, deformation		
For further information see http://www.gom.com			

The maximum image rate is fixed for the 5M and 4M cameras. For the high-speed camera (HS), higher frame rates can be achieved by dividing the height of the image size in half. The following table shows the frame rates of the different cameras with the respective image size and informs about the typical max. possible number of images.

Camera	Image size	Frequency in Hz BV RAM	No. of images BV RAM	Frequency in Hz PC RAM	No. of images 16 GB PC RAM	No. of images 32 GB PC RAM
5M	1 (max. camera resolution)	-	-	15	600	1300
	2x2 Binning	-	-	29	600	1300
4M	1 (max. camera resolution)	-	-	60	700	1600
	1/2	-	-	120	1400	3200
	1/4	-	-	240	2800	6400
	1/8	-	-	480	5600	10000

12.1.1. Camera lens and measuring volumes

		Measuring volume			
Camera support		500 mm (length)		800 mm (length)	
Camera angle		25°	25°	25°	25°
Sensors	Lenses (f in mm)	Min. Range	Max. Range	Min. Range	Max. Range
		Length x Width in mm			
PONTOS 5M	8	190 x 180	900 x 820	190 x 180	1550 x 1400
	12	130 x 110	610 x 540	130 x 110	1050 x 930
	17	90 x 75	440 x 380	90 x 75	760 x 650
	23	60 x 50	320 x 270	60 x 50	560 x 480
	35	35 x 29	210 x 170	35 x 29	370 x 310
	50	17 x 14	140 x 120	17 x 14	250 x 210
	65	10 x 8	100 x 85	10 x 8	190 x 150
PONTOS 4M	100	10 x 8	60 x 50	10 x 8	120 x 100
	20	130 x 100	710 x 560	130 x 100	1250 x 980
	35	60 x 48	410 x 310	60 x 48	720 x 550
	50	29 x 21	280 x 200	29 x 21	500 x 370
	65	20 x 14	200 x 150	20 x 14	380 x 280
PONTOS HS	100	10 x 7	120 x 90	10 x 7	240 x 170
	20	110 x 95	640 x 540	110 x 95	1100 x 940
	28	75 x 60	450 x 380	75 x 60	800 x 660
	35	50 x 43	360 x 290	50 x 43	640 x 530
	50	22 x 17	250 x 200	22 x 17	450 x 360
	100	10 x 8	110 x 85	10 x 8	210 x 160

12.2. Shunt resistor calibration

Gage Circuit	Resistance, ohms	Equivalent Microstrain*
120-ohm	599 880	100
	119 880	500
	59 880	1000
	29 880	2000
	19 880	3000
	14 880	4000
	11 880	5000
	5880	10 000

12.3. Digital Image Correlation system

12.3.1. Marker size

The reference point markers are available in the following sizes:

0.4 mm, 0.8 mm, 1.5 mm, 3 mm, 5 mm, 8 mm, 12 mm, 18 mm, 25 mm. Using the formula in the table below, the typical reference point size for your measuring volume is obtained. To do so, use the length of the measuring volume i.e. the largest value of the respective volume. If the result is a reference point size which is not available, round to the next available size. It is recommended using the next larger size.

PONTOS 5M	PONTOS 4M	PONTOS HS
Length of measuring volume x 0.004	Length of measuring volume x 0.004	Length of measuring volume x 0.008

Example:

For the measuring volume 125 x 90 with PONTOS 4M the following calculation results:

$$125 \times 0.004 = 0.5$$


This means, you should use the reference point marker size 0.8 mm for your measuring task.

12.3.2. Camera setup

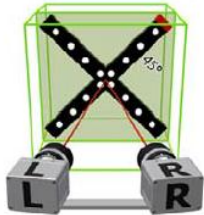
Lens	Measuring volume [mm x mm]	Comment	Min. length camera support [mm]	Distance ring [mm]	Measuring distance [mm]	Slider distance [mm]	Camera angle [°]	Calibration objects (coded)
	125 x 90	1)	500	---	195	66	27	CP20 90x72
	150 x 110	1)	500	---	230	74	25	CP20 175x140
	175 x 130	1)	500	---	260	88	25	CP20 175x140
	200 x 150	---	500	---	290	102	25	CP20 175x140
	250 x 180	---	500	---	355	130	25	CP20 250x200
	300 x 220	---	500	---	415	156	25	CP20 250x200
	350 x 260	---	500	---	480	186	25	CP20 350x280
	400 x 290	---	500	---	545	214	25	CP20 350x280
	500 x 370	---	500	---	670	270	25	CP20 350x280
	750 x 550	---	800	---	985	410	25	CC20 700x560
20mm, lens family A1 (Titanar)	1000 x 730	---	800	---	1285	542	25	CC20 1000x800
	1250 x 920	---	800	---	1600	682	25	CC20 1400x1120
	1500 x 1100	---	800	---	1900	688	21	CC20 1400x1120

Legend: 1) without laser pointer

a) Example of a few calibration steps

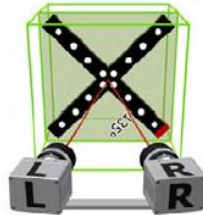
Calibration object cross - coded 

Step 1:



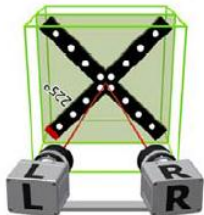
- Center of the measuring volume
- Cross position 45°

Step 2:



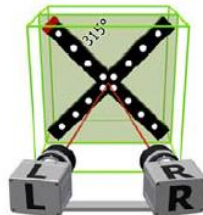
- Center of the measuring volume
- Cross position 135°

Step 3:



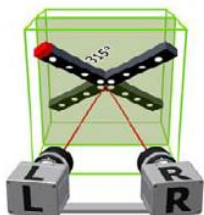
- Center of the measuring volume
- Cross position 225°

Step 4:



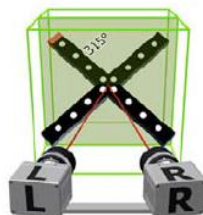
- Center of the measuring volume
- Cross position 315°

Step 5:



- Center of the measuring volume
- Cross position 315°
- Top tilted 40°

Step 6:



- Center of the measuring volume
- Cross position 315°
- Bottom tilted 40°

13. Appendix E: Matlab codes

The codes written below are done by the author in Matlab. The order removal code is based on the work of Groover et al. (2005).

13.1. Order removal and plotting of data

%Program that reads the optic and strain signal and applies order removal
%to it. From this various plots of time domain, frequency domain and order
%domain is plotted.

```
clc
```

```
clear all
```

```
close all
```

```
format long
```

```
tic
```

```
% Open and read the experimental data
```

```
fid = fopen('3in1_T1_2x3.txt', 'r');
```

```
% Loads pre-saved data of harmonics
```

```
load 3in1_T1_2x3 xv yv
```

```
% Collect info on sampling frequency and no. of columns and no. of entries
```

```
%skips the heading section to get to the data section. The k loop can be
```

```
%adjusted in order to start reading data at some random place in the middle
```

```
for k = 1:3
```

```
    dummy = fgetl(fid);
```

```
end
```

```
%Obtain sampling frequency,
```

```
dummy = fscanf(fid, '%s', 1);
```

```
fs = fscanf(fid, '%g', 1);
```

```
dummy = fgetl(fid);
```

```
%Obtain number of columns
```

```
dummy = fscanf(fid, '%s', 1);
```

```
num = fscanf(fid, '%d', 1);
```

```
dummy = fgetl(fid);
```

```
%Obtain number of entries
```

```
dummy = fscanf(fid, '%s', 1);
```

```
nel = fscanf(fid, '%d', 1);
```

```
dummy = fgetl(fid);
```

```
%Dummies to ignore rest of heading section
```

```
for k = 1:11
```

```
    dummy = fgetl(fid);
```

```
end
```

% Reads the optic and strain values

```
O_T = fscanf(fid, '%g %g %g', [num,nel]);
```

% Creates a time vector

```
dt=1/fs;
```

```
t=0:dt:((nel-1)*(dt));
```

% Smooth the values so there is less overshoot

```
op = smooth(O_T(:,1));
```

```
str = (O_T(:,2));
```

```
op(op>4.8)=5;
```

```
op(op<0.5)=0;
```

```
trig=4.9;
```

```
pulses=46;
```

% Send to tacho function to create a 1x revolution signal as a tacho signal

% from the 46 pulse optic signal

```
[tac,rev] = tacho(op,trig,fs,pulses);
```

%% Create one matrix for ease of use

```
mat = [t' op str];
```

```
mat(:,2)=mat(:,2)-2.5;
```

```
mat(:,3)=mat(:,3)-mean(mat(:,3));
```

% Variable for which signal to analyse

%st is strain or tacho 2- tacho, 3- strain

```
st = 2;
```

%Plot time domain signal

```
figure(1);subplot(3,1,1); plot(mat(:,1),mat(:,st));
```

```
xlabel('Time');ylabel('Volts');title('Time domain signal');legend('Optic sensor');
```

% Try to filter the signal, lowpass filter @ $(51200*0.015)/2=384\text{Hz}$

```
filtorder = 9;
```

```
Wn = 0.015;
```

```
[bb,aa] = cheby1(filtorder,0.5,Wn);
```

```
mat(:,st) = filtfilt(bb,aa,mat(:,st));
```

%Plot filtered time signal

```
figure(1);subplot(3,1,2);plot(mat(:,1),mat(:,2));
```

```
xlabel('Time');ylabel('Volts');title('Filtered time domain signal');legend('Filtered Optic sensor');
```

% Define parameters for FFT analyses

```
L = length(mat);
```

% Next power of 2 from length of y

```

NFFT = 2^nextpow2(L);
f = fs/2*linspace(0,1,NFFT/2+1);
Y = fft(mat(:,st),NFFT)/L;
YY = 2*abs(Y(1:NFFT/2+1));

% Plot frequency content of time signal
figure(1);subplot(3,1,3);plot(f,YY);
xlabel('Frequency');ylabel('Magnitude dB');title('FFT of time signal');

% Order removal section
% Specifying the number of rotations in entire signal and number of divisions per revolution
required

%number of revolutions analysed
R=length(rev);
%number of constant angle divisions
nod = 360;
%delta theta
dthet = 360/nod;

% Dividing the actual signal into required divisions
t1=0;
p=1;
for cc = 1:length(rev)-1;
    t1 = rev(cc,1);
    t2 = rev(cc+1,1);
    temp = linspace(t1,t2,nod+1);
    temp(end) = [];
    time(1+nod*(cc-1):nod*cc) = temp;
end

% Interpolating the new time signal with original to get the y-value for new time signal
val = interp1(mat(:,1),mat(:,st),time);

%Plotting constant angle and constant time signals
figure(2);plot(mat(:,1),mat(:,st),'*-','time,val','ro');
xlabel('Time');ylabel('Volt');legend('Constant time signal','Constant angle signal');

% Creating a time equivalent angle vector
theta = 0:dthet:(R*360);

% Creating FFT in the order domain for constant angle representation of original signal

%Sampling frequency for order domain
fsO = nod;
%Length of signal to be analysed
LO=length(V);

```

```

%Next power of 2 from length of y
NFFTO = 2^nextpow2(LO);
%Creating the order axis vector
fO = fsO/2*linspace(0,1,NFFTO/2+1);

%equivalent to frequency vector
YO = fft(V,NFFTO)/LO;
YYO = 2*abs(YO(1:NFFTO/2+1));
yyO = LO*ifft(YO);

%Finding the fft of the signal
%obtaining the correct length
%Inverse FFT applied

% Removal of dominant orders
Xn = YO;

% Selecting harmonics which represent the orders
for j=1:nod-1
    semilogy(abs(YO))
    dd=1457*j;
    axis([(dd)-500 (dd)+500 0 3.5])
    title([num2str(j), ' place ', num2str(dd)]);
    [xv(j),yv(j)]=ginput(1);
end

% Saving their location
save 3in1_T1_2x2 xv yv

xv=round(xv);

% Since each order is represented by a distribution of data. Removing about
% 20 data points would cause the order to be removed. Simply removing a
% single point which is represented by 50 data points would not work.
sss=20;
for x = 1:nod-1
    Xn(xv(x)-sss:xv(x)+sss)=min(YO(xv(x)-sss:xv(x)+sss));
end
XXn = 2*abs(Xn(1:NFFTO/2+1));

% Plotting old and new order content
figure(3);plot(fO,YYO,fO,XXn,'r--');
xlabel('Orders');ylabel('Magnitude');title('Comparison of removal of orders');
legend('Orders','Orders removed');

% Taking the order domain back to angular domain
xxn = LO*ifft(Xn);

% Finding the new time domain signal associated with the new order removed signal
VAL = interp1(time(1:length(xxn)),xxn,mat(:,1));
dum = 2^nextpow2(length(VAL))/2;

```

```
VAL = VAL(1:end);
TIME = mat(1:length(VAL),1);
```

```
% Getting the FFT of the new signal
```

```
dT = TIME(2)-TIME(1);
fsT = 1/dT; %Sampling frequency for order domain
LT=length(VAL); %Length of signal to be analysed
NFFTT = 2^nextpow2(LT); %Next power of 2 from length of y
fT = fsT/2*linspace(0,1,NFFTT/2+1); %Creating the order axis vector,
%equivalent to frequency vector
YT = fft(VAL,NFFTT)/LT; %Finding the fft of the signal
YYT = 2*abs(YT(1:NFFTT/2+1)); %obtaining the correct length
```

```
% Plotting order removed FFT with previous FFT
```

```
figure(4);plot(f,YY,fT,YYT,'r--');xlabel('Frequency');ylabel('Magnitude');
title('Comparison of old and new FFT');legend('Old FFT','Order removed FFT');
```

```
% Plots time domain graph of optic or strain signal for waterfall, spectrogram and averaged
%plots
```

```
%Number of spectre
```

```
N = 12;
fmin=0;
fmax=500;
zmax=0.01;
fftsize = 512000;
```

```
%Waterfall plot
```

```
figure(6);[T,F,M]=timeh2oh(VAL,fs,N,fftsize,fmin,fmax,zmax); title('Waterfall')
```

```
%Averaging the waterfall plot to get a single averaged plot
```

```
Yavg = (sum(M(1:N,:)))/N;
figure(7); plot(F,Yavg);xlabel('Frequency');ylabel('Magnitude');title('Averaged frequency
plot');
```

```
% Undersampling Section of the good optic and strain signals
```

```
% Define undersampling value to be used
```

```
undersampledV = 9;
```

```
% Undersample the good signal
```

```
unfs = undersampledV; %Define undersampled frequency
undt = fs/unfs; %Time increment associated with undersampled
%frequency
matund = mat(1:undt:end,st); %New matrix with undersampled data of
%original signal
matund=VAL(1:undt:end); %New matrix with undersampled data of order
%removed signal
```

```
% Doing FFT analyses on the undersampled data
```

```
uL = length(matund);
```

```
%Next power of 2 from length of y
```

```
unNFFT = 2^nextpow2(uL);
```

```
unf = unfs/2*linspace(0,1,unNFFT/2+1);
```

```
unY = fft(matund,unNFFT)/uL;
```

```
unYY = 2*abs(unY(1:unNFFT/2+1));
```

```
% Plotting the undersampled signal
```

```
figure(8);
```

```
plot(unf,unYY);
```

```
xlabel('Frequency')
```

```
ylabel('Magnitude')
```

```
title('Undersampled optic sensor')
```

```
% Time of analysis run
```

```
toc
```

13.2. Creating tacho signal using Tacho function

```
function [tactime,rev] = tacho(op,trig,fs,pulses)
```

```
%The purpose of this function is to read the pulses from the coded tape and  
%creates a tacho pulse depending on number of pulses per revolution. Then it  
%saves the time at the tacho pulses
```

```
% Define location and creating time signal
```

```
d=sign(op-trig);
```

```
dd=diff(d);
```

```
tt=maketime(dd,fs);
```

```
% Finds location where the trigger and time represents one of the 46 pulses
```

```
tactime=tt(dd>1.5);
```

```
tactime(:,2)=zeros;
```

```
%Creating the tacho and time vector for 46pulse/revolution
```

```
tactime(1:pulses:end,2)=6;
```

```
rev=tactime(tactime(:,2)>5,:);
```